DESIGN, MODELING, IDENTIFICATION AND CONTROL OF MECHATRONIC SYSTEMS

Part I. Design Rules and Actuator Modeling for the Optimization of Mechatronic Systems

Part II. Identification and Control of Piezoelectric Actuators

Oriol Gomis i Bellmunt
Doctoral Thesis
Barcelona, February 2007

UNIVERSITAT POLITÈCNICA DE CATALUNYA

DEPARTAMENT D'ENGINYERIA ELÈCTRICA

Electrical Engineering Department
UNIVERSITAT POLITÈCNICA DE CATALUNYA

CITCEA - Centre d´Innovació Tecnològica
en Convertidors Estàtics i Accionaments
UNIVERSITAT POLITÈCNICA DE CATALUNYA

Doctoral Thesis

DESIGN, MODELING, IDENTIFICATION AND CONTROL OF MECHATRONIC SYSTEMS

Part I. Design Rules and Actuator Modeling for the Optimization of Mechatronic Systems

Part II. Identification and Control of Piezoelectric Actuators

Author: **Oriol Gomis i Bellmunt**

Advisors: **Samuel Galceran i Arellano**
Fayçal Ikhouane

Barcelona, February 2007

Són moltes les persones que m'han donat suport durant aquests anys i que han fet possible que ara estigui acabant d'escriure les últimes línies de la tesi doctoral. Moltes gràcies a tots.

Als directors de la tesi. Al Samuel Galceran pel seu suport incondicional, per comunicar-me la seva visió pràctica de l'enginyeria i per fer fàcil el que podria haver estat difícil i al Fayçal Ikhouane per transmetre'm la seva metodologia científica i la capacitat de tractar els problemes d'enginyeria des de la formalització teòrica.

A tots els companys d'Engitrol, en especial a l'Oscar i la Carmen, per introduir-me al món de l'enginyeria i a la realitat de la industria i pels anys que vaig passar amb ells.

Den Kollegen und Freunden aus Braunschweig und vom DLR, mit denen ich immer interessante technische und nicht-technische Diskussionen hatte, die mir beim Deutsch halfen und mit denen ich eine tolle Zeit hatte. Flavio Campanile, für sein Rat und Beistand zum ersten Teil der Dissertation. Robert, Damiano, Björn, Nicole und Valerie, für ihre Freundschaft.

A tots els companys del CITCEA i del Departament d'Enginyeria Elèctrica, pel suport que he rebut durant aquest temps i per l'intercanvi d'idees. Al Pere Castell, per la seva col·laboració en els muntatges experimentals. Al Quim López i al Daniel Montesinos per la seva valuosa ajuda en el disseny de les plaques i en la programació del DSP. A l'Antoni Sudrià per donar-me l'oportunitat d'integrar-me a l'equip del CITCEA.

A la meva família, per donar-me suport en tot moment. Als meus pares, a l'Anna, i als avis, en especial al padrí Cristòfol, per transmetre'm la seva actitud positiva davant la vida.

Als que heu aguantat les llargues explicacions quan em preguntàveu de què anava això de la tesi. A l'Andreu i el Xavi per tots aquests anys d'anades i vingudes. A l'Edu, el Josep, el Manuel i l'Oriol pels anys d'estudiants on potser no ens vam fer enginyers, però

ens vam fer persones. Al Salva, el Joan i la Marta, per les llargues converses sense conclusions i per algunes conclusions sense converses.

A la Sílvia, per ser com és, per estar sempre al meu costat, per tot el que hem viscut i sobretot, per tot el que ens queda per viure.

A la histèresis, la no-linealitat i la complexitat, perquè en aquest món on tot es vol simplificar i resumir en una frase, una de les poques coses clares que podem tenir és que les respostes són sempre difícils i complexes. La histèresis i les no-linealitats no són només presents a l'enginyeria.

Acknowledgements

Supported by CICYT through grants DPI2005-08668-C03-03 and DPI2005-08668-C03-01.

Part of this thesis is a result of a research training project which has been developed in the DLR (German Aerospace Center) in Braunschweig (Germany) and supported by a Marie Curie Fellowship of the European Community programme *Smart Lightweight Structures And Transportation Application* under the contract number HPMT-CT-2001-00298.

Resum

Les societats modernes plantegen nous reptes que demanden noves maneres de tractar els projectes d'enginyeria. Els enginyers han d'afrontar aquests reptes i desenvolupar solucions òptimes i eficients pels problemes clàssics i nous. Els diferents avenços produïts en la tecnologia hi poden ajudar, però una nova manera de tractar els problemes enginyerils és també necessària, no considerant únicament les diferent especialitats de l'enginyeria aïlladament. En aquest context, podem parlar de la creació d'una nova filosofia de fer enginyeria: la Mecatrònica. En els darrers anys han aparegut diferents definicions: A [2] la Mecatrònica es defineix com *l'aplicació de decisions complexes a l'operació de sistemes físics.* A [22; 48] la Mecatrònia és definida com *la integració o sinergia de diferents disciplines de l'enginyeria.* Aquestes disciplines inclouen *l'enginyeria mecànica*, *l'enginyeria elèctrica*, *l'enginyeria electrònica*, *l'enginyeria de control*, *les comunicacions industrials* i *l'enginyeria de software.* A [50] es dóna una definició més específica: *En general, la Mecatrònica són soluciones de sistemes, que poden ser realitzades utilitzant components mecànics, electrònics, computacionals, materials, químics i de programari amb les seves corresponents disciplines enginyerils. L'objectiu d'aquestes solucions és incrementar la funcionalitat del sistema, l'intel·ligència i la fiabilitat, reduint els costos de producció.* No obstant, tal com sosté [48], la importància del concepte no està únicament en la definició sinó a la filosofia que hi ha al fons. És important de veure, que la Mecatrònica no és només la suma dels resultats de diferents disciplines, sinó la filosofia enginyeril per

afrontar els problemes com un de sol, fent servir les eines que subministren les diferents disciplines.

La present tesi ha estat concebuda com un treball multidisciplinar. Comença centrada en l'anàlisi general de diferents classes d'actuadors, per després treballar la identificació i control d'actuadors piezoelèctrics. Per fer la primera part, s'investiguen aspectes *mecànics* i *elèctrics*, en especial les expressions de la força i el treball de diferents tipus d'actuadors, així com totes les magnituds relacionades. La segona part utilitza *matemàtiques* i *enginyeria de control*, aplicant-ho a actuadors reals amb *electrònica de potencia* i *enginyeria de software.*

Les dos parts de la tesi tracten problemes de diferent natura. La primera part es titula **Regles de disseny i modelat d'actuadors per l'optimització de sistemes mecatrònics** i es centra en proporcionar un anàlisis detallat de diferents actuadors utilitzant un procediment general, orientat a millorar el disseny de l'actuador. S'introdueix una nova metodologia per analitzar actuadors lineals electromagnètics i hidràulics modelitzant la seves magnituds mecàniques (força, treball i desplaçament) com a funcions de la geometria i les propietats del material, estudiant l'escalabilitat (en el sentit de produir la mateixa distribució de tensions i deformacions per diferents mides). La motivació de realitzar aquest treball neix de la necessitat d'estructures i sistemes lleugers i de volum reduït, que han de ser integrats en el procediment de disseny el més aviat possible. Per tant, s'estudien les relacions geomètriques, les proporcions i les propietats dels materials que maximitzen les magnituds mecàniques de sortida dels actuadors per un volum i pes limitat, així com l'escabilitat per la seva posterior integració en estructures. Els resultats són validats mitjançant anàlisi dimensional de les expressions obtingudes i comparant els resultats numèrics amb dades d'actuadors industrials. Es considera el comportament estàtic de diferents classes d'actuadors, incloent actuadors hidràulics i electromagnètics lineals.

La segona part es titula **Identificació i Control d'Actuadors Piezoelèctrics**. Els actuadors piezoelèctrics estan demostrant ser una solució fiable per moltes aplicacions, des del microposicionament (màquines eina, dispositius òptics o microscopis moderns) al control actiu d'estructures. La principal motivació de la segona part de la tesis és aprofundir en models per representar el comportament histerètic dels actuadors piezoelèctrics per posteriorment aplicar els models al desenvolupament de controladors pels sistemes histerètics. Es desenvolupa inicialment un estudi general dels actuadors piezoelèctrics per després tractar la seva modelització. Degut a l'elevat comportament no-lineal observat es necessita un model d'histèresis. El model de Bouc-Wen ha estat escollit i s'ha treballat en la identificació dels paràmetres del model i la seva validació. Un cop el sistema ha estat modelat, s'ha dissenyat un nou controlador lineal i s'ha implementat en una plataforma experimental utilitzant un DSP (Processador digital de senyal).

Encara que les dues parts estan clarament diferenciades, la unitat de la tesis pot ser trobada a les arrels de la Mecatrònica. La tesis tracta la resposta a una sola pregunta: Com podem millorar un sistema mecatrònic? No obstant, la resposta és doble: Dissenyant i modelant actuadors òptims considerant el sistema o estructura complet i controlant el sistema adequadament fent servir els models desenvolupats.

Abstract

Fast changing societies come up with new challenges that require new engineering approaches. Engineers have to face such challenges and provide novel and more efficient solutions to classical and new problems. This can be done by using different relevant advances produced in technology. Furthermore, a new way of addressing the engineering problems has to be applied, not considering only isolated engineering specialities. In this frame, we can talk about the creation of a new engineering philosophy: Mechatronics. Many definitions have been appeared in the last years: In [2] it is stated that *Mechatronics is the application of complex decision making to the operation of physical systems*. In [22; 48] Mechatronics is defined as *the integration or synergy of different engineering disciplines*. Such disciplines may include *Mechanical Engineering*, *Electrical Engineering*, *Electronics Engineering*, *Control Engineering*, *Industrial Communications* and *Software Engineering*. In [50] a more specific definition is given: *In general, mechatronics are system solutions, which can be realized using mechanical, electronic, computer, material, chemical, and software components and the corresponding engineering disciplines. The goal of these solutions is to increase system functionality, intelligence, and reliability while decreasing system production cost*. Nevertheless, as it is stated in [48], the importance of the concept does not lie only in the definition but in the philosophy behind it. It is very important to note that Mechatronics is not only the sum of the results of the different disciplines, but the engineering philosophy to face engineering problems as a whole, employing the tools provided by the different disciplines.

The present thesis has been devised as a multidisciplinary work. It begins focusing on the general analysis of different actuator classes to later face the identification and control of piezoelectric actuators. To perform the first part, *mechanical* and *electrical* issues are investigated, focusing on the force and work expressions of certain classes of actuators, and all the quantities involved. The second part employs *mathematics* and *control engineering*, applying it to real actuators with *power electronics* and *software engineering*.

The two parts of the thesis deal with problems of different nature. The first part is titled **Design Rules and Actuator Modeling for the Optimization of Mechatronic Systems** and focuses on providing the detailed analysis of different actuators using a general procedure and oriented towards improving the actuator design. It introduces a new methodology to analyze linear electromagnetical and hydraulic actuators by modeling their maximum output mechanical quantities (force, work and stroke) as functions of the geometry and material properties and discusses the scalability (in the sense of producing the same stress and strain distribution for different sizes). The motivation to undertake such a work stems from the need for light and volume reduced structures and systems, which are to be integrated in the design procedure as early as possible. Hence, the geometric relationships, aspect ratios and material properties that maximize the actuator output quantities with a certain limited volume or weight, along with their scalability for the integration in structures are studied. A validation of the results is done by performing dimensional analysis of the expressions obtained and comparing numerical results with industrial actuator data. The static behavior of different classes of actuators is considered. Such actuators include linear hydraulic and electromagnetic actuators.

The second part is titled **Identification and Control of Piezoelectric Actuators**. Piezoelectric actuators are proving to be a reliable solution for many engineering applications, ranging from micro-positioning (machine tools, optic devices or modern microscopes) to active control of structures. The main motivation of this thesis part is to delve into models to represent the hysteretic behavior of piezoelectric actuators in order to apply them to the conception of controllers for such hysteretic systems. A general study of piezoelectric actuators is performed to later deal with the modeling of such actuators. Due to the high non-linear behavior observed, the problem of identifying and modeling the actuator requires a hysteresis model. The Bouc-Wen model has been chosen and investigations to identify its parameters and to validate the model have been undertaken. Once the system has been identified, a linear controller has been designed and implemented in a real platform, employing a DSP (Digital Signal Processor).

Although the two parts are clearly differentiated, the thesis unity can be found in the roots of Mechatronics. The thesis deals with the response to one single question: How can we improve a mechatronic system? However, the answer is twofold: By designing and modeling optimum actuators taking into account the whole system or structure and by controlling the system appropriately using developed models.

Thesis Outline

The thesis has been divided into two parts. **Part I** is entitled **Design Rules and Actuator Modeling for the Optimization of Mechatronic Systems** and includes chapters 1, 2, 3, 4 and 5. **Part II** is entitled **Identification and Control of Piezoelectric Actuators** and includes chapters 6, 7, 8, 9, 10, 11 and 12.

The first part has been structured as follows. In **chapter 1** a brief introduction is presented, defining the orientation, motivation and objectives. In **chapter 2** the methodology is introduced, including the description of the different steps: design parameters, force-stroke and work-stroke curves, discussion of the limiting quantities involved in the output quantities expressions, maximum force for a given size, analysis of the scalability of the actuator, dimensional analysis study and comparison between the theoretical results and the industrial actuators quantities.

In **chapter 3** the methodology is applied to electromagnetic actuators. Two linear electromagnetic actuators are considered: solenoids and moving coil actuators. In **chapter 4** the methodology is applied to hydraulic actuators. Finally, in **chapter 5** the conclusions are summarized.

The second part has been structured as follows. In **chapter 6** a brief introduction is presented, defining the motivation and objectives. In **chapter 7** an introduction to the piezoelectric effect is exposed. The relevant quantities and constants are introduced and the typical linear formulation for low and high frequency are stated. Piezoelectric actuators are introduced, along with their common applications, advantages and drawbacks.

The Bouc-Wen hysteresis model is introduced in **chapter 8**. Thereafter, an identification technique to determine the parameters is proposed and its robustness against different classes of perturbations is discussed in **chapter** 9.

Chapter 10 adds an adaptation to the previous model, in order to allow it to characterize better the behavior of piezoelectric actuators. The model is validated with a real actuator and the advantages over the previous chapter method are shown.

In **chapter** 11 the models developed are employed to design a new controller. The controller takes into account not only the error but the output control effort which is tried to keep unchanged when a perturbation occurs.

In **chapter** 12 the conclusions of the thesis part are summarized.

Contents

List of Tables

List of Figures

Part I

Design Rules and Actuator Modeling for the Optimization of Mechatronic Systems

Chapter 1

Introduction

An actuator can be defined as an energy converter which transforms energy from an external source into mechanical energy in a controllable way. The actuator input quantities depend on the type of energy used. For electromagnetical, piezoelectric and magnetostrictive actuators the input quantities can be the current, the charge or the voltage; for fluid power actuators the fluid pressure or the flow; for shape memory alloys and thermal expansion actuators the temperature. The relevant output quantities to be considered in the optimization are the force, the work and the stroke. The input quantities are provided by a control system which lead output quantities to the referenced values. Such quantities are ruled by the mechanical load system or structure, which defines the relationship between the force and the stroke. The integration of actuators and loads in a mechatronic or adaptronic[1] system allows the conception of a unique system which is to be analyzed.

1.1 Design Rules and Actuator Modeling for the Optimization of Mechatronic Systems

The increasing quantity of different novel actuator technologies being used in different industrial applications along with the need for light and volume

---

[1] Adaptronics is a term referred to the analysis, design and integration of smart structures and systems.

reduced systems are boosting the necessity of general analysis using uniform criteria.

Regarding the comparison of different actuators, in [1] an actuator selection criterium is presented in order to develop a software to choose the most suitable actuator for different applications. To undertake such a task performance indices and material property charts are provided. The actuators as energy converters are analyzed and compared in [37], focusing on robot applications. A comparison of the performance of different actuators regarding stress, strain, energy and precision is introduced in [23], showing different tables and graphics to compare the performance of the studied actuators. In [12] the performance of solid-state actuators available in the market is compared and studied. The environmental impact of the mechanical design is presented in [20], and material property charts including this new criteria are presented. A new selection and classification criterium is introduced in [60], including a comparison between existing actuators in the market as well as their stress, strain, power densities, and resolution.

Although the previous references deal with the comparison of different actuators using different criteria, to the best of our knowledge no methodology to address the modeling of each actuator allowing comparisons of different classes of actuators has been found. Therefore, the present work proposes a novel methodology which might be applied to any class of actuator in order to optimize mechatronic and adaptronic systems.

The motivation to develop a methodology stems from the need for light and volume reduced structures and systems, which are to be integrated in the design procedure as early as possible. Hence, the geometric relationships, aspect ratios and material properties that maximize the actuator output quantities with a certain limited volume or weight, along with their scalability for the integration in structures are studied. A validation of the results is done by performing dimensional analysis of the expressions obtained and comparing numerical results with industrial actuator data.

1.2 Application of the methodology

Once the methodology has been presented, it is applied to electromagnetic and hydraulic actuators. Electromagnetic actuators are commonly used in many engineering fields. They have good force and work densities, although not as high as hydraulic actuators. They are easily controllable and the power source providing the energy can be placed as far away as necessary. Their use must be avoided when their environment must be free of electromagnetic fields or interferences. However, many technologies to deal with such effects are being developed. The electrical circuit provides the current to the coils. This current flows through wires and produces heat due to the Joule effect. Different materials can be employed for the wires but usually copper, silver or aluminium are used because they present the lowest resistivities. The magnetic circuit provides the flux and the force. Different materials can be used in the magnetic circuit depending on the magnetic permittivity. The electromechanical actuators have an electrical and a magnetic circuit. Such circuits are built together, and therefore, the heat generated in the coils by Joule effect must flow through part of the magnetic circuit. The heat transfer circuit includes all the components of the actuator and depends on the geometry of each of them. Although different materials can be used in both the electric and magnetic circuit, it is common to talk about copper for the electric circuit and iron for the magnetic circuit.

As far as fluid power actuators are concerned, they use the fluid power to provide mechanical work; the difference between the pressures P in two different chambers results in a relative pressure which produces a force F in a given surface S which yields $F = PS$. The pressure is the input quantity, performing the same function as the current in electromechanical actuators. The fluid actuators employed in the industry are mainly divided by the state of the fluid employed: *hydraulic actuators* employ an incompressible liquid (usually oil), while *pneumatic actuators* employ a compressible gas (air). Hydraulic actuators are commonly used in many engineering fields. They show the following advantages: very good force and work densities (more than any other actuator), strokes as long as necessary (if enough fluid is supplied), easily controllable and the fact that the power source providing the energy can be placed far away from the actuator (but not as far as with the electromagnetic actuators). Their main disadvantages are the safety problems generated by the high pressures needed (the same fact that provides the advantages), the leakage flow (that can become an important problem for actuator performance, safety conditions and environmental issues) and the hardly inflammability of the oil employed. Pneumatic actuators are used in many engineering fields, as well. They present good force and work densities, even though not as high as the hydraulic actuators, they can perform strokes as long as needed like their hydraulic counterparts, they are easily controllable and the power source providing the energy can be placed far away from the actuator. However, they cannot work with pressures as high as the hydraulic actuators because of the problems derived from the high compressibility of the gases. This same fact makes the hydraulic actuators faster in response and stiffer against external load disturbances. The efficiency of the hydraulic systems is also higher. It is caused by the losses of energy due to the heat transfer (in the air cooling), higher leakage and worse lubrication which occurs in the pneumatic systems. Nevertheless, the pneumatic systems can work at higher environment temperatures. In the present work, the hydraulic actuators are studied. However, some of the results obtained also apply for their pneumatic counterparts.

Although several studies [1; 12; 23; 37; 60] in the literature provide rules and charts for selecting the most optimal actuator class for different applications and others [21] delve into the study of different actuator classes, to the best of our knowledge no detailed analysis of linear electromagnetic or hydraulic actuators following a general procedure and oriented towards improving the actuator design has been found. The present thesis introduces a new methodology to analyze linear electromagnetical and hydraulic actuators by modeling their maximum output mechanical quantities (force, work and stroke) as functions of the geometry and material properties and discusses the scalability (in the sense of producing the same stress and strain distribution for different sizes).

The motivation of this thesis part is to provide the detailed analysis of different actuators using a general procedure, rather than introducing a general analysis (see [23]). The static behavior[1] of different classes of actuators is considered. Such actuators include linear hydraulic and electromagnetic actuators. In this second group, the actuators have been chosen as examples of electromagnetic actuators with (moving coil) and without (solenoid) permanent magnets.

1.3 Objectives and Scope

The objectives of the present thesis part may be summarized as:

1. **Design of a methodology to deal with the modeling and optimization of industrial actuators.** The methodology is the crucial step for the study of different classes of actuators. The methodology includes design optimization, scalability analysis and validation with real actuators and dimensional analysis.

2. **Application of the methodology.** The methodology has to be applied to common industrial actuators: hydraulic and electromagnetic. These two classes of actuators are the most employed in the industry.

As far as the scope is concerned, the optimization is performed for linear hydraulic and electromagnetic actuators considering static behavior. Neither the dynamics nor the non-linear motion are considered in this work.

1.4 Outline

The thesis part has been structured as follows. In **chapter 2** the methodology is introduced, including the description of the different steps: design parameters, force-stroke and work-stroke curves, discussion of the limiting quantities involved in the output quantities expressions, maximum force for

---

[1] The static behavior analysis assumes very slow operation, and hence it does not take into account the effect of the frequency in the analyzed system.

a given size, analysis of the scalability of the actuator, dimensional analysis study and comparison between the theoretical results and the industrial actuators quantities.

In **chapter 3** the methodology is applied to electromagnetic actuators. Two linear electromagnetic actuators are considered: solenoids and moving coil actuators. In **chapter 4** the methodology is applied to hydraulic actuators. Finally, in **chapter 5** the conclusions are summarized.

Chapter 2

Design Rules and Actuator Modeling for the Optimization of Mechatronic Systems

As previously stated, the purpose of this work is to develop design rules and models for actuator optimization. This section explains the general procedure introducing all the concepts which are going to provide such rules. The main steps are:

1. Design parameters. Study of the geometry and materials of the actuators.
2. Force-stroke and work-stroke curves. Analysis of the force, stroke and work production.
3. Discussion of the limiting quantities involved in the output quantities expressions.
4. Maximum force for a given size. Study of the limit force, stroke and work.
5. Analysis of the scalability of the actuator.
6. Dimensional analysis study of the relevant quantities.

7. Comparison between the theoretical results and the industrial actuators quantities.

The first step introduces the design parameters in the construction of the actuator. A detailed schematic drawing is presented showing the geometric properties and the materials used. In order to obtain a clear design parametrization *geometrical factors*, *aspect ratios* and *filling factors* are presented.

The geometrical factors define the ratio between any geometrical dimension and a reference geometrical dimension in the same axis. A non-dimensional factor k_i is obtained for each length l_i as a quotient of this length and the reference length l in its axis as:

$$k_i = \frac{l_i}{l} \rightarrow l_i = k_i l \tag{2.1}$$

Using these factors, all the lengths in the same axis are related to one single length, simplifying the analysis of the size dependence of different quantities. The number n of independent reference lengths depend on the degrees of symmetry of the actuator. An actuator with cylindrical shape presents two different reference lengths ($n = 2$, since a cross-section diameter and a length define a cylinder), a spherical actuator would be defined with one reference length ($n = 1$, only a diameter defines a sphere).

The relationships between different reference lengths is obtained using aspect ratios as:

$$\eta = \frac{r}{l} \tag{2.2}$$

If n independent reference dimensions are necessary, $n - 1$ aspect ratios are to be defined. The combination of the previous two concepts implies that all the geometric dimensions are expressed as a function of one single reference length, which is associated to the size of the actuator and allows the independent study of the performance of an actuator with a limited size and the actuator performance when the size is changed.

The filling factor provides the portion of usable cross-section surface when electric wires are concerned. Due to the shape of the wires and the necessary electrical isolation, the entire cross-section designed for the copper wires is not employed. The filling factor yields:

$$k_{ff} = \frac{S_{copper}}{S_{total}} \tag{2.3}$$

where S_{copper} is the cross-section of the wires and S_{total} the overall cross-section of the coil.

A general expression of the output quantities as a function of all the input quantities involved is developed in the second step. These expressions are taken from the general physics laws ruling the actuators concerned. Each type of actuator behaves in a different way and its expressions are presented describing all the assumptions done. The force-stroke curves and work-stroke curves are obtained, establishing the characterization plot of the actuator. The inputs (currents, voltages, pressures, etc.) capable of changing these curves are presented, explaining why and how they can influence the actuator performance. The different working points depending on the load are discussed and graphically shown. It is important to note that the design parameters cannot be considered inputs and their influence is discussed in the following steps.

The third step focuses on the quantities involved in the expressions obtained in the second step. The output quantities developed by an actuator can be controlled by modifying the input quantities (electrical voltages and currents, fluid pressures and flows, etc.). Some physical limits (maximum allowed temperature, mechanical resistance etc.) do not allow the actuator output quantities to be increased indefinitely. Since the purpose of the present work is to separately deal with the maximum force, stroke and work available in a given size and the performance scalability, only geometric quantities (reference lengths), relationships (geometrical factors, aspect ratios and filling factors), material properties (magnetic permeability, resistivity, resistivity temperature coefficient, conductivity, etc.), universal physics constants (μ_0, σ, etc.) and physical thresholds (maximum temperature, stress, etc.) are to be used. Therefore, all the other quantities (currents, magnetic fluxes, pressures, etc.) must be expressed as functions of the mentioned quantities.

The physical thresholds limiting the maximum force, stroke and work are discussed, showing how they limit the performance of the actuator. The principle limiting quantity in electromagnetical actuators is the allowed temperature.

The quantities involved in the force, stroke and work expressions developed in the latter step are substituted in the fourth step in order to express them depending on the limiting values and design parameters. The analysis of a given output quantity, for a given class of actuators, as a function of the design variables, shows (as a rule) a monotonic dependence on certain size variables. For instance, the limit force will typically depend monotonically on the actuator cross section and the actuator stroke on the length. Other design variables will exist (typically some aspect or shape factors) for which the considered output quantity can be maximized. The search of such optimal design variables is very useful, since it enables a fair and effective comparison between actuators of different kinds and can be of essential importance for the optimization of the whole active mechanical system. These expressions are carefully analyzed keeping the size constant. The limit force, stroke and work available in a given size are studied depending on the different design parameters. The geometric factors, aspect ratios and the materials selected providing the best performance are discussed. This leads to a general expression of the maximum force, stroke and work in a given volume and provides design rules to optimize the actuator's performance with the proper ratios and materials.

In the fifth step the actuator performance as a function of the size is analyzed and the scalability and application range are discussed. If two geometrically similar passive mechanical systems with a given scale factor are considered, and their mechanical behavior can be described by an approach based on continuum mechanics, they are to be loaded by forces whose ratio is the square of the scale factor in order to produce the same stress and strain distribution and, consequently, a similar displacement field. A certain actuator class is mechanically scalable if its output quantities follow the same rules, i.e. if (by proportional scaling in all directions) the actuator force is proportional to the square of the size and the actuator displacement is proportional to the size. Usually, a certain actuator class will be mechanically scalable only in a certain size range; beyond this range, the required actuator size changes with respect to the rest of the mechanical system, which can make the use of the considered type of actuator unpractical. Scalability is discussed for the considered actuator classes.

If the force is proportional to the area and the stroke to the length in the whole actuator's domain it follows that the work is proportional to the volume since the work is obtained from the integration of the force between two different strokes. If all these requirements are fulfilled and the actuator is fully scalable significant consequences arise. The structures working in the elastic region are considered fully scalable loads, the expression ruling its behavior $\sigma = E\varepsilon$ shows that the quotient between the stress $\sigma = F/A$ and the strain $\varepsilon = x/L$ is the Young Modulus E without dependence on the size of the structure. Therefore, if the actuator is shown to be scalable and the load is scalable in the sense described above, the whole system (actuator plus load structure) would be scalable, allowing the development of models of easy (normal size) construction as a preliminary step to the construction of large or small systems (inside the scalability range), with the corresponding saving of resources. In this case, the experimental results must be analyzed as non-dimensional numbers and provide information for all the range of sizes where the scalability can be assumed.

The requirements to keep the actuator force and work scalable are discussed. All the scalability analysis is based on some assumptions which are to be noted. In electromagnetical actuators the Nusselt[3] number is decisive and its influence on the scalability is discussed. Since the described assumptions are necessary to consider one actuator scalable, the non-scalability when these assumptions do not hold true is studied, too. The actuator performance as a function of the size is undertaken and conclusions are obtained for each actuator.

In the sixth step the results obtained are contrasted with dimensional analysis. Finally in the seventh step the theoretical results obtained are compared to the data from industrial actuators.

Chapter 3

Application to electromagnetic actuators

Before applying the described methodology to two particular classes of actuators (subsections 3.1 and 3.2), some general considerations about electromagnetic actuators are given.

Electromagnetic actuators are commonly used in many engineering fields. They have good force and work densities, although not as high as hydraulic actuators. They are easily controllable and the power source providing the energy can be placed as far away as necessary. Their use must be avoided when their environment must be free of electromagnetic fields or interferences. However, many technologies to deal with such effects are being developed.

The electrical circuit provides the current to the coils. This current flows through wires and produces heat due to the Joule effect. Different materials can be employed for the wires but usually copper, silver or aluminium are used because they present the lowest resistivities (Silver $1.59 \cdot 10^{-8}\ \Omega m$, Copper $1.68 \cdot 10^{-8}\ \Omega m$, Aluminium $2.65 \cdot 10^{-8}\ \Omega m$). Copper is the most commonly used material because of the cost. New technologies with superconductor materials (of extremely low resistivity) are being developed, but they are beyond the scope of this work. The magnetic circuit provides the flux and the force. Different materials can be used in the magnetic circuit depending on the magnetic permittivity.

The electromechanical actuators have an electrical and a magnetic circuit. Such circuits are built together, and therefore, the heat generated in the coils by Joule effect must flow through part of the magnetic circuit. The heat transfer circuit includes all the components of the actuator and depends on the geometry of each of them. Although different materials can be used in both the electric and magnetic circuit, it is common to talk about copper for the electric circuit and iron for the magnetic circuit.

Although some magnetic (demagnetization, saturation and magnetization hysteresis) and mechanical (friction and mechanical stress) effects are important in electromagnetical actuators, this work assumes that the temperature is the quantity that limits the available force. Therefore, to maximize the force, a study of the heat transfer phenomenon is to be done. Although there are losses caused by the magnetic hysteresis, eddy currents and friction, the resistive losses are dominant in the considered actuators operation, and hence, only such resistive losses are considered. An expression of the maximum current or current density allowed in an actuator in order to keep the temperature under the safety threshold has been developed. For the sake of simplicity, continuous operation (100 % duty cycle) has been assumed, nonetheless the case of non-continuous operation can be considered by using the RMS current. The model will be valid as long as the thermal transients are significantly slower than the mechanical. Otherwise (for fast temperature transients), the worst case should be considered, and thus, the maximum current of the cycle should be chosen instead of the RMS current.

Different actuators shapes and heat flow directions are discussed, and the expressions are later used to evaluate the maximum force of each actuator. First of all, the resistance of the coils of all the actuators is expressed as a function of the geometrical dimensions and the copper resistivity as:

$$R = \frac{\delta_{res} l_w}{A_w} = \frac{\delta_0 \left(1 + \gamma \Delta T\right) l_w}{A_w} \tag{3.1}$$

where γ is the resistivity temperature coefficient, δ_0 the resistivity at a given temperature T_0, $\Delta T = T_{max} - T_0$ the temperature increment, and l_w and A_w the length and cross-section of the wire. The steady-state heating balance equals the heat power produced in the coils due to the Joule effect with the heat power which the actuator can dissipate by means of conduction and convection as:

$$Ri^2 = \dot{Q} = \frac{\Delta T}{\vartheta_{cond} + \vartheta_{conv}} \tag{3.2}$$

where ϑ_{cond} is the thermal resistance by means of conduction and ϑ_{conv} is the thermal resistance by means of convection. The thermal resistance is defined in [3] as the temperature increment ΔT divided into the heat flow $\dot{Q}$. Since the electromagnetical actuators studied in this work present cylindrical shape, only this actuator shape will be considered. If the heat produced in the coils flows radially, the thermal resistances can be written as:

$$\vartheta_{cond} = \frac{log\left(r_{out}/r_{in}\right)}{2\pi L\lambda_{iron}} \tag{3.3}$$

$$\vartheta_{conv} = \frac{1}{2\pi L r_{out} h_c} \tag{3.4}$$

where L is the length of the actuator, λ_{iron} the conductivity of the iron, h_c the convection coefficient between the iron surface and the air, and r_{in} and r_{out} the internal and external radium of the pipe surrounding the actuator. If no pipe is surrounding the actuator there will be no heat transfer by means of conduction, and therefore, less thermal resistance.

From the heating balance (3.2) an expression of the maximum allowed current is obtained. The maximum current can be expressed as:

$$i_{max} = \sqrt{\frac{\Delta T}{R(\vartheta_{cond} + \vartheta_{conv})}} \tag{3.5}$$

Substituting the resistance obtained in (3.1) and the thermal resistances from (3.3) and (3.4) in the last expression, the maximum current can be written as:

$$i_{max} = \sqrt{\frac{A_w 2\pi L\Delta T}{\delta_0\left(1+\gamma\Delta T\right) l_w\left(\frac{log\left(\frac{r_{out}}{r_{in}}\right)}{\lambda_{iron}} + \frac{1}{r_{out}h_c}\right)}} \tag{3.6}$$

When the heat flows axially (moving coil actuator) without any conduction (since the air is surrounding de coils), the maximum current can be expressed as:

$$i_{max} = \sqrt{\frac{A_w \Delta T \pi (r_{out}^2 - r_{in}^2) h_c}{\delta_0 \left(1 + \gamma \Delta T\right) l_w}} \tag{3.7}$$

The conduction coefficient λ is a material property, but the convection coefficient h_c depends on the non-dimensional Nusselt number which is expressed in [3] as:

$$N_{u-L} = \frac{h_c L}{\lambda_{air}} \tag{3.8}$$

The Nusselt number can be written as a function of Reynolds, Prandtl and Grashof numbers, in [33] it is presented as:

$$N_u = C R_e^m P_r^n G_r^p \tag{3.9}$$

where R_e is the Reynolds number ($\rho v L/\eta$) which shows the relationship between the inertial forces and the viscous forces in the dynamics of a fluid, P_r is the Prandtl number ($\eta c/\lambda$) which characterizes the regime of convection, G_r is the Grashof number($\beta g \Delta T L^3/\nu^2$) analog to the Reynolds number when natural convection is concerned and C, m, n and p can take different values in forced convection ($C < 1, m < 1, n = 1/3, p = 0$) and natural convection ($C < 1, m = 0, n < 1/3, p < 1/3$). The Nusselt number can be in all the cases expressed as:

$$N_{u-r} = K_{Nu} r^{\alpha} \tag{3.10}$$

where K_{Nu} and α must be discussed in each case.

If it is not otherwise stated the values used in the numerical calculations done in this work are $\lambda_{air} = 0.0257\ W/Km$, $\lambda_{iron} = 80\ W/Km$, $\mu_0 = 1.25664 \cdot 10^{-6}\ Tm/At$, $\Delta T = 50\ K$, $\mu_r = 200$, $\mu_c = \mu_m = 1$, $H_c = 0.5 \cdot 10^6\ A/m$, $\rho_0 = 1.68 \cdot 10^{-8}\ \Omega m$ and $\gamma = 0.0068\ \Omega m/K$.

3.1 Solenoid actuators

Step 1. The solenoid actuators provide motion exciting a magnetic field where a plunger (movable part) tries to minimize the reluctance (i.e. the air gap) moving to the less reluctance position. The geometry is shown in Fig. 3.1. The non-dimensional constant k_ψ refer to ψ geometry dimensions of Fig. 3.1.

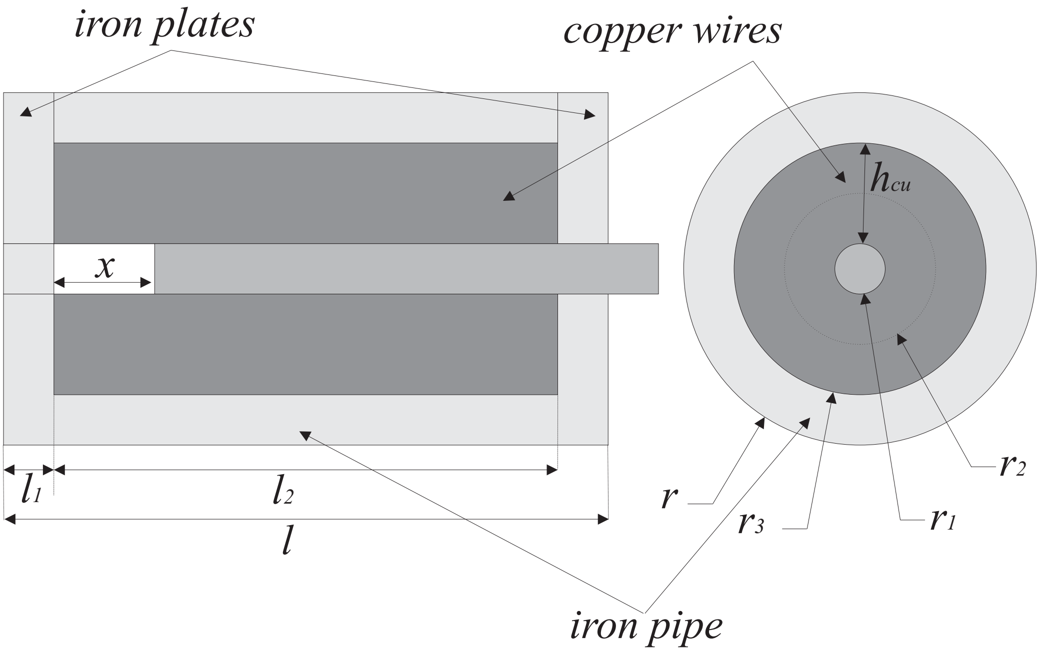

Figure 3.1: Solenoid actuator sketch

Step 2. The magnetic flux flowing inside a solenoid can be derived from the reluctance expression. It can be written as:

$$\Phi = \frac{F_{mm}}{\Re} = \frac{Ni}{\frac{x}{\mu_0 S} + \frac{l_2 + l_{eq} - x}{\mu_r \mu_0 S}} = \frac{Ni\mu_r\mu_0 S}{l_2 + l_{eq} + x\left(\mu_r - 1\right)} \tag{3.11}$$

where $\Re$ is the reluctance expressed as a function of the magnetic properties of the iron μ_r, the length l_2, the cross-section of the plunger $S = \pi r_1^2$ and the length l_{eq}, which is the plunger length with a reluctance equivalent to the reluctance of the plates and the pipe. F_{mm} is the magneto-motive force, equal to the number of turn N times the current i. The number of turns can be expressed as a function of the actuator dimensions as:

$$N = \frac{h_{cu} l_2 k_{ff}}{A_w} \tag{3.12}$$

where h_{cu} is the thickness of copper, l_2 the coil's length, k_{ff} the filling factor described in (2.3) and A_w the cross-section of a single wire. The solenoid force is produced for the change of reluctance due to the change of the air gap distance. Its expression can be derived from the energy stored in a solenoid $W_m = \int i d\lambda = \int N i d\Phi$. It yields:

$$F = \frac{dW_m}{dx} = \frac{S N^2 i^2 \mu_r^2 \mu_0}{2\left(l_2 + l_{eq} + \left(\mu_r - 1\right) x\right)^2} \tag{3.13}$$

The energy can be obtained integrating the force (3.13) between a given displacement x and 0 as:

$$W = \int_0^x F dx = \frac{S N^2 i^2 \mu_r^2 \mu_0 x}{2\left(l_2 + l_{eq} + \left(\mu_r - 1\right) x\right)\left(l_2 + l_{eq}\right)} \tag{3.14}$$

It can be seen that W is the total energy which the actuator stores in each position. This energy is transformed in work against a load and kinetic energy $W_k = (1/2) m v^2$, since this work focuses on the static behavior of the studied actuators, a quasi-static movement is considered. Therefore, if it is not otherwise stated all the energy is assumed to be transformed into work. The force-strokes curves can be seen in Fig. 3.2.

The force-stroke curves are presented when the input quantity (electrical current) is changed for different loads (one elastic load, equivalent to a structure, and one constant load). It can be seen how the operating points are changing depending on the input quantity and the load, when the current is increased working against an elastic load the working point is moving from E0 to E5. From the initial working point E0 the load can be moved to the other points depending on the input current. If a current $3i_0$ is applied the plunger moves from E0 to E3 and remains there. The work against a constant load presents more difficulties. When the current is not large enough the actuator cannot begin to move and remains blocked at the initial posi-

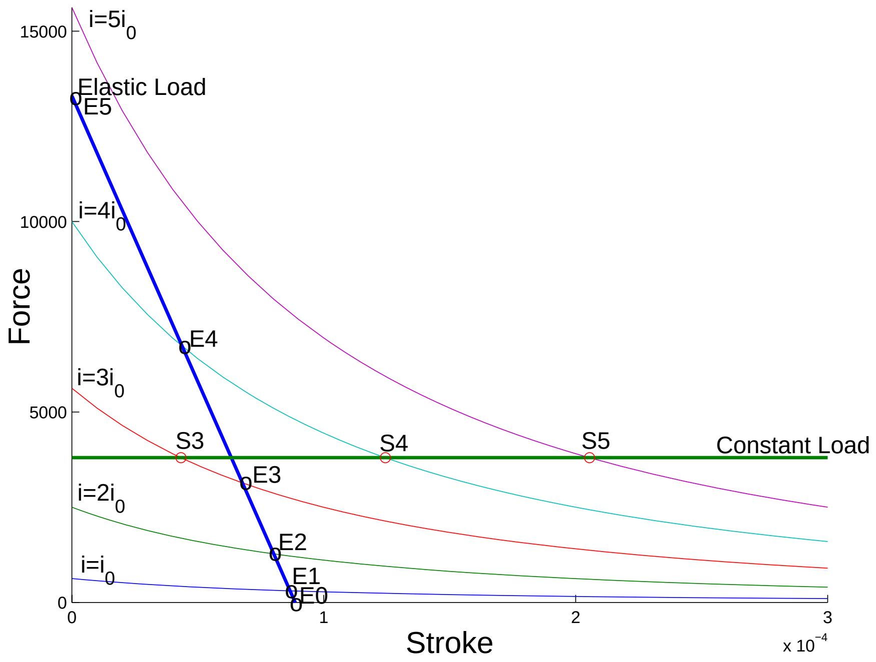

Figure 3.2: Force-Displacement curves for elastic and constant loads

tion, for this reason S1 and S2 do not appear in the curve and a minimum current $2.5i_0$ must be established to begin the traction. The force-stroke curves present hyperbolic behavior, with a horizontal asymptote tending to 0 as the distance increases and a vertical asymptote located in the negative stroke segment (physically unreachable).

Step 3. The general expressions obtained for electromagnetic actuators (3.13), (3.12) and (3.8) apply for solenoid actuators.

Step 4. Replacing the maximum current (3.6) in (3.13), using the number of turns given in (3.12), the convection coefficient of (3.8) and the geometrical expressions of (2.1) the maximum force (obtained when $x = 0$) can be expressed as:

$$\frac{F_{max}}{S_{act}} = \frac{\lambda_{air}\mu_0 \Delta T \mu_r^2}{\delta_0\left(1+\gamma\Delta T\right)} \frac{k_L^2 k_{r1}^2 \left(\frac{k_{r3}-k_{r1}}{k_{r2}}\right) k_{ff}}{\left(\frac{2k_\lambda \lambda_{air}}{\lambda_{iron}} + \frac{4}{Nu_D}\right)} \tag{3.15}$$

with $k_\lambda = log(1/k_{r3})$ and $k_L = l_2/(l_2 + l_{eq})$. The equivalent length ratio can be expressed as:

$$\frac{l_{eq}}{l} = \frac{k_{r1}^2(1-2k_{l1})}{1-k_{r3}^2} + \frac{k_{r1}^2\eta^2 log\frac{1}{k_{r1}}}{k_{l1}} \tag{3.16}$$

It can be noted that the maximum force divided into the cross-section of the actuator is expressed as a function of material constants, physical thresholds and geometrical relationships. A design factor depending on the design parameters can be defined from (3.15) as:

$$q_f = k_L^2 k_{r1}^2 \left(\frac{k_{r3}-k_{r1}}{k_{r2}}\right) k_{ff} \tag{3.17}$$

Substituting all the terms in the last expression it can be written as:

$$q_f = \frac{k_{l2}^2 2k_{r1}^2 k_{ff}\frac{k_{r3}-k_{r1}}{k_{r3}+k_{r1}}}{\left(k_{l2} + \frac{k_{r1}^2 k_{l2}}{1-k_{r3}^2} + \frac{k_{r1}^2\eta^2 log\frac{1}{k_{r1}}}{(1-k_{l2})/2}\right)^2} \tag{3.18}$$

The expression (3.18) has been analyzed numerically. The best design parametrization has been found for values $k_{r1} = 0.34$, $k_{r3} = 0.76$, $k_{l2} = 0.50$ and $\eta < 0.1$. The optimized found design factor is $q_f = 0.0402$.

In Fig. 3.3 the design factor q_f depending on the ratios k_{r1} and k_{r3} is plotted. The aspect ratio η, the ratio r_{l1} and the filling factor are kept constant to allow a three-dimensional plot. The filling factor k_{ff} is typically around 0.75 and can be considered independent of the other design parameters. Regarding the aspect ratio, in (3.18) it is shown that a large η implies a low design factor q_f, but its importance depends on the other terms on the denominator. It has been seen that below aspect ratios of 0.1 the improvement of the design factor is insignificant. In Fig. 3.3 it can be seen that k_{r1} values between 0.3 and 0.4 provide the best performance for k_{r3} values between 0.7 and 0.8. In Fig. 3.4 the design factor behavior depending on k_{l2} and k_{r3} with a constant $k_{r1} = 0.34$ is presented. The plot shows that high design factors are obtained for k_{r3} values between 0.7 and 0.8 and in a wide range $(0.1-0.9)$ of k_{l2}.

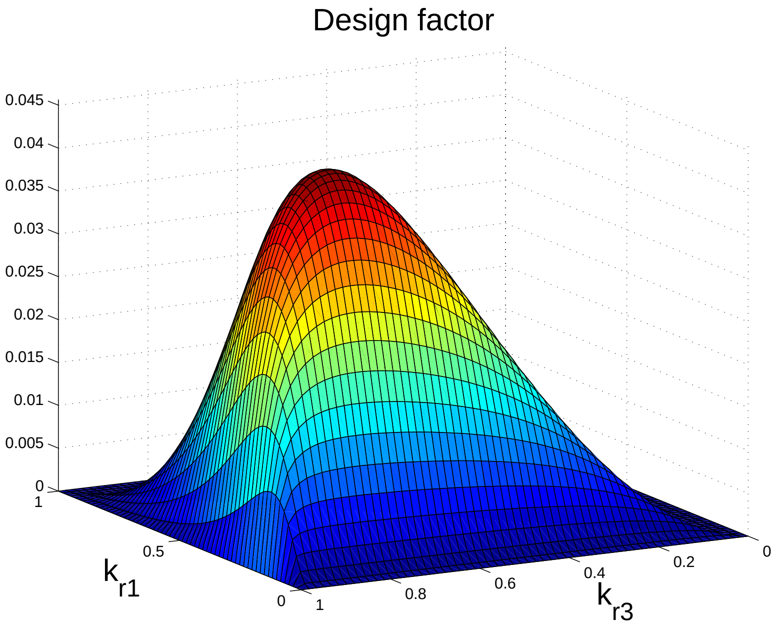

Figure 3.3: Solenoid design factor depending on k_{r1} and k_{r3} with $k_{l2} = 0.5$ and $\eta = 0.1$

The maximum displacement is l_2 and is proportional to the length of the actuator l since $l_2 = k_{l2} l$. The maximum volumetric work is achieved when the whole displacement is done. It can be obtained integrating the force. The maximum work expression found yields:

$$\frac{W_{max}}{V_{act}} = \frac{q_f \lambda_{air} \mu_0 \Delta T \mu_r^2 \frac{k_L}{(1/k_L + \mu_r - 1)}}{\delta_0 \left(1 + \gamma \Delta T\right) \left(\frac{2 k_\lambda \lambda_{air}}{\lambda_{iron}} + \frac{4}{Nu_D} \right)} \tag{3.19}$$

The discussion undertaken for the force optimum design parametrization applies for the work, too.

Step 5. If the l_{eq}/l ratio is kept constant in (3.15) and (3.19) the scalability will depend only on the Nusselt number. If the Nusselt number is assumed to be constant ($\alpha = 0$), the force will be independent of the actuator length and it will be proportional to the cross-section. The work will be proportional to both the length and the cross-section, and therefore to the volume so that a constant volumetric energy will be shown. Such an assump-

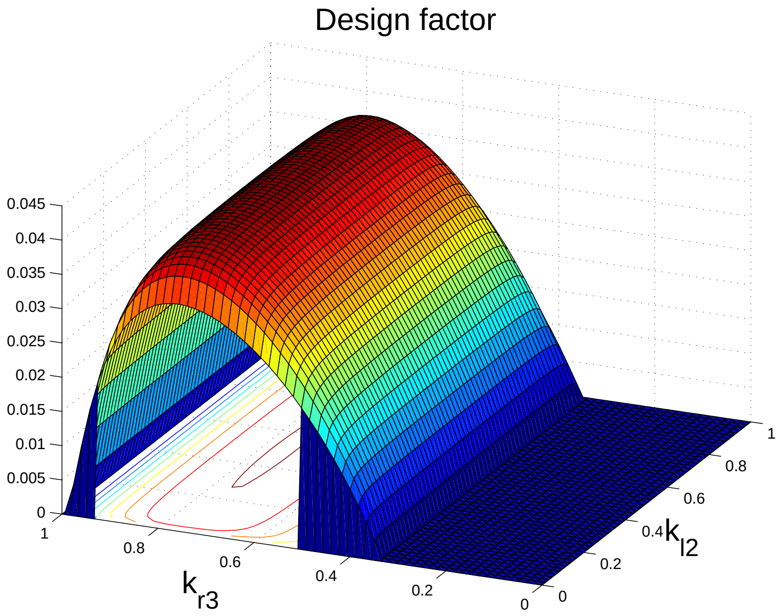

Figure 3.4: Solenoid design factor depending on k_{l2} and k_{r3} with $k_{r1} = 0.34$ and $\eta = 0.1$

tion cannot generally be done when studying the different convection cases. With a positive value of α (which is the behavior observed) the actuator force and work are not scalable anymore and their maximum performance values are increased when the size is increased. In such a case the maximum force per cross-section can be expressed as:

$$\frac{F_{max}}{S_{act}} = k_a \frac{r^\alpha}{k_b + r^\alpha} \tag{3.20}$$

It can be noted that for high values of r the maximum force tends to be scalable since $\lim\limits_{r \to \infty} k_a r^\alpha / (k_b + r^\alpha) = k_a$. It can also be observed in Fig. 3.5. For tiny actuators the force and work are strongly unscalable and the performance becomes worse. It may explain that these actuators are not used when a small actuator is required.

Step 6. The force provided by these actuators can be analyzed with dimensional analysis using the Buckingham Pi Theorem [5], the quantities involved are shown in the Table 3.1. The $FLTI\theta$ (force - length - time -

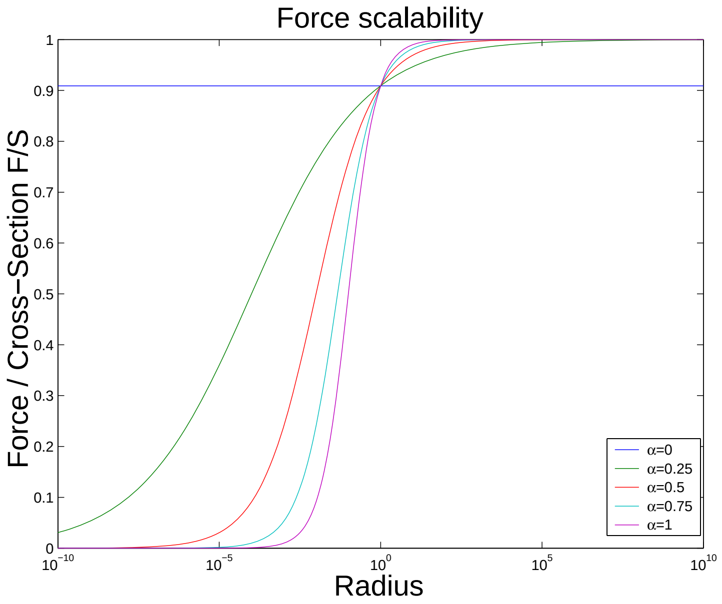

Figure 3.5: Solenoid force scalability for different α coefficients in the Nusselt number expression

current - temperature) system is used.

Table 3.1: Solenoid actuator dimensional analysis quantities

F	Force	$[F]$
x	Position	$[L]$
μ	Permeability	$[FI^{-2}]$
h_c	Convection Coef.	$[FL^{-1}T^{-1}\theta^{-1}]$
λ	Conduction Coef.	$[FT^{-1}\theta^{-1}]$
δ	Resistivity	$[FL^2I^{-2}T^{-1}]$
T	Temperature	$[\theta]$

The results show that the maximum force can be expressed as:

$$\frac{F}{x^2} = K\frac{\mu T\lambda}{\delta}\Phi\left(N_u\right) \tag{3.21}$$

where it can be observed that it matches perfectly with (3.15) since $\delta = \delta_0\left(1+\gamma\Delta T\right)$ and μ_r and all the geometrical constants are adimensional. The results obtained for the work match with the expression (3.19), the maximum work given by dimensional analysis can be expressed as:

$$\frac{W}{x^3} = K\frac{\mu T\lambda}{\delta}\Phi\left(N_u\right) \tag{3.22}$$

3.2 Moving coil actuators

Step 1. The geometric dimensions are shown in Fig. 3.6. For the sake of simplicity and without loss of generality it has been assumed that $l_1 = l_2 = l_3$.

Step 2. Moving coil actuators use the force produced by the interaction of perpendicular magnetic field and electrical current, described in the Lorenz force law. It yields:

$$F = Bl_w i \tag{3.23}$$

where B is the field density provided by the permanent magnet, l_w is the length of the wire and i the current flowing in the wire.

The present work assumes that the moving coil stroke is limited to the region where the flux is flowing, so that the force-stroke curve presents a constant force depending linearly on the current applied to the coil. The work is obtained by the integration of a constant function. Without the assumption of limited stroke, the length of wire l_w being crossed by magnetic flux decreases as the coil is moving outside the flux region, whereas the flux density and the current are kept constant since the copper permittivity can be considered equal to the air permittivity.

The flux density B in the coil can be derived from the reluctance expression. In this case the magneto-motive force is provided by the permanent magnet $F_{mm} = H_c l$, where H_c is the coercitive field (a magnet constant). The reluctance can be calculated as the series association of all the reluctances sketched in Fig. 3.7. The total reluctance of the magnetic circuit can be expressed as:

$$\Re = \frac{\log\left(\frac{k_{r2}^{\frac{1}{k_{l1}}-\frac{\mu_r}{\mu_{cu}k_{l4}}} k_{r4}^{\frac{\mu_r-1}{k_{l1}}}}{k_{r1}^{\frac{2}{k_{l1}}} k_{r3}^{\frac{\mu_r}{k_{l1}}-\frac{\mu_r}{\mu_{cu}k_{l4}}}}\right) + \frac{2(1-2k_{l1})}{\left(1-k_{r5}^2\right)\eta^2} + \frac{2}{\frac{\mu_m}{\mu_r}k_{r1}^2\eta^2}}{\mu_r\mu_0 2\pi l} \tag{3.24}$$

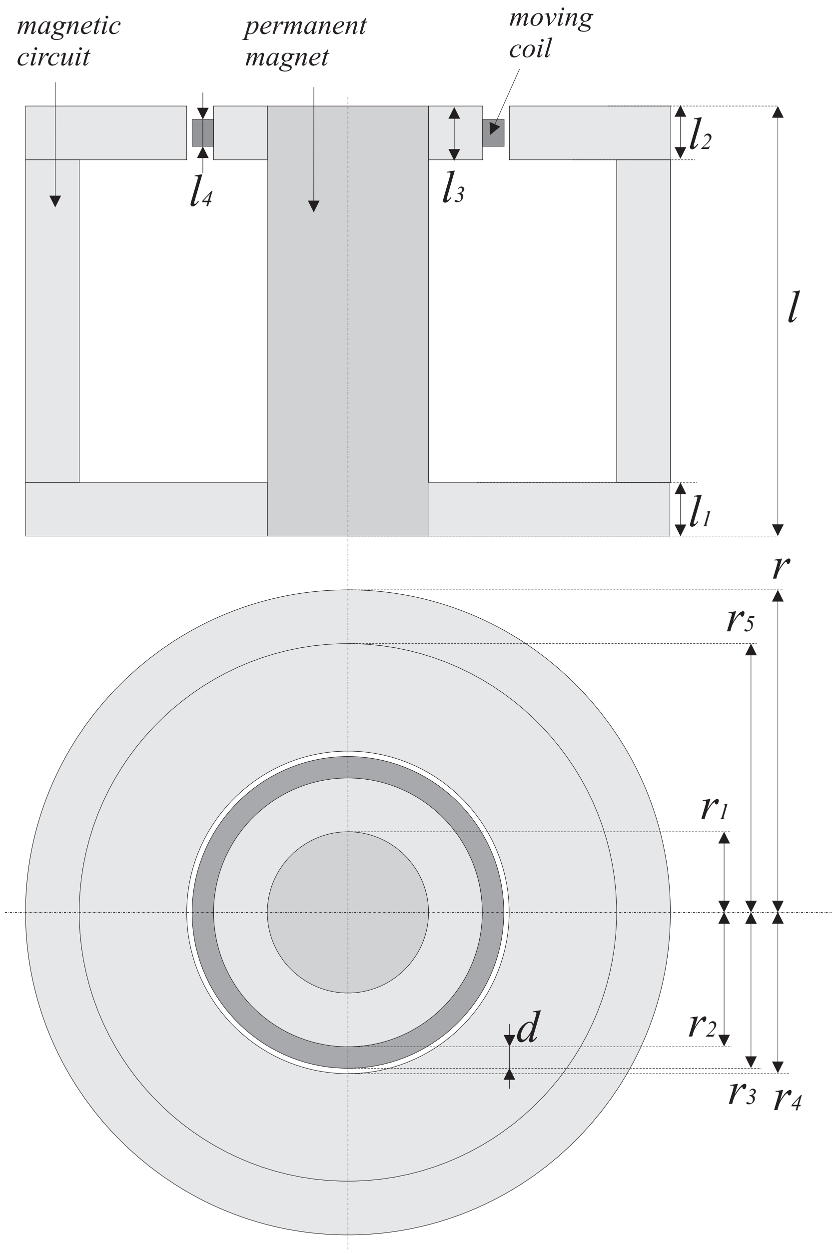

Figure 3.6: Moving coil actuator sketch

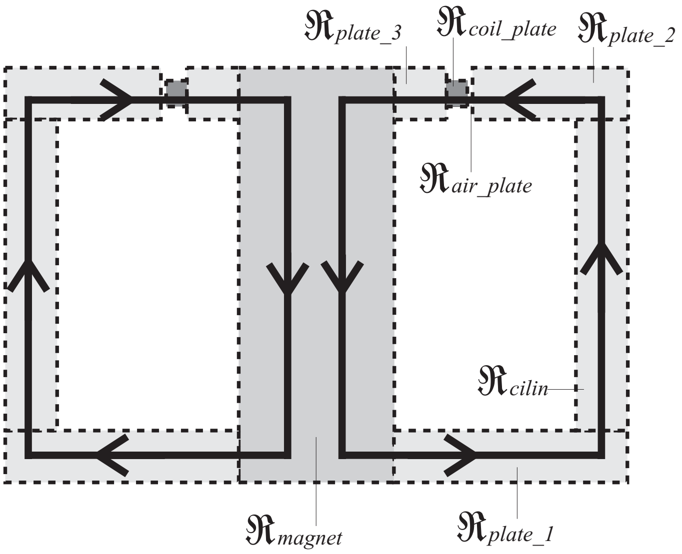

Figure 3.7: Moving coil actuator reluctances

The flux density ($B = \Phi/S$) can be written as:

$$B = \frac{H_c l/\Re}{r_3 l_4} = \frac{H_c}{r \Re k_{r3} k_{l4}} \tag{3.25}$$

The number of turns can be expressed as a function of the actuator dimensions as:

$$N = \frac{d l_4 k_{ff}}{A_w} = \frac{(r_3 - r_2) l_4 k_{ff}}{A_w} \tag{3.26}$$

The length l_w used in (3.23) can be expressed as:

$$l_w = 2\pi \frac{r_3 + r_2}{2} N = \pi r^2 l \frac{(k_{r3}^2 - k_{r2}^2) k_{l4} k_{ff}}{A_w} \tag{3.27}$$

Since the permanent magnet is always providing the same magnetomotive force, and the length of wire crossed by the flux is constant, the force from (3.23) can be considered proportional only to the current.

Step 3. The maximum current in the coil can be taken from (3.7). In such a case there is no conduction because the coil can exchange heat directly with the air surrounding it. Substituting l_w, the Nusselt number from (3.8), using the external diameter of the coil $2r_3$ as the reference length and arranging, the maximum current can be written as:

$$i_{max} = \frac{A_w}{\sqrt{rl}} \sqrt{\frac{\Delta T N_u \lambda_{air}}{2\delta_0 \left(1 + \gamma \Delta T\right) k_{l4} k_{r3} k_{ff}}} \tag{3.28}$$

Step 4. Using the maximum current from (3.28), the length from (3.27) and the flux density from (3.25), the force expression (3.23) turns into:

$$\frac{F_{max}}{S_{act}} = q_f H_c \mu_r \mu_0 \sqrt{\frac{\Delta T N_u \lambda_{air}}{2\delta_0 \left(1 + \gamma \Delta T\right)}} \tag{3.29}$$

where q_f is the design factor which can be expressed as:

$$q_f = \frac{\frac{2\pi}{\sqrt{\eta}}(k_{r3}^2 - k_{r2}^2)\sqrt{\frac{k_{ff}}{k_{r3}^3 k_{l4}}}}{\log\left(\frac{k_{r2}^{\frac{1}{k_{l1}} - \frac{\mu_r}{\mu_{cu} k_{l4}}} k_{r4}^{\frac{\mu_r - 1}{k_{l1}}}}{k_{r1}^{\frac{2}{k_{l1}}} k_{r3}^{\frac{\mu_r}{k_{l1}} - \frac{\mu_r}{\mu_{cu} k_{l4}}}}\right) + \frac{2(1-2k_{l1})}{\left(1-k_{r5}^2\right)\eta^2} + \frac{2}{\frac{\mu_m}{\mu_r} k_{r1}^2 \eta^2}} \tag{3.30}$$

The expression (3.30) has been analyzed numerically in order to obtain the most optimum parametrization. It has been found with values $k_{r1} = k_{r2} = k_{r5} = 0.8586$, $k_{r3} = k_{r4} = 1$, $k_{l1} = k_{l4} = 0.50$ and $\eta = 6.0606$. The optimized design factor obtained is $q_f = 0.0108$.

In Fig. 3.8 the design factor q_f depending on the ratios k_{r1} and η is plotted. The filling factor and the other geometric relationships are kept constant to allow a three-dimensional plot. The filling factor k_{ff} is typically around 0.75 and can be considered independent of the other design parameters.

It has been assumed that the coil movement is limited to the region where the whole coil is being crossed by the magnetic flux provided by the permanent magnet. Therefore, the available stroke is $l_1 - l_4$, which can be written as $l\left(k_{l1} - k_{l4}\right)$. Since the force does not depend on the displacement in this region, the work can be easily obtained multiplying the force times the displacement as:

$$\frac{W_{max}}{V_{act}} = F_{max}\left(k_{l1} - k_{l4}\right) \tag{3.31}$$

A modified design factor $q_{fW} = q_f\left(k_{l1} - k_{l4}\right)$ is to be analyzed to obtain

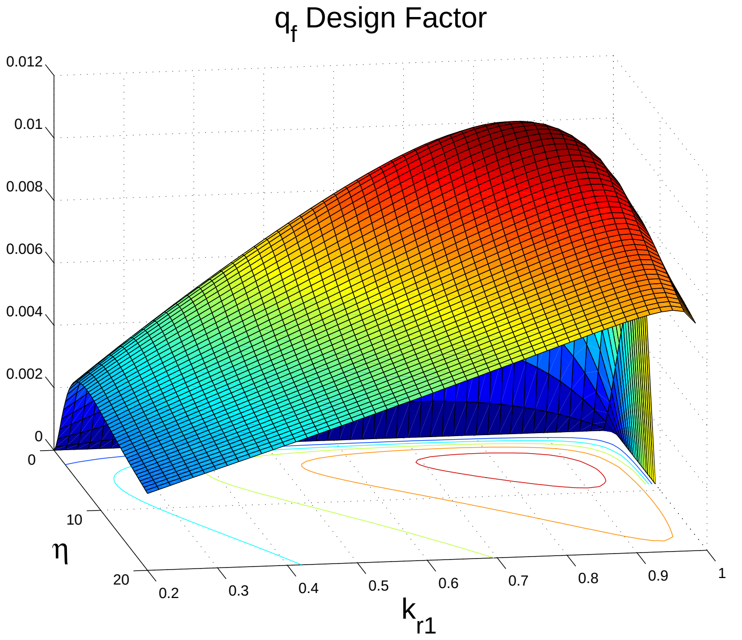

Figure 3.8: Moving coil design factor depending on η and k_{r1} with $k_{r3} = 1$ and $k_{l1} = k_{l4} = 0.5$

the best performance design concerning the work. It can be easily seen that the design parameters providing maximum force produce no work because they are using the maximum coil width $k_{l4} = k_{l1} = 1/2$, allowing no stroke. A numerical analysis has been undertaken to obtain the optimum modified design factor. The best performance values has been found with $k_{r1} = k_{r2} = k_{r5} = 0.8283$, $k_{r3} = k_{r4} = 1$, $k_{l1} = 0.50$, $k_{l5} = 0.0960$ and $\eta = 2.0202$. The optimized design factor obtained is $q_{fW} = 0.0029$.

Step 5. Regarding the scalability, it can be seen that the force and work depend on the Nusselt number, while the stroke can be considered completely scalable. As it has been discussed, if the Nusselt number is considered constant all the output mechanical quantities can be considered scalable. Nonetheless, this assumption cannot be done and it is observed that both the force per cross-section and the volumetric work density depend linearly on $\sqrt{N_u}$. Hence, the cited output quantities present a linear dependence on $r^{\alpha/2}$, implying an improvement of the performance when the size is increased

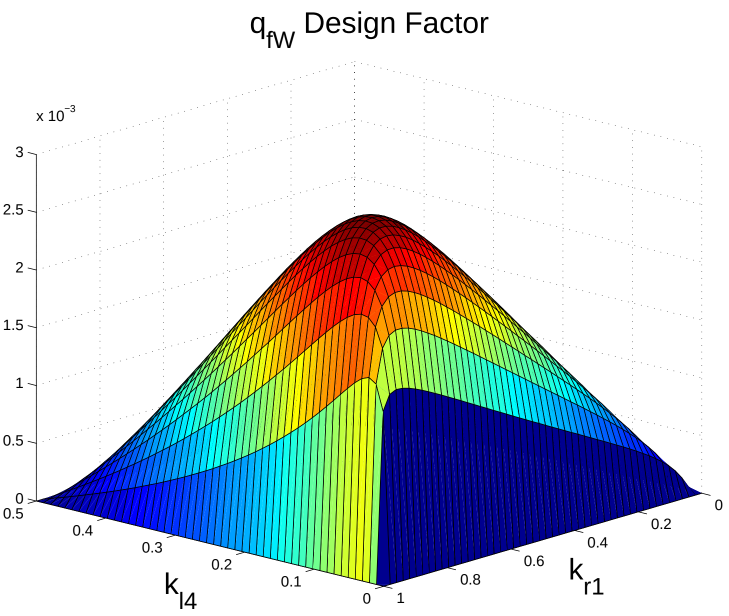

Figure 3.9: Moving coil work modified design factor depending on k_{r1} and k_{l4} with $k_{l1} = 0.5$ and $\eta = 2$

and not allowing the use of these actuators for tiny applications.

Step 6. The force provided by these actuators can be analyzed with dimensional analysis using the Buckingham Pi Theorem [5]. The quantities involved are shown in the Table 3.2. The $FLTI\theta$ (force - length - time - current - temperature) system is used.

Table 3.2: Moving coil actuator dimensional analysis quantities

F	Force	$[F]$
x	Position	$[L]$
μ	Permeability	$[FI^{-2}]$
H	Magnetic Field Intensity	$[IL^{-1}]$
h_c	Convection Coef.	$[FL^{-1}T^{-1}\theta^{-1}]$
λ	Conduction Coef.	$[FT^{-1}\theta^{-1}]$
δ	Resistivity	$[FL^2I^{-2}T^{-1}]$
T	Temperature	$[\theta]$

The results show that the maximum force can be expressed as:

$$\frac{F}{x^2} = K\mu H\sqrt{\frac{T\lambda N_u}{\delta}} \tag{3.32}$$

where it can be observed that it matches perfectly with (3.29) since $\delta = \delta_0\left(1+\gamma\Delta T\right)$ and μ_r and all the geometrical constants are non-dimensional. The results obtained for the work match with the expression (3.31). The maximum work given by dimensional analysis can be expressed as:

$$\frac{W}{x^3} = K\mu H\sqrt{\frac{T\lambda N_u}{\delta}} \tag{3.33}$$

3.3 Industrial actuators

Step 7. Since the electromagnetical actuators are often cooled with air by means of free convection, a numerical analysis is presented assuming natural convection. In such case the Nusselt number can be written as a function of the Rayleigh number in the form $N_{uD} = CR_a^n$ where C and n are to be discussed for different values of R_a as it is exposed in [33]. It has been found (assuming an air temperature of 293 K and a temperature increment of 50 K) that for diameters between 2.6 mm and 0.124 m the coefficients $C = 0.48$ and $n = 1/4$ can be used, while for diameters between 0.124 m and 5.75 m, $C = 0.125$ and $n = 1/3$ can be used. This range of diameters covers all the industrial electromagnetical actuators found, but other ranges can be considered using other coefficients. The Nusselt numbers can be written as:

$$N_{u_D} = \begin{cases} 129.20 \cdot D^{1/4} & 0.0026 < D < 0.124\ m \\ 217.25 \cdot D^{1/3} & 0.124 \le D < 5.75\ m \end{cases} \tag{3.34}$$

Different manufactured industrial solenoids and moving coil actuators have been studied. Its output mechanical quantities compared to the maximum quantities developed in this work are shown in Fig. 3.10. The maximum quantities have been calculated using the design factor $q_f = 0.04$ for the solenoids and $q_f = 0.0108$, $q_{fW} = 0.0029$ for the moving coils.

It can be seen that the solenoid actuator perform better force per cross-section ratios, between 1 and 2 orders of magnitude, while the difference in energy densities is smaller (less than one order of magnitude). The data from industrial actuators have been analyzed and approached using a linear regression after taking logarithms of the quantities concerned. The force provided by the solenoid actuators has been approached with the function $9.35 \cdot 10^6 r^{2.3336}$. The moving coil actuator has been approached with the function $4.59 \cdot 10^4 r^{2.1270}$. It has been stated that the limiting force for the solenoid holds $F \propto r^2 Nu$. Therefore, the α coefficient should be located between 2.25 and 2.333 (according to (3.34), $2{+}1/4$ and $2{+}1/3$). It matches with the α coefficient 2.3336 obtained with the regression. The same can be said for the moving coil, where the force holds $F \propto r^2\sqrt{Nu}$. In such a case, the $\alpha = 2.1270$ coefficient is also located between 2.125 and 2.166.

The solenoid work has been fitted with $1.369 \cdot 10^5 V^{1.167}$, where the coefficient is close to the expected between 1.083 and 1.111 ($1 + \frac{1/4}{3}$ and $1 + \frac{1/3}{3}$). The moving coil work has been approached with $8.775 \cdot 10^3 V^{1.129}$, slightly higher than the expected between 1.041 and 1.056.

As shown in the regression analysis and in Fig. 3.10 and Fig. 3.11, it can be concluded that the behavior of the industrial actuators follows the trends developed theoretically and are limited by the maximum mechanical quantities described.

3.4 Conclusions

The present chapter has dealt with the optimization of linear electromagnetical actuators. A procedure to obtain the maximum energy and force in a given volume, weight or cross-section has been described. The scalability of the analyzed actuators has been also discussed. It has been shown that solenoid and moving coil actuators are suitable for a number of applications excluding those where tiny actuators are required or a high scalability is to be kept. Solenoid actuators can perform higher force per cross-section and energy per volume than the moving coil actuators, but they face the problems derived from non-linear force-stroke curves. This problem can be

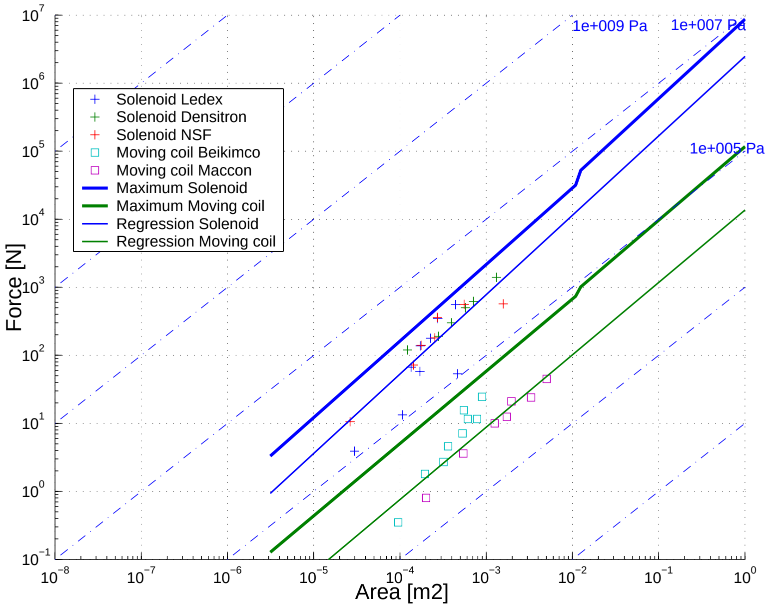

Figure 3.10: Industrial electromagnetic actuator force-area comparison

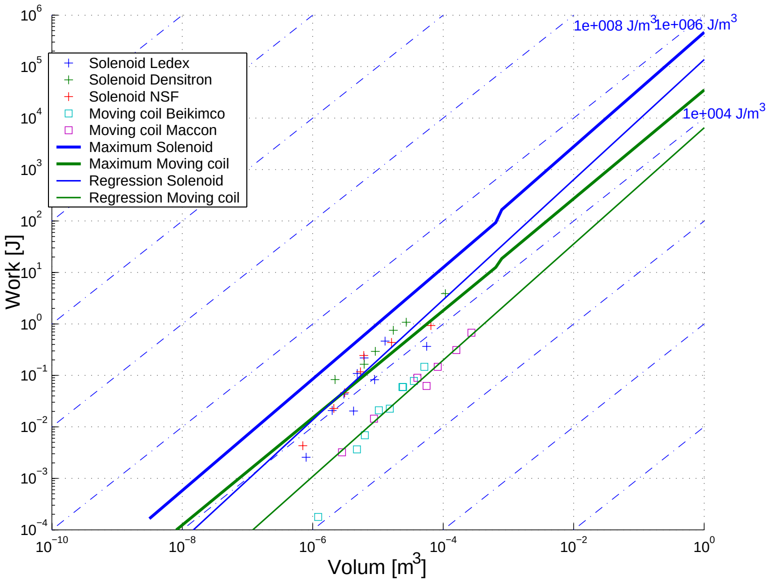

Figure 3.11: Industrial electromagnetic actuator work-volume comparison

overcome by using certain design techniques including some high reluctance parts which are beyond the scope of this work.

The limit output quantities have been found for certain aspect ratios and geometric relationships. The results have been compared with the performance of industrial actuators and it has been noted that the industrial actuators behave as expected. Regressions linking the force and work with the cross-section and volume have been carried out, resulting in similar performances as a function of the size as the theoretically developed models.

The results can be used in any application with volume and weight constraints. For given volume or weight constraints, the presented expressions can show whether the studied electromagnetic actuators match the requirements and what materials and shapes are needed.

Chapter 4

Application to hydraulic actuators

Fluid power actuators use the fluid power to provide mechanical work; the difference between the pressures P in two different chambers results in a relative pressure which produces a force F in a given surface S which yields $F = PS$. The pressure is the input quantity, performing the same function as the current in electromechanical actuators. The fluid actuators employed in the industry are mainly divided by the state of the fluid employed: *hydraulic actuators* employ an incompressible liquid (usually oil), while *pneumatic actuators* employ a compressible gas (air).

Hydraulic actuators are commonly used in many engineering fields. They show the following advantages: very good force and work densities (more than any other actuator), strokes as long as necessary (if enough fluid is supplied), easily controllable and the fact that the power source providing the energy can be placed far away from the actuator (but not as far as with the electromagnetic actuators). Their main disadvantages are the safety problems generated by the high pressures needed (the same fact that provides the advantages), the leakage flow (that can become an important problem for actuator performance, safety conditions and environmental issues) and the hardly inflammability of the oil employed. Pneumatic actuators are also used in many engineering fields. They present good force and work densities, even though not as high as the hydraulic actuators, they can perform strokes as long as needed like their hydraulic counterparts, they are easily controllable and the power source providing the energy can be placed far away from the actuator. However, they cannot work with pressures as high as the hydraulic actuators because of the problems derived from the high compressibility of the gases. This same fact makes the hydraulic actuators faster in response and stiffer against external load disturbances. The efficiency of the hydraulic systems is also higher. It is caused by the losses of energy due to the heat transfer (in the air cooling), higher leakage and worse lubrication which occurs in the pneumatic systems. Nevertheless, the pneumatic systems can work at higher environment temperatures. In the present work, the hydraulic actuators are studied. However, some of the results obtained also apply for their pneumatic counterparts.

In this work an ideal power supply with no losses will be considered, it implies that the load will not change the supplied pressure and it can be assumed with no loss of generality if the power of the power supply is larger than the nominal power consumed by the actuator. The methodology described in chapter 2 is applied below.

4.1 Step 1. Design parameters

In Figure 4.1 a hydraulic actuator is sketched. It can be seen that for $x = 0$ both orifices are completely closed, when $x > 0$ follows $P_1 > P_2$ since $P_s > P_r$, and the plunger moves forward, when $x < 0$ follows $P_2 < P_1$ and it moves backward. The sections can be written as $A_1 = \pi D_1^2/4$ and $A_2 = \pi/4\,(D_1^2 - D_2^2)$ where D_1 is the diameter of the cylinder and D_2 is the diameter of the rod which guides the plunger.

The geometry of hydraulic cylindrical actuators is shown in Figure 4.2. The same geometry would be valid for pneumatic actuators, with the only difference of the fluid used and the corresponding limitations.

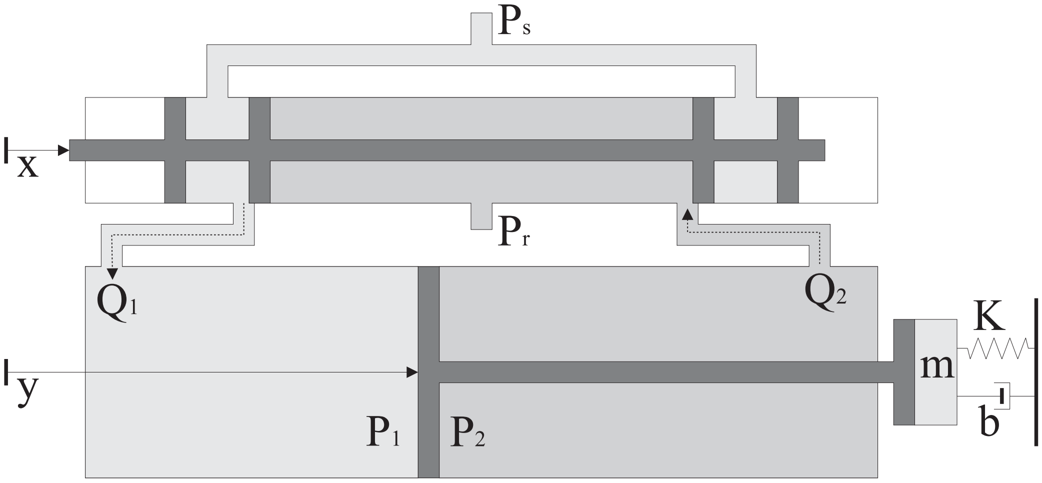

Figure 4.1: Hydraulic Actuator

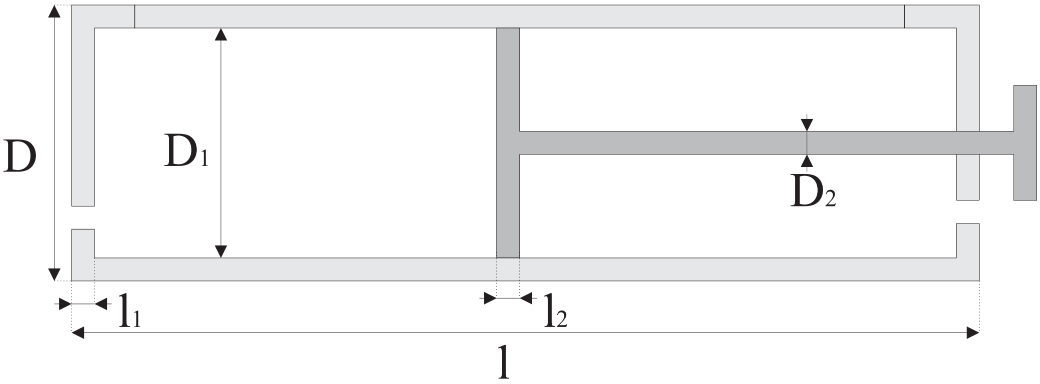

Figure 4.2: Geometry of a hydraulic actuator

4.2 Step 2. Force-stroke and work-stroke characteristic

The cylinder force can be expressed as $F = P_1 A_1 - P_2 A_2$ where P$_i$ is the pressure in the chamber i and A$_i$ is the effective section of the piston. It can be expressed as:

$$F = P_1 \pi \frac{D_1^2}{4} - P_2 \pi \frac{(D_1^2 - D_2^2)}{4} \tag{4.1}$$

The force performed by the cylinder in steady-state conditions depends on whether the movement is done forward or backward, since the section is different. Assuming $P_2 = P_r = 0$ and $P_1 = P_s$, the forward force can be expressed as :

$$F_f = P_s \pi D_1^2 / 4 \tag{4.2}$$

Concerning the backward force, $P_2 = P_s$ and $P_1 = P_r = 0$. The force yields:

$$F_b = P_s \pi \left(D_1^2 - D_2^2 \right) / 4 \tag{4.3}$$

Assuming quasistatic behaviour the work can be obtained assuming the force is constant during the time and therefore multiplying the force times the displacement.

4.3 Step 3. Limiting quantities.

The maximum allowed shear stress is the main quantity limiting the available mechanical force and work. It can be expressed using the Mohr circle as half the difference between the radial and tangential stresses. The radial stress in a thick walled cylinder can be written from [49] as a function of the position r in the wall as follows:

$$\sigma_{rr} = \frac{P D_1^2}{D^2 - D_1^2} \left(1 - \frac{D^2}{4 r^2} \right) \tag{4.4}$$

The tangential stress in a thick walled cylinder from [49] yields:

$$\sigma_{\theta\theta} = \frac{PD_1^2}{D^2 - D_1^2}\left(1 + \frac{D^2}{4r^2}\right) \tag{4.5}$$

The equivalent shear stress can be derived from (4.4) and (4.5) as:

$$\tau_{eq} = \frac{\sigma_{rr} - \sigma_{\theta\theta}}{2} = \frac{PD_1^2}{D^2 - D_1^2}\frac{D^2}{4r^2} \tag{4.6}$$

It can be clearly seen in (4.6) that the maximum shear stress is produced for the minimum value of r, i.e. $r = D_1/2$. Using the defined geometric relationships the maximum shear stress yields:

$$\tau_{eq} = \frac{P}{1 - k_{D1}^2} \tag{4.7}$$

Hence, to not overcome the shear stress threshold, the maximum pressure must be established as:

$$P_{L1} = \tau_{eq}\left(1 - k_{D1}^2\right) \tag{4.8}$$

For backward motion, there arises another fact: there exists a maximum axial stress σ_{aa} in the rod attaching the load. It implies another pressure limitation:

$$P_{L2} = \sigma_{aa} k_{D2}^2 \tag{4.9}$$

Then, the maximum pressure for backward motion P_{Lb} can be written as:

$$P_{Lb} = min\{P_{L1}, P_{L2}\} = min\{\tau_{eq}\left(1 - k_{D1}^2\right), \sigma_{aa} k_{D2}^2\} \tag{4.10}$$

Defining $\varphi = \sigma_{aa}/\tau_{eq}, \varphi > 0$, it may be expressed as:

$$P_{Lb} = \tau_{eq} min\{\left(1 - k_{D1}^2\right), \varphi k_{D2}^2\} \tag{4.11}$$

4.4 Step 4. Maximum force, stroke and work.

4.4.1 Forward motion

Using (4.8) and (4.2), the maximum available force per cross-section can be expressed for the forward motion as:

$$\frac{F_f}{\pi D^2/4} = \tau_{eq}\left(1 - k_{D1}^2\right) k_{D1}^2 \tag{4.12}$$

The design factor q_f can be defined as:

$$q_f = \left(1 - k_{D1}^2\right) k_{D1}^2 \tag{4.13}$$

and is the factor to be maximized in the design.

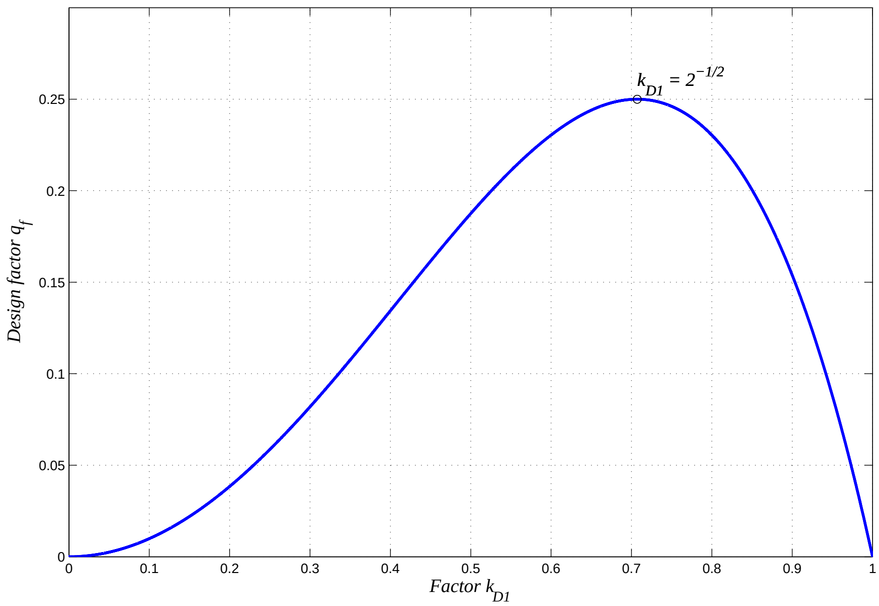

Figure 4.3: Forward force design factor

Analyzing the latter expression, it can be seen that for a given size the forward force is maximized for $k_{D1} = 1/\sqrt{2}$ performing a force per cross section of $\tau_{eq}/4$ with a design factor $q_f = 1/4$. Graphical results may be seen in Fig. 4.3.

4.4.2 Backward motion

Using (4.11) and (4.3), the maximum available force per cross-section can be expressed for the backward motion as:

$$\frac{F_f}{\pi D^2/4} = \tau_{eq} min\{\left(1 - k_{D1}^2\right), \varphi k_{D2}^2\} \left(k_{D1}^2 - k_{D2}^2\right) \tag{4.14}$$

An alternative formulation yields:

$$\frac{F_f}{\pi D^2/4} = \begin{cases} \tau_{eq} \left(1 - k_{D1}^2\right) \left(k_{D1}^2 - k_{D2}^2\right) & 1 - k_{D1}^2 < \varphi k_{D2}^2 \\ \tau_{eq} \varphi k_{D2}^2 \left(k_{D1}^2 - k_{D2}^2\right) & 1 - k_{D1}^2 \geq \varphi k_{D2}^2 \end{cases} \tag{4.15}$$

The design factor $q_f = 4F_f/\tau_{eq}\pi D^2$ may be defined as:

$$q_f = \begin{cases} \left(1 - k_{D1}^2\right) \left(k_{D1}^2 - k_{D2}^2\right) & 1 - k_{D1}^2 < \varphi k_{D2}^2 \\ \varphi k_{D2}^2 \left(k_{D1}^2 - k_{D2}^2\right) & 1 - k_{D1}^2 \geq \varphi k_{D2}^2 \end{cases} \tag{4.16}$$

Analyzing the expression (4.16), the maximum design factor may be found by using $1 - k_{D1}^2 = \varphi k_{D2}^2$ or its equivalent formulation $k_{D2} = \sqrt{\left(1 - k_{D1}^2\right)/\varphi}$. In such a case:

$$q_f = \left(1 - k_{D1}^2\right) \left(k_{D1}^2 - 1 + k_{D1}^2/\varphi\right) \tag{4.17}$$

It can be expressed as:

$$q_f = -\frac{\varphi + 1}{\varphi} k_{D1}^4 + \frac{2\varphi + 1}{\varphi} k_{D1}^2 - 1 \tag{4.18}$$

To obtain the maximum design factor:

$$\dot{q}_f = -4\frac{\varphi + 1}{\varphi} k_{D1}^3 + 2\frac{2\varphi + 1}{\varphi} k_{D1} \rightarrow 4\frac{\varphi + 1}{\varphi} k_{D1max}^3 = 2\frac{2\varphi + 1}{\varphi} k_{D1max} \tag{4.19}$$

The maximum k_{D1max} yields:

$$k_{D1max} = \sqrt{\frac{2\varphi+1}{2\varphi+2}} \tag{4.20}$$

It can be demonstrated that it is maximum, since $\ddot{q}_f(k_{D1max}) = -12\frac{\varphi+1}{\varphi}k_{D1}^2 + 2\frac{2\varphi+1}{\varphi} = -4\frac{2\varphi+1}{\varphi}$ which is $\ddot{q}_f(k_{D1max}) < 0, \forall\varphi > 0$. The maximum design factor yields:

$$q_{fmax} = \frac{1}{4}\frac{1}{\varphi^2+1} \tag{4.21}$$

And k_{D2}:

$$k_{D2max} = \sqrt{\frac{1}{2\varphi(\varphi+1)}} \tag{4.22}$$

For $\varphi = 1$, $k_{D1max} = \sqrt{3}/2$ and the maximum design factor $q_f = 1/8$ for $k_{D2} = 1/2$. It can be noted that the maximum design factor is half the value of the one found for forward motion. Graphical results may be seen in Fig. 4.4. It is shown how the maximum design factors may be found in the value stated previously for $\varphi = 1$.

4.4.3 Considering forward and backward motion

In practical cases, both forward and backward motion are used. If the average force including forward and backward motion are considered:

$$\frac{F_{fb}}{\pi D^2/4} = \frac{\tau_{eq}}{2}\left[min\{\left(1-k_{D1}^2\right), \varphi k_{D2}^2\}\left(k_{D1}^2 - k_{D2}^2\right) + \left(1-k_{D1}^2\right)k_{D1}^2\right] \tag{4.23}$$

An alternative formulation yields:

$$\frac{F_f}{\pi D^2/4} = \tau_{eq}\left(1-k_{D1}^2\right)k_{D1}^2 + \begin{cases}\left(1-k_{D1}^2\right)\left(k_{D1}^2-k_{D2}^2\right) & 1-k_{D1}^2 < \varphi k_{D2}^2\\ \varphi k_{D2}^2\left(k_{D1}^2-k_{D2}^2\right) & 1-k_{D1}^2 \geq \varphi k_{D2}^2\end{cases} \tag{4.24}$$

A detailed analysis (similar to the developed for the backward motion, and excluded here) show that the maximum can be derived from (4.24), by differentiating against k_{D1} and k_{D2} and equaling to zero. The following

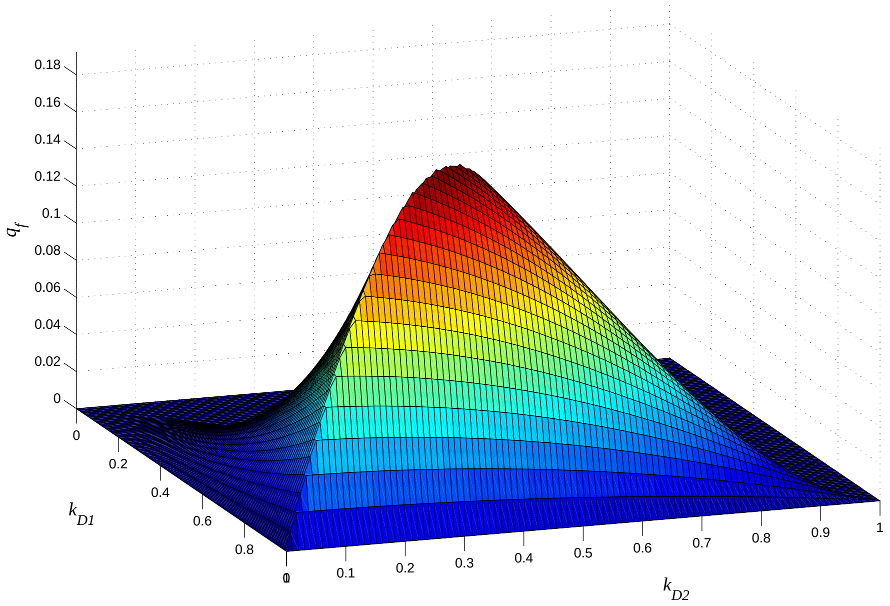

Figure 4.4: Backward force design factor, $\varphi = 1$

system of equations is obtained:

$$\begin{aligned} k_{D2} - k_{D1}\frac{1}{\sqrt{2}} &= 0 \\ \varphi k_{D2}^2 - 2k_{D1}^2 &= -1 \end{aligned} \tag{4.25}$$

Solving, the maximum is shown for:

$$k_{D1max} = \sqrt{\frac{2}{4-\varphi}} \qquad k_{D2max} = \sqrt{\frac{1}{4-\varphi}} \tag{4.26}$$

Taking $\varphi = 1$, graphical results may be seen in Fig. 4.5.

4.4.4 Stroke and Work

The stroke is given by $l - 2l_1 - l_2$. For the sake of simplicity, and without lost of generalization, l_1 can be considered equal to $l_1 = l_2 = (D - D_1)/2$, since they correspond to the wall thickness. The stroke is then $l - 3l_1 =$

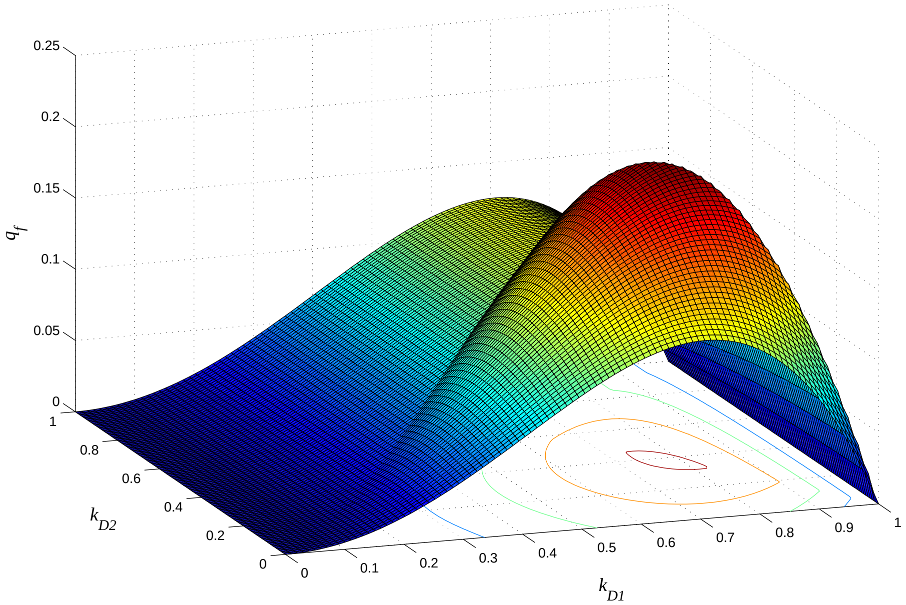

Figure 4.5: Forward - Backward averaged force design factor, $\varphi = 1$

$l - (3/2)D(1 - k_{D1}) = l\,(1 - 3\eta(1 - k_{D1}))$. It will be maximized for $\eta = 0$, which is clearly not possible, due to the fact that no force would be performed for such an aspect ratio. In this case, the force criterium would be dominant, while trying to obtain the smaller aspect ratio η for stroke maximization purposes.

Similar conclusions can be extracted analyzing the work. The maximum forward work per volume can be expressed as:

$$\frac{W_f}{\pi l D^2/4} = \tau_{eq}\left(1 - k_{D1}^2\right) k_{D1}^2\,(1 - 3\eta(1 - k_{D1})) \tag{4.27}$$

As it has been highlighted for the stroke, the work is maximized for $\eta = 0$. Concerning the dependance on k_{D1}, the maximum volumetric work can be found as the solution k_{D1} of the equation:

$$\begin{multline} -2k_{D1}^3(1-3\eta(1-k_{D1}))+2(1-k_{D1}^2)k_{D1}(1-3\eta(1-k_{D1})) \\ +3(1-k_{D1}^2)k_{D1}^2\eta=0 \quad (4.28) \end{multline}$$

whose solution is omitted because of its length. For $\eta = 0$, it yields:

$$k_{D1max} = \frac{\sqrt{2}}{2} \quad (4.29)$$

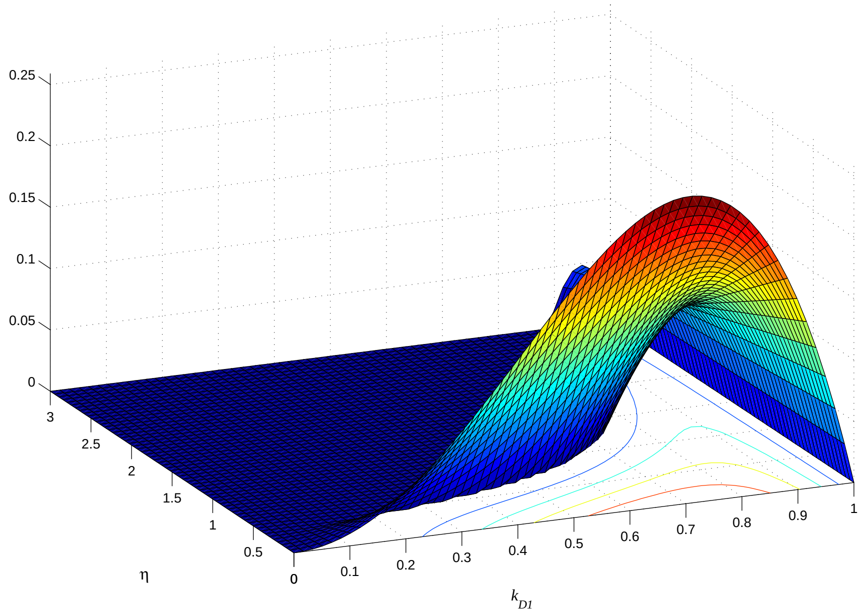

Figure 4.6: Forward work design factor

Graphical results may be seen in Fig. 4.6. It can be noted that only the forward motion has been addressed. Similar effects to those observed with the force when dealing with backward and averaged forward and backward motion appear also with the work.

4.5 Step 5. Scalability

Regarding the scalability, the static behavior of hydraulic actuators does not have the dependance on size-dependant numbers such as the Nusselt number (as happened with electromagnetic actuators [14]). Hence, as long as the static behavior is concerned the scalability criterium applies for the usual industrial range of dimensions.

4.6 Step 6. Dimensional Analysis

The force provided by these actuators can be analyzed with dimensional analysis using the Buckingham Pi Theorem [5]. The quantities involved are shown in the Table 4.1 and 4.2. The FL (force - length) system is used.

Table 4.1: Hydraulic actuator dimensional force analysis quantities

F	Force	$[F]$
x	Length	$[L]$
σ	Stress	$[FL^{-2}]$

Table 4.2: Hydraulic actuator dimensional work analysis quantities

W	Work	$[FL]$
x	Length	$[L]$
σ	Stress	$[FL^{-2}]$

The results show that the maximum force can be expressed as:

$$\frac{F}{x^2} = K\sigma \tag{4.30}$$

where it can be observed that it matches perfectly with previous analytical results. The results obtained for the work match with the previous results. The maximum work given by dimensional analysis can be expressed as:

$$\frac{F}{x^3} = K\sigma \tag{4.31}$$

4.7 Step 7. Industrial actuators

The results obtained analytically are compared with industrial actuators in the present section. Actuators from different manufacturers including *Bosch Rexroth AG*, *Parker* and *Enerpac* have been studied, taking into account their dimensions, maximum allowed pressures, strokes, etc.

The comparison between the inner-output diameter ratio of the analyzed actuators and the optimum extracted analytically from the equations show that the matching is remarkable. It can be seen in Figure 4.7. It can be noted that the real actuator data regression lies between the optimum for forward and backward motion. It is placed very close to the forward motion optimum.

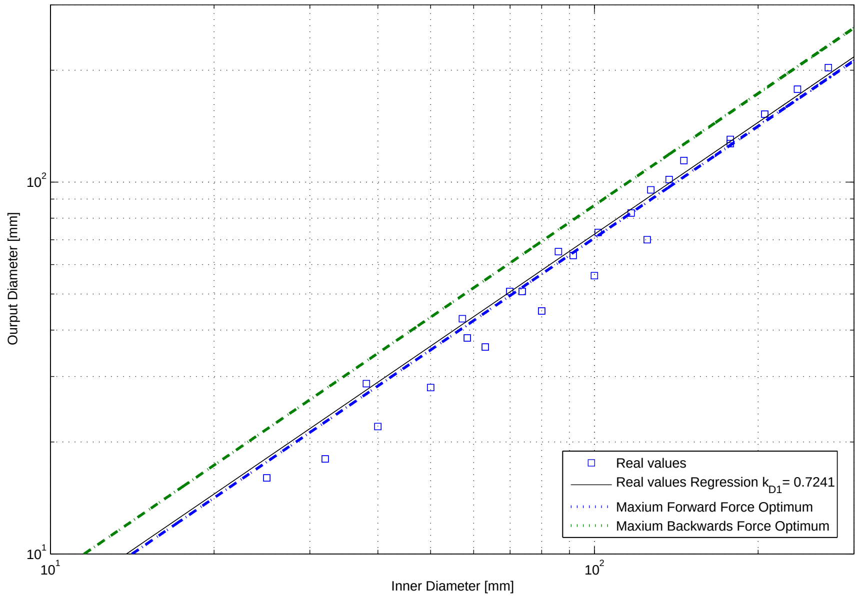

Figure 4.7: Comparison between the input to output diameter ratio existing in industrial actuators and the results of the present work.

The force-cross section relationship analyzed in Section 4.4 has proven to apply for the real actuators. In Figure 4.8 it can be noted that the real actuator performance for different actuators is below the maximum threshold.

The regression analysis of each class of actuator shows that the relationship between the force and the cross-section can be found as the considered operating pressure.

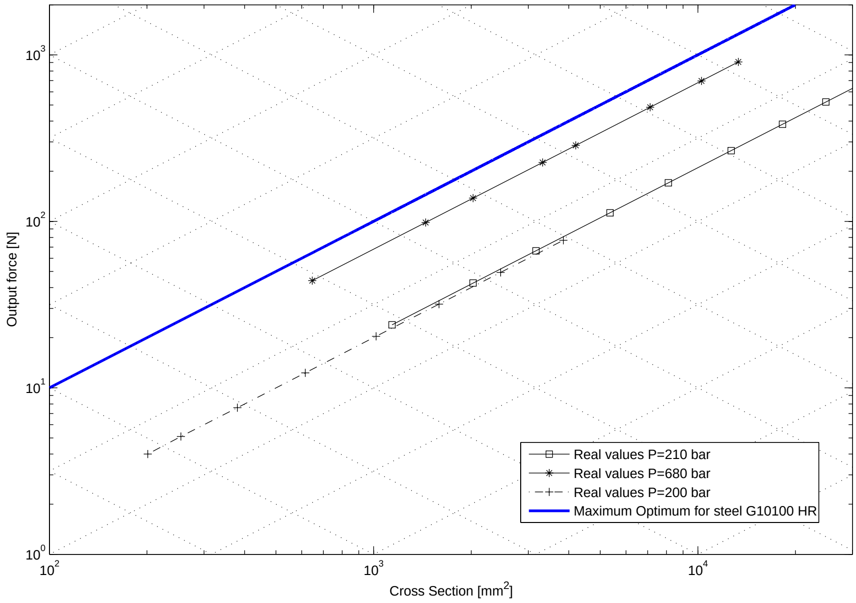

Figure 4.8: Industrial hydraulic actuator force-area performance

4.8 Conclusions

The present chapter has dealt with the optimization of linear hydraulic actuators. The procedure presented in [14] has been employed to obtain the maximum energy and force in a given volume, weight or cross-section. The scalability of the analyzed actuators has been also discussed.

The limit output quantities have been found for certain aspect ratios and geometric relationships. The results have been compared with the performance of industrial actuators and it has been noted that the industrial actuators behave as expected. Regressions linking the force and work with the cross-section and volume have been carried out, resulting in similar performances as a function of the size as the theoretically developed models.

Chapter 5

Conclusions

The present part has focused on providing the detailed analysis of different actuators using a general procedure and oriented towards improving the actuator design. It has introduced a new methodology to analyze linear electromagnetical and hydraulic actuators by modeling their maximum output mechanical quantities (force, work and stroke) as functions of the geometry and material properties and has discussed the scalability (in the sense of producing the same stress and strain distribution for different sizes). The motivation to undertake such a work stems from the need for light and volume reduced structures and systems, which are to be integrated in the design procedure as early as possible. Hence, the geometric relationships, aspect ratios and material properties that maximize the actuator output quantities with a certain limited volume or weight, along with their scalability for the integration in structures have been studied. A validation of the results has been done by performing dimensional analysis of the expressions obtained and comparing numerical results with industrial actuator data.

5.1 Contributions

The main contribution of thesis part is the methodology described in Chapter 2 along with its application to electromagnetic (Chapter 3) and hydraulic (Chapter 4) actuators. Furthermore, the contributions may be summarized as:

- Design of a methodology to deal with the modeling and optimization of industrial actuators
- Application of the methodology to linear electromagnetic actuators
- Application of the methodology to linear hydraulic actuators
- Design Optimization an scalability Analysis of the analyzed actuators.
- Validation with real actuators and with dimensional analysis of the analyzed actuators.

Part of these contributions are collected in [14] and [15].

5.2 Future work

The optimization methodology has been performed for linear hydraulic and electromagnetic actuators considering static behavior. Further research beyond the scope of this thesis is encouraged. It may be particularly interesting to investigate in the following lines:

- Application of the methodology to other classes of actuators, including some other classical actuators (pneumatic) and new smart actuators (piezoelectric, magnetostrictive, shape memory alloys, magnetorheological, etc.)
- Discussion of the validity of the methodology for non-linear motion. Application to rotative motion, substituting the force by the torque and the position by the angle.
- Expand the methodology to deal with dynamics, taking into account other quantities, such as the power or the speed.

Part II

Identification and Control of Piezoelectric Actuators

Chapter 6

Introduction

Although the so-called classical actuators (electromagnetic, hydraulic and pneumatic) are the most used in the industry, new technologies based on different physical principles are being developed. In applications where the size of the actuator has to be minimized [14], or where fast response and high resolution are needed, the classical actuators fail to respond appropriately. For this reason, non-classical technologies are becoming more relevant. Among them, the piezoelectric actuators are proving to be a reliable solution for many engineering applications, ranging from micropositioning (machine tools, optic devices or modern microscopes) to active control of structures.

The piezoelectric actuators are based on the known piezoelectric effect described in 1880 by Jacques and Pierre Curie [8]: in certain materials with crystalline non-symmetrical structure, dipoles are formed when the material is deformed, i.e. a mechanical strain produces an electrical field; reciprocally, the application of an electric field produces a strain. These actuators show a fast reaction time, a high resolution, a high energy density and an easy miniaturization. However, the piezoelectric actuators have some drawbacks: the reduced strain (< 0.2 %), the presence of non-linearities and the high voltage needed for optimal performance. In this thesis part, we focus on the nonlinear behavior of piezoelectric actuators by taking into account the presence of hysteresis. In materials, the hysteresis is referred to the memory nature of inelastic systems where the restoring force depends not only on the instantaneous deformation but also on the history of that deformation.

In this frame, the main motivation is to delve into models to represent the hysteretic behavior of piezoelectric actuators in order to apply them to the conception of controllers for such hysteretic systems. These controllers can allow a more optimum control of the devices employing piezoelectric actuators.

6.1 Modeling and validation of piezoelectric actuators

It is known that the presence of non-linearities and the high voltage needed for optimal performance are the main drawbacks of piezoelectric actuators. We focus on the nonlinear behavior of piezoelectric actuators by taking into account the presence of hysteresis.

To describe the behavior of hysteretic processes several mathematical models have been proposed [54]: the Duhem model [9] uses the property that a hysteretic system's otput changes its character when the input changes direction; the Ishlinskii hysteresis operator has been proposed as a model for plasticity-elasticity [36]; the Preisach model has been used for the modeling of electromagnetic hysteresis [43]; the Bouc-Wen model has been used to model wood joints and structural systems [11]. A survey of the mathematical models for hysteresis may be found in [40]. These models have been applied to describe the behavior of piezoelectric actuators: Prandtl-Ishlinskii in [44], Preisach in [51] and Bouc-Wen in [39]. An energy based model has been employed in [45].

The present is focused on the Bouc-Wen model. In a recent work, the hysteresis loop obtained by the Bouc-Wen model has been characterized analytically [29]. In further work [26], a new parametric nonlinear identification technique for the Bouc-Wen model based on the analytical description of [29] is proposed. This method does not use any information from the behavior of the system in the plastic region which makes it applicable for a wide class of materials including base isolation devices, magnetorheological damper, piezoelectric elements, etc. And, unlike most identification techniques for the Bouc-Wen model, this method provides the exact values of the model parameters in the absence of disturbances, and gives a guaranteed relative error between the estimated parameter and the true ones in the presence of a particular class of perturbations. The main advantages of the proposed identification methodology are (1) the simplicity of the proof that the estimated parameters are within a given tolerance with respect to their true counterparts in the presence of disturbances; (2) the fact that limit cycles can be obtained experimentally in a simple way [4]; (3) its wider range of applicability than [30]. The identification technique consists in exciting the hysteretic system with two periodic signals that have a specific shape. The parameters of the Bouc-Wen model are then obtained from the two limit cycles using a precise algorithm. The method guarantees that the estimated parameters are within a given tolerance with respect to the true parameters, and it is shown that the identification technique is robust with respect a class of disturbances of practical interest.

However, when applying the method to the modeling of certain piezoelectric actuators, an inexact matching has been noted. To improve the matching between the model and the experimental behaviour of a certain piezoelectric actuator, we propose a modification of the Bouc-Wen model. To identify such a modified model, we have developed a new identification technique based on the results obtained in [26]. The modified Bouc-Wen model is validated by means of experiments, and compared to the behavior of the non-modified Bouc-Wen model.

6.2 Control of piezoelectric actuators considering the hysteresis

The main challenge for the control design of applications with piezoelectric actuators is the presence of hysteresis. In this work, we consider the problem of micropositionning using a piezoelectric actuator. This problem has spurred much interest in the current literature. A robust controller is employed in [6] to control a piezoelectric bimorph actuator using the Bouc-Wen model. In [24] a piezoelectric actuator is modeled with neural networks and controlled with a variable structure control system. In [59], the controller uses information of the charge instead of the voltage for the control of position. This technique takes advantage of the reduced hysteresis between the displacement and the electrical charge, but presents some difficulty for the measurement of the charge.

In [31], a second-order mechanical system that includes a Bouc-Wen hysteresis is considered for control purposes. The control objective is to guarantee the global boundedness of all the closed loop signals, and the regulation of both the displacement and the velocity of the device to zero. This objective is achieved using a simple PID controller. However, the main drawback of this controller is that the equilibrium point of the closed loop system is not robust vis-à-vis perturbations which is undesirable in practice. Since the piezoelectric device is represented in this work using the Bouc-Wen model, the results of [31] are used and improved for the control of the piezoelectric element.

In order to solve such a problem, we present a new control law which is a time-varying PID that guarantees that the equilibrium point of the closed loop is robust to perturbations. Furthermore, this control law is tested in numerical simulations and experimentally using a piezoelectric actuator.

The main advantage of the proposed control law over other existing control schemes, is that it is simple to implement in an industrial context.

6.3 Objectives

The objectives can be summarized:

1. **Modeling and validation of piezoelectric actuators**: The purpose is to develop a model capable to capture the hysteretic behavior of piezoelectric actuators and to introduce an identification technique to

adjust the parameters involved. The model has to be validated by means of experiments.

2. **Control of piezoelectric actuators considering the hysteresis** Using the knowledge of the system under study provided by the model a controller has to be designed to optimize the mechatronic system.

3. **Platform construction and Experimental validation** A platform has to devised and build in order to validate experimentally all the results.

6.4 Outline

The thesis second part has been structured as follows. In **chapter 7** an introduction to the piezoelectric effect is exposed. The relevant quantities and constants are introduced and the typical linear formulation for low and high frequency are stated. Piezoelectric actuators are introduced, along with their common applications, advantages and drawbacks.

The Bouc-Wen hysteresis model is introduced in **chapter 8**. Thereafter, an identification technique to determine the parameters is proposed and its robustness against different classes of perturbations is discussed in **chapter 9**.

Chapter 10 adds an adaptation to the previous model, in order to allow it to characterize better the behavior of piezoelectric actuators. The model is validated with a real actuator and the advantages over the pervious chapter method are shown.

In **chapter 11** the models developed are employed to design a new controller. The controllers take into account not only the error but the output control effort which is tried to keep unchanged when a perturbation occurs.

In **chapter 12** the conclusions of the thesis part are summarized.

Chapter 7

Piezoelectricity

The present chapter introduces basic concepts related to piezoelectricity which will be later used. The piezoelectric effect is briefly introduced, along with the different deformation modes, the frequency effect on the piezoelectric elements behavior and some important considerations which are to be taken into account when dealing with this class of actuators: loading, nonlinearities, temperature dependance, aging and materials. The objective of this paper is to introduce such concepts in order to allow their use and development in the forthcoming chapters.

7.1 The piezoelectric effect

The word *Piezo* derives from the Greek *piezein*, which means to squeeze or press. When joined with *electricity* forming *piezoelectricity* it stands for the material property that links directly the mechanical and electrical states. The piezoelectric effect was firstly described in 1880 by Jacques and Pierre Curie [8]. In certain materials with crystalline non-symmetrical structure, dipoles are formed when the material is deformed, i.e. a mechanical strain produces an electrical field, reciprocally the application of an electric field produces a strain.

Although the piezoelectric behavior observed is highly non-linear, simplified equations are presented in [25; 52; 53] introducing the direct and inverse piezoelectric effect:

$$\begin{aligned} D &= dT + \varepsilon^T E \\ S &= s^E T + dE \end{aligned} \tag{7.1}$$

where d is defined as the piezoelectric coefficients matrix, ε^T is the piezoelectric permittivity under conditions of constant stress, s^E is the compliance of the material under constant electric field, D is the electric displacement, E is the electric field, T the mechanical stress and S the mechanical strain. Alternatively, it can be written as:

$$\begin{aligned} E &= -gT + \beta^T D \\ S &= s^D T + gD \end{aligned} \tag{7.2}$$

where g is a piezoelectric constant, s^D is the compliance of the material under constant electric displacement and β^T is the impermittivity component [25] under conditions of constant stress. A third alternative expression yields:

$$\begin{aligned} E &= -hS + \beta^S D \\ T &= c^D S + hD \end{aligned} \tag{7.3}$$

where h is a piezoelectric constant, β^S is the impermittivity component under conditions of constant strain and c^D is the elastic stiffness constant under conditions of constant electric displacement. The relationships between the different constants can be expressed as:

$$\begin{aligned} g &= \beta^T d \\ d &= \varepsilon^T g \\ h &= g c^D \end{aligned} \tag{7.4}$$

Note the indices employed to show relevant information about the constants or quantities. The example s_{12}^E indicates that the compliance s is for a stress in the axis 2 and strain in axis 1 considered under conditions of constant electrical field E. Such superior indexes are of crucial importance and it is important to use the appropriated ones. They are linked as:

$$\begin{aligned} s^D &= s^E - dg \\ \beta^T &= \beta^S - gh \end{aligned} \tag{7.5}$$

Depending on the application geometry and the mechanical and electrical constraints (7.1), (7.2) or (7.3) will be employed.

All the expressions can be written in matrix form. (7.1) may be expressed as:

$$\begin{pmatrix} S_1 \\ S_2 \\ S_3 \\ S_4 \\ S_5 \\ S_6 \end{pmatrix} = \begin{bmatrix} s_{11}^E & s_{12}^E & s_{13}^E & s_{14}^E & s_{15}^E & s_{16}^E \\ s_{21}^E & s_{22}^E & s_{23}^E & s_{24}^E & s_{25}^E & s_{26}^E \\ s_{31}^E & s_{32}^E & s_{33}^E & s_{34}^E & s_{35}^E & s_{36}^E \\ s_{41}^E & s_{42}^E & s_{43}^E & s_{44}^E & s_{45}^E & s_{46}^E \\ s_{51}^E & s_{52}^E & s_{53}^E & s_{54}^E & s_{55}^E & s_{56}^E \\ s_{61}^E & s_{62}^E & s_{63}^E & s_{64}^E & s_{65}^E & s_{66}^E \end{bmatrix} \times \begin{pmatrix} T_1 \\ T_2 \\ T_3 \\ T_4 \\ T_5 \\ T_6 \end{pmatrix} + \begin{bmatrix} d_{11} & d_{21} & d_{31} \\ d_{12} & d_{22} & d_{32} \\ d_{13} & d_{23} & d_{33} \\ d_{14} & d_{24} & d_{34} \\ d_{15} & d_{25} & d_{35} \\ d_{16} & d_{26} & d_{36} \end{bmatrix} \times \begin{pmatrix} E_1 \\ E_2 \\ E_3 \end{pmatrix} \tag{7.6}$$

Using the tetragonal crystal system explained in [25] (7.6) may be written as:

$$\begin{pmatrix} S_1 \\ S_2 \\ S_3 \\ S_4 \\ S_5 \\ S_6 \end{pmatrix} = \begin{bmatrix} s_{11}^E & s_{12}^E & s_{13}^E & 0 & 0 & 0 \\ s_{12}^E & s_{11}^E & s_{13}^E & 0 & 0 & 0 \\ s_{13}^E & s_{13}^E & s_{33}^E & 0 & 0 & 0 \\ 0 & 0 & 0 & s_{44}^E & 0 & 0 \\ 0 & 0 & 0 & 0 & s_{44}^E & 0 \\ 0 & 0 & 0 & 0 & 0 & s_{66}^E \end{bmatrix} \times \begin{pmatrix} T_1 \\ T_2 \\ T_3 \\ T_4 \\ T_5 \\ T_6 \end{pmatrix} + \begin{bmatrix} 0 & 0 & d_{31} \\ 0 & 0 & d_{31} \\ 0 & 0 & d_{33} \\ 0 & d_{15} & 0 \\ d_{15} & 0 & 0 \\ 0 & 0 & 0 \end{bmatrix} \times \begin{pmatrix} E_1 \\ E_2 \\ E_3 \end{pmatrix} \tag{7.7}$$

Analogously:

$$\begin{pmatrix} D_1 \\ D_2 \\ D_3 \end{pmatrix} = \begin{bmatrix} 0 & 0 & 0 & 0 & d_{15} & 0 \\ 0 & 0 & 0 & d_{15} & 0 & 0 \\ d_{31} & d_{31} & d_{33} & 0 & 0 & 0 \end{bmatrix} \times \begin{pmatrix} T_1 \\ T_2 \\ T_3 \\ T_4 \\ T_5 \\ T_6 \end{pmatrix} + \begin{bmatrix} \varepsilon_{11} & 0 & 0 \\ 0 & \varepsilon_{11} & 0 \\ 0 & 0 & \varepsilon_{33} \end{bmatrix} \times \begin{pmatrix} E_1 \\ E_2 \\ E_3 \end{pmatrix} \tag{7.8}$$

It can be expressed in a single expression as:

$$\begin{pmatrix} S_1 \\ S_2 \\ S_3 \\ S_4 \\ S_5 \\ S_6 \\ \hdashline D_1 \\ D_2 \\ D_3 \end{pmatrix} = \left[\begin{array}{cccccc:ccc} s_{11}^E & s_{12}^E & s_{13}^E & 0 & 0 & 0 & 0 & 0 & d_{31} \\ s_{12}^E & s_{11}^E & s_{13}^E & 0 & 0 & 0 & 0 & 0 & d_{31} \\ s_{13}^E & s_{13}^E & s_{33}^E & 0 & 0 & 0 & 0 & 0 & d_{33} \\ 0 & 0 & 0 & s_{44}^E & 0 & 0 & 0 & d_{15} & 0 \\ 0 & 0 & 0 & 0 & s_{44}^E & 0 & d_{15} & 0 & 0 \\ 0 & 0 & 0 & 0 & 0 & s_{66}^E & 0 & 0 & 0 \\ \hdashline 0 & 0 & 0 & 0 & d_{15} & 0 & \varepsilon_{11} & 0 & 0 \\ 0 & 0 & 0 & d_{15} & 0 & 0 & 0 & \varepsilon_{11} & 0 \\ d_{31} & d_{31} & d_{33} & 0 & 0 & 0 & 0 & 0 & \varepsilon_{33} \end{array}\right] \times \begin{pmatrix} T_1 \\ T_2 \\ T_3 \\ T_4 \\ T_5 \\ T_6 \\ \hdashline E_1 \\ E_2 \\ E_3 \end{pmatrix} \tag{7.9}$$

The so-called electromechanical coupling factor k is specially significative in the characterization of a piezoelectric element, it is defined in [52] as:

$$k^2 = \frac{d^2}{s^E \varepsilon^T} \tag{7.10}$$

and it shows the relationship between the stored mechanical energy and the input electrical energy when working as an actuator, and between the stored electrical energy and the input mechanical energy when working as a sensor.

7.1.1 A brief history

Some references [19; 35] deal with the history of piezoelectric technology. The most important events are reported here briefly.

In 1880, the brothers Pierre Curie and Jacques Curie predicted and demonstrated piezoelectricity using tinfoil, glue, wire, magnets, and a jeweler saw [8; 58]. They showed that crystals of tourmaline, quartz, topaz, cane sugar, and Rochelle salt (sodium potassium tartrate tetrahydrate) generate electrical polarization from mechanical stress. Quartz and Rochelle salt exhibited the most piezoelectricity. The term *piezoelectricity* was first suggested by W. Hankel in 1881. Converse piezoelectricity was mathematically deduced from fundamental thermodynamic principles by Lippmann in 1881. The Curies immediately confirmed the existence of the *converse effect* and obtained quantitative proof of the complete reversibility of deformations in piezoelectric crystals.

In 1910 Voigt published *Lehrbuch der Kristallphysik* [55], and it became a standard reference work detailing the complex electromechanical relationships in piezoelectric crystals. During World War I the piezoelectric ultrasonic transducer was developed by Langevin. At the same time piezoelectric materials began to be used as microphones, accelerometers, underwater transducers, etc. However, the limited material performance inhibited commercialization.

During World War II $BaTiO_3$ was discovered as a high dielectric constant material in USA, UK, USSR, and Japan, independently. Gray discovered a poling process, which made ceramic materials act as a single crystal possessing both ferroelectric and piezoelectric properties. In 1952, PZT was reported as ferroelectric solid-solution system, and the phase diagram was established by Shirane, et al. PZT was reported as useful piezoelectric transducer material by B. Jaffe et al. in 1954. Piezoelectric ceramics applications became commercialized, including phonograph pick-ups, microphones, underwater transducers (sonar), ignition systems, discrete actuators, etc. The 1960s-1980s decades were important for the discovery and research of transparent electro-optic $(Pb, La)(Zr, Ti)O_3$ $PLZT$ ceramics and by the development of $Pb(Mg_{1/3}Nb_{2/3})O_3$ PMN and other relaxor ferroelectric ceramics and devices. Also there was the first development of multi-layer stack actuators.

From 1980 to now piezoelectric actuators has been used for smart structures, distributed actuator systems, prototype smart beam, active airfoil, etc.. There has been a development of flexible actuators based on piezoelectric fibers embedded in polymer matrix (active fiber composites), with applications for active vibration reduction and noise control system. The use of piezoelectric actuators in micro and nano positioning devices requiring high precision such as modern microscopes is one of the actual applications and challenges of the piezoelectric technology.

7.1.2 Deformation modes.

The deformation directions are shown in Fig. 7.1. It is important to note that all the parameters used in (7.1) have to be considered in the different deformation directions.

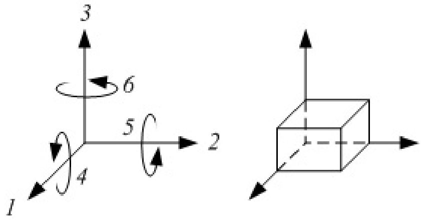

Figure 7.1: Axes and deformation directions.

Depending on the electrical field application and the deformation of interest, piezoelectric actuators can be employed using different modes:

- Longitudinal mode d_{33}. See Fig. 7.2(a). Expression (7.6) turns into:

$$S_3 = \sum_{i=1}^{6} \left(s_{3i}^{E} T_i \right) + d_{33} E_3 \tag{7.11}$$

- Transverse mode d_{31}. See Fig. 7.2(b). Expression (7.6) turns into:

$$S_1 = \sum_{i=1}^{6} \left(s_{1i}^{E} T_i \right) + d_{31} E_3 \tag{7.12}$$

- Shear mode d_{15}. See Fig. 7.2(c). Expression (7.6) turns into:

$$S_5 = \sum_{i=1}^{6} \left(s_{5i}^{E} T_i \right) + d_{15} E_1 \tag{7.13}$$

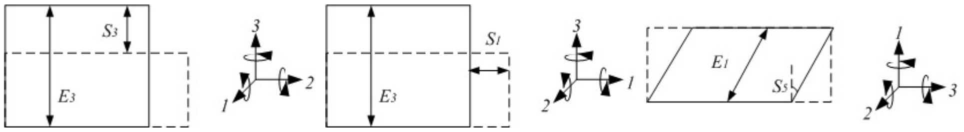

(a) Longitudinal mode. (b) Transverse mode. (c) Shear mode.

Figure 7.2: Different deformation modes.

7.2 Piezoelectric actuator simplified model

7.2.1 Low frequency

A piezoelectric element can be modeled from (7.1) as the association in parallel of a capacitor and a charge source, since the charge can be obtained from the electric displacement D, and the voltage can be derived from the electrical field E, assuming that it is uniformly distributed in a length l ($V = E/l$). Expression (7.1) can be written as:

$$\begin{aligned} \frac{Q_e}{A} &= d\frac{F}{A} + \varepsilon^T \frac{V}{z} \\ \frac{x}{l_0} &= s^E \frac{F}{A} + d\frac{V}{z} \end{aligned} \tag{7.14}$$

where Q_e is the electrical charge, A is the cross-section in the movement direction, F is the force, V is the applied voltage, l_0 is the initial length in the movement axis and z is the thickness in electrical field direction. The first equation of (7.14), (known as the sensor expression) can be written as:

$$Q_e = dF + \varepsilon^T \frac{A}{z} V = dF + CV \tag{7.15}$$

where $C = \varepsilon^T A/z$ is the equivalent capacitance.

The second equation of (7.14), (known as the actuation expression) can be written as:

$$x = s^E l_0 \frac{F}{A} + Vd\frac{l_0}{z} = k^{-1}F + d\frac{l_0}{z}V \tag{7.16}$$

where $k = A/s^E l_0$ is the equivalent stiffness constant. Note that in the longitudinal mode, the electrical field is applied in the motion's direction and thus:

$$x = k^{-1}F + dV \tag{7.17}$$

7.2.2 High frequency

These approximations of (7.15),(7.16) and (7.17) apply for low frequencies but when the dynamic behavior for higher frequencies (close to the mechanical resonance frequency) is concerned, the model from [56] characterized in Fig. 7.3 has to be used. It includes the equivalent capacitor and a RLC branch in parallel where R_1 includes the mechanical losses, L_1 is the equivalent inductance of the mechanical circuit and C_1 the capacitance of the mechanical circuit. Each branch has a mechanical resonance at $f_i = 1/2\pi\sqrt{L_iC_i}$. A current (or charge) source can be added if the system is mechanically loaded. More branches can be added corresponding to the resonance frequencies of the mechanical system.

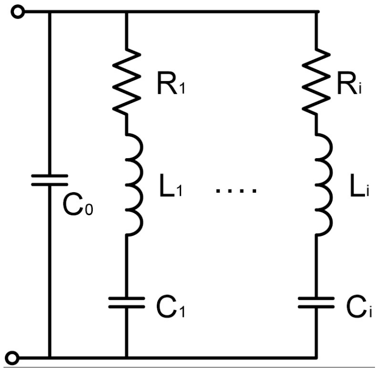

Figure 7.3: Equivalent circuit of a piezoelectric element excited at high frequency.

The impedance behavior against the frequency considering only one resonance frequency is plotted in Fig. 7.4. It can be noted that the frequencies between them show an inductive behavior while the others below resonance and above antiresonance show capacitive behavior. The resonance and antiresonance frequencies can be found for values close to the series and parallel

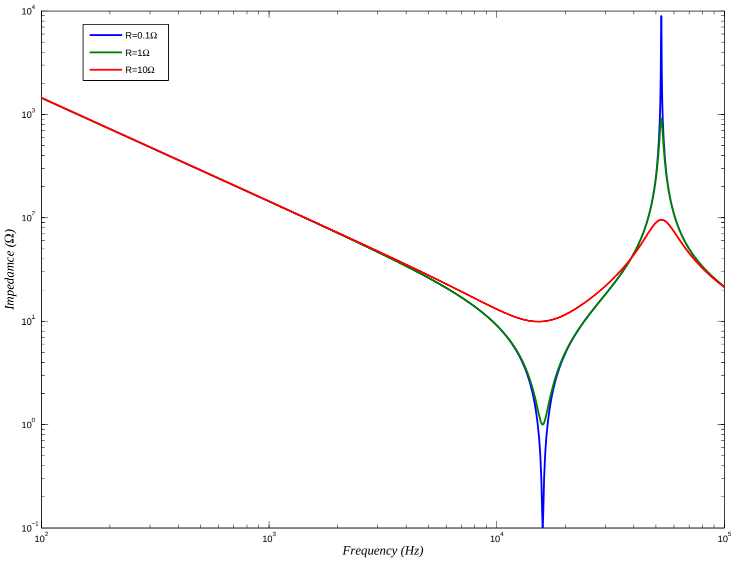

(a) Impendance value

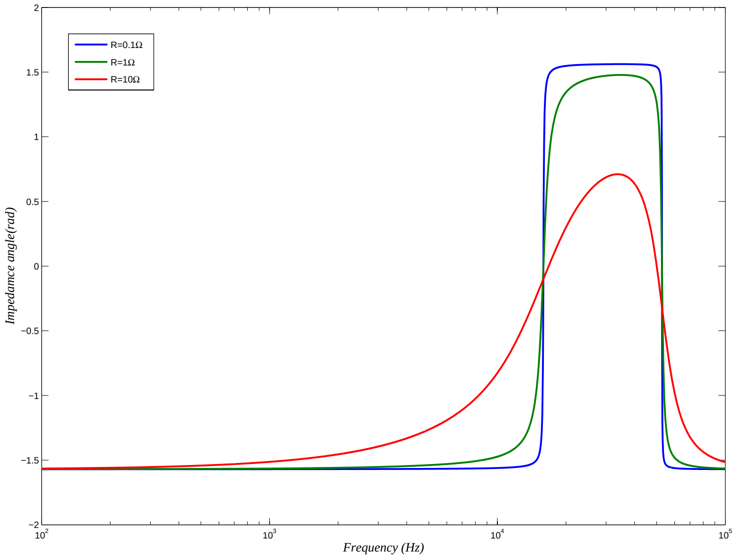

(b) Impedance angle

Figure 7.4: Impedance of a piezoelectric element with different R values and $C_0 = 0.1\ \mu$F, $C_1 = 1\ \mu$F and $L_1 = 0.1$ mH.

resonant frequency as:

$$
\begin{aligned}
f_r &= \frac{1}{2\pi}\sqrt{\frac{1}{L_1C_1}} \\
f_a &= \frac{1}{2\pi}\sqrt{\frac{C_0+C_1}{L_1C_0C_1}}
\end{aligned}
\tag{7.18}
$$

7.2.3 Load

The relationship between force and displacement can be extracted from expression (7.16). Manufacturers usually provide the force with no displacement and the free displacement. Defining F_0 as the force with no displacement (clamped actuator) and x_0 the free displacement with no force:

$$
\begin{aligned}
x_0 &= dV\frac{l_0}{z} \\
F_0 &= dV\frac{A}{zs^E}
\end{aligned}
\tag{7.19}
$$

Hence expression (7.16) can be rewritten as:

$$
F = \frac{F_0}{x_0}\left(x_0 - x\right) \tag{7.20}
$$

where both F_0 and x_0 depend linearly on the applied voltage. Note that the previously defined stiffness constant k, can be expressed as F_0/x_0 and does not depend on the voltage but on the material stiffness. An alternative expression of (7.20) is:

$$
F = k\left(x_0 - x\right) = F_0 - kx \tag{7.21}
$$

7.2.3.1 Example

An example can be shown with a sample actuator working in the transversal mode. The parameters are:

$$l_0 = 50 \cdot 10^{-3} m$$
$$z_0 = 0.2 \cdot 10^{-3} m$$
$$A = 6 \cdot 10^{-6} m^2$$
$$s_{31}^E = 15 \cdot 10^{-12} m^2/N$$
$$d_{31} = -250 \cdot 10^{-12} m/V$$

Then:

$$k = \frac{A}{s_E \cdot l_0} = \frac{6 \cdot 10^{-6}}{15 \cdot 10^{-12} \cdot 50 \cdot 10^{-3}} = 8 \cdot 10^6 N/m$$

For $V = 400\ V$:

$$x_0 = d \cdot V \cdot \tfrac{l_0}{z_0} = -250 \cdot 10^{-12} \cdot 400 \cdot \tfrac{50 \cdot 10^{-3}}{0.2 \cdot 10^{-3}} = 25 \cdot 10^{-6} m$$
$$F_0 = x_0 \cdot k = 200N$$

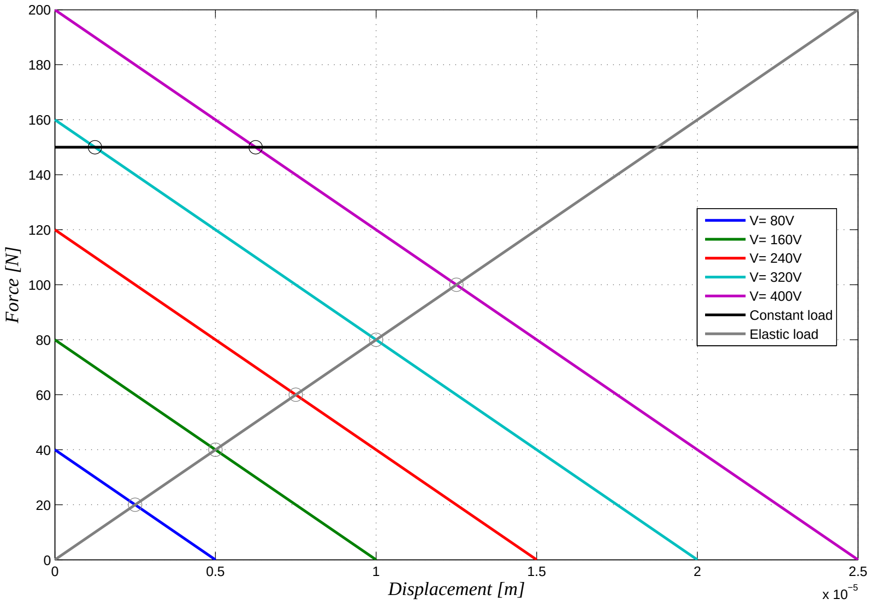

Figure 7.5: Displacement - Force curves

In Figure 7.5 the load - displacement characteristic for different voltages can be seen. Also the load - displacement characteristic for different voltages under a constant load and linear load (for example a spring or a attached structure) are shown.

7.3 Considerations

7.3.1 Non-linearities

It is known that the presence of non-linearities is one of the main drawbacks of piezoelectric actuators. The most important non-linearities involved in piezoelectric materials are hysteresis and creep. The hysteresis is referred to the memory nature of inelastic systems where the restoring force depends not only on the instantaneous deformation but also on the history of that deformation. The hysteresis (Fig. 7.6) is produced by the retarded reorientation of dipole domains, which initially maintain their direction in the field direction upon reducing its strength. The creep refers to the time variation of the strain. When the field is changed and hold constant at a certain level, more and more dipoles orient themselves in the applied direction and thus, a increment in the strain is produced. It is important to note that creep is significative in static conditions while hysteresis has to be always taken into account.

To describe the behavior of hysteretic processes several mathematical models have been proposed [54]: the Duhem model [9] uses the property that a hysteretic system's otput changes its character when the input changes direction; the Ishlinskii hysteresis operator has been proposed as a model for plasticity-elasticity [36]; the Preisach model has been used for the modeling of electromagnetic hysteresis [43]; the Bouc-Wen model has been used to model wood joints and structural systems [11]. A survey of the mathematical models for hysteresis may be found in [40]. These models have been applied to describe the behavior of piezoelectric actuators: Prandtl-Ishlinskii in [44], Preisach in [51] and Bouc-Wen in [39]. An energy based model has been employed in [45].

In the present thesis part we consider the modeling of a piezoelectric actuator using the Bouc-Wen model for smooth hysteresis [57]. This model has received an increasing interest due to its ability to capture in an analytical form a range of shapes of hysteretic cycles which match the behavior of a wide class of hysteretical systems [46]. In particular, it has been used to

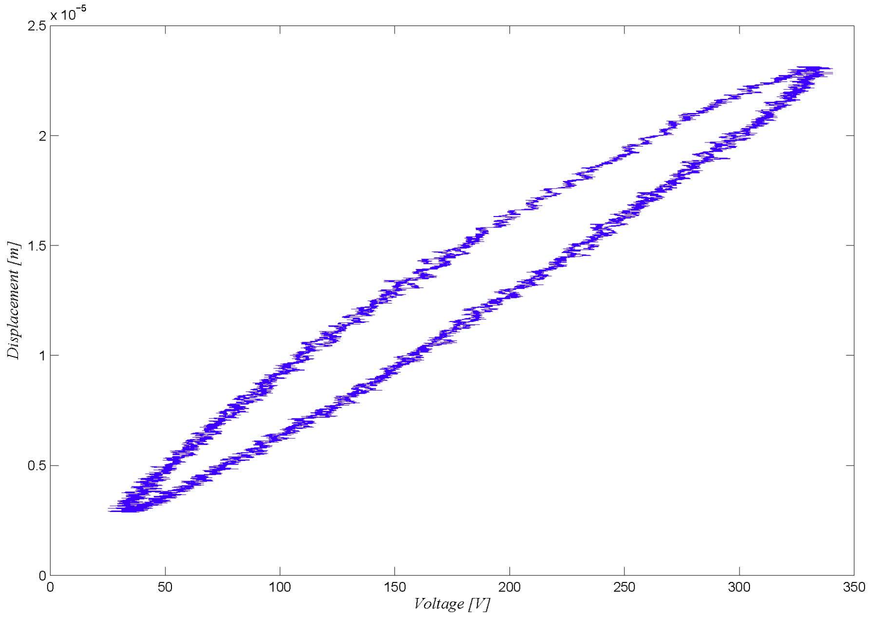

Figure 7.6: Example of a displacement - voltage hysteresis curve

model piezoelectric elements [39], magnetorheological dampers [7; 47] and wood joints [11]. The models, derived from experiments, have been used either to predict the behavior of the physical hysteretic element [47] or for control purposes as in [6; 28; 31].

7.3.2 Temperature dependance

The temperature is an important quantity to be considered when dealing with piezoelectric actuators. The Curie temperature T_C is a threshold value. Above T_C the piezoelectric materials lose their piezoelectric properties. The Curie temperature ranges from 160 $°C$ to 350 $°C$ depending on the materials. It is important to remark that depolarization begins to occur below T_C and thus the temperature should be limited to half of the Curie temperature.

7.3.3 Aging

As it is explained in [34] the mechanical and electrical loading of piezoelectric materials can lead to micro-cracking. Such phenomenon can change the material properties or destroy the actuator or sensor. Some improvements introduced in manufacturing processes and material engineering are allowing certain actuators to achieve up to 10^9 high-level cycles without suffering substantial damage.

7.3.4 Piezoelectric materials

The piezoelectric materials are divided in single-crystal materials, piezoceramics, piezopolymers, piezocomposites and piezofilms. Comprehensive information about them may be found in [52]. The most significant paramaters employed to describe piezoelectric actuators can be found in Table 7.1. The most relevant properties of some piezoelectric materials are shown in Table 7.2.

Table 7.1: Piezoelectric material relevant parameters.

Quantity	Description	Units
d_{ij}	Piezoelectric Strain Constant	C/N
g_{ij}	Piezoelectric Voltage Constant	Vm/N
k_t	Thickness-extensional coupling factor	
k_p	Planar coupling factor	
ε	Relative permittivity	
Q_m	Mechanical Quality Factor	
T_C	Curie Temperature	$^{\circ}C$

7.4 Applications

The employment of piezoelectric actuators has been increased in the last decades. The main advantages [42] shown by the piezoelectric actuators are:

- **High Resolution**: A piezoelectric actuator can perform very small and precise position changes to the subnanometer range.

Table 7.2: Piezoelectric material properties [52].

Parameter	Quartz	$BaTiO_3$	PZT 4	PST 5H	(Pb, Sm) TiO_3	PVDF TrFE
d_{33} pC/N	2.3	190	289	593	65	33
g_{33} $10^{-3}Vm/N$	57.8	12.6	26.1	19.7	42	380
k_t	0.09	0.38	0.51	0.50	0.50	0.30
k_p		0.33	0.58	0.65	0.03	
ε	5	1700	1300	3400	175	6
Q_m	$> 10^5$		500	65	900	3-10
T_C °C		120	328	193	355	

- **Easy miniaturization**: The fact that they are solid state actuators allows to miniaturize them and allow their application to micro and nano-scale applications. This advantage is very significative in comparison with their electromagnetic counterparts [14].

- **Work in different directions**: It is not necessarily an advantage but it certainly allows a wide range of applications, not only longitudinal traction.

- **Large Force Generation**: Piezoelectric actuators generate large forces. It leads to high energy and power densities.

- **Very Rapid Response**: Piezoelectric actuators offer very fast time response. It enables to be used in applications requiring very high frequencies.

- **Absence of Magnetic Fields**: Piezoelectric actuators are especially indicated for applications where magnetic fields are not allowed.

- **Low Power Consumption**: The piezoelectric effect converts directly electrical energy to motion. The electrical energy is consumed only during the motion. The static losses can be considered very low in comparison with other kinds of actuators.

- **Compatible with vacuum and clean rooms**: Piezoelectric actuators use ceramic elements which do not need lubrication and exhibit no wear or abrasion. This makes them clean-room compatible and ideally suited for ultra-high-vacuum applications.

The main drawbacks include:

- **Reduced displacement**: The piezoelectric actuators range is small in comparison with other actuators. The maximum typical deformation is approximately < 0.2 %.
- **High voltage operation**: To obtain a certain displacement usually requires high voltage operation, with all the drawbacks involved.
- **High non-linearity**: Piezoelectric actuators show an elevated non-linearity due to hysteresis and creep. The present thesis concentrates in this drawback. Forthcoming chapters will introduce techniques to model accurately the hysteresis present in piezoelectric actuators and present controllers able to minimize the hysteresis effect for control purposes.

The mentioned advantages make piezoelectric actuators appropriated for a wide range of applications. They are summarized in Table 7.3.

Table 7.3: Main applications of piezoelectric devices.

Linear Actuator	Bending Actuator	Generator Sensor	Transformer Sensor/Actuator
Fuel injection	Drug dispensers	Accelerometers	LCD backlighting
Printers	Valves	Force sensor	Ion generators
Microscopes	Pumps	Pressure sensor	Power Supplies
Micropositioning	Micropositioning	Knock sensors	
Nanopositioning	Nanopositioning	Gyroscopes	
Tunable lasers	Textile machines	Medical	
Ultrasonic motors	Optics	Gas ignition	
Micro pumps	Micro pumps	Sonars	
Ultrasound scanners	Vibration control	Medical scanners	
Droplet dispensing	Droplet dispensing	Blood flow meters	
Hard disc drives	Wire bonding	Distance sensors	
Process control	Tunable lasers		
Mechatronics	Mechatronics		
Optics	Optics		
Vibration control	Vibration control		
Ultrasound welding	Telecommunication		
Ultrasound cleaning	Moving opt. fibres		
Stretching opt. fibers			

Chapter 8

The Bouc-Wen model

8.1 Introduction

Hysteresis is encountered in a wide variety of processes in which the input-output dynamic relations between variables involve memory effects. Examples are found in biology, optics, electronics, ferroelectricity, magnetism, mechanics, structures, among other areas.

In the present thesis part we consider the modeling of a piezoelectric actuator using the Bouc-Wen model for smooth hysteresis [57]. Consider a physical system with a hysteretic component that can be represented by a map $x(t) \mapsto \Phi_s(x)(t)$, which is referred to as the "true" hysteresis. The so-called Bouc-Wen model represents the true hysteresis in the form [57]

$$\begin{aligned} \Phi_{BW}(x,t) &= \alpha k x(t) + (1-\alpha) D k z(t), && (8.1) \\ \dot{z} &= D^{-1}\left(A\dot{x} - \beta|\dot{x}|\,|z|^{n-1}z - \gamma\dot{x}|z|^{n}\right), && (8.2) \end{aligned}$$

where $\dot{z}$ denotes the time derivative, $n \geq 1$, $D > 0$, $k > 0$ and $0 < \alpha < 1$. This model was originally developed in the context of mechanical systems in which x is a displacement and Φ_s is a restoring force. It represents the hysteretic force $\Phi_s(x)(t)$ as the superposition of an elastic component $\alpha k x$ and a purely hysteretic component $(1-\alpha)kDz$, in which $D > 0$ is the yield constant displacement and $\alpha \in (0,1)$ is the post to pre-yielding stiffness ratio. The hysteretic part involves a nondimensional auxiliary variable z

which is the solution of the nonlinear first order differential equation (8.2). In this equation, A, β and γ are nondimensional parameters which control the shape and the size of the hysteresis loop, while n is a scalar that governs the smoothness of the transition from elastic to plastic response. The Bouc-Wen model has received an increasing interest due to its ability to capture in an analytical form a range of shapes of hysteretic cycles which match the behavior of a wide class of hysteretical systems [46]. In particular, it has been used to model piezoelectric elements [39], magnetorheological dampers [7; 47] and wood joints [11]. The models, derived from experiments, have been used either to predict the behavior of the physical hysteretic element [47] or for control purposes as in [6; 28; 31].

8.2 The normalized Bouc-Wen model

8.2.1 Classification of the Bouc-Wen models

The nonlinear hysteretic behavior may be conceptualized [32] as a map $x(t) \mapsto \Phi_s(x)(t)$, where $x(t)$ represents the time history of an input variable and $\Phi_s(x)(t)$ describes the time history of the hysteretic output variable. Two fundamental properties are shared by many physical hysteretic systems arising from structural, mechanical and electromechanical engineering:

Property 1: For any bounded input $x(t)$, the output of the true hysteresis $\Phi_s(x)(t)$ is bounded. This bounded input-bounded output (BIBO) property stems from the fact that, in practice, many (electro)mechanical and structural systems are stable in open loop.

Property 2: The physical systems that include hysteretic components dissipate energy.

To represent adequately the true hysteresis $\Phi_s(x)(t)$, the Bouc-Wen model $\Phi_{BW}(x)(t)$ needs to keep both properties, that is to be BIBO and dissipative. Define the sets:

$$\Omega_{\alpha,k,D,A,\beta,\gamma,n} = \{z(0) \in \mathbb{R} \text{ such that } \Phi_{BW} \text{ is BIBO} \\ \text{with fixed values of the parameters } \alpha, k, D, A, \beta, \gamma, n\} \tag{8.3}$$

$$\Omega_{A,\beta,\gamma,n} = \{z(0) \in \mathbb{R} \text{ such that } z(t) \text{ is bounded for any } C^1 \text{ bounded} \\ \text{input signal } x(t)\text{with fixed values of the parameters } A, \beta, \gamma, n\} \tag{8.4}$$

$$\Omega^{\star}_{A,\beta,\gamma,n} = \{z(0) \in \mathbb{R} \text{ such that } z(t) \text{ is bounded for any } C^1 \text{ input} \\ \text{signal } x(t) \text{ with fixed values of the parameters } A, \beta, \gamma, n\} \tag{8.5}$$

Then, we have the following result which characterizes the two classes of Bouc-Wen models that are BIBO and asymptotically dissipative [29].

Theorem 1 *Define the constants:*

$$z_0 \triangleq \sqrt[n]{\frac{A}{\beta+\gamma}} \text{ and } z_1 \triangleq \sqrt[n]{\frac{A}{\gamma-\beta}}. \tag{8.6}$$

Then, Table 8.1 holds.

Table 8.1: Classification of the BIBO, passive and thermodynamically consistent Bouc-Wen models

CASE		$\Omega_{A,\beta,\gamma,n}$	Upper bound on $\lvert z(t)\rvert$	CLASS
$A > 0$	$\beta+\gamma > 0$ and $\beta-\gamma \geq 0$	$\mathbb{R}$	$\max\left(\lvert z(0)\rvert, z_0\right)$	I

Furthermore, we have

$$\Omega_{\alpha,k,D,A,\beta,\gamma,n} = \Omega^{\star}_{A,\beta,\gamma,n} = \Omega_{A,\beta,\gamma,n} \tag{8.7}$$

A by-product of Theorem 1 is the existence and uniqueness of the solution $z(t)$ over $t \in [0, +\infty)$. Equality (8.7) means that the boundedness of the signal $z(t)$ depends only on the parameters A, γ, β and n, and it is independent of the boundedness of the input signal $x(t)$. This fact is particularly important for system control theory: when $x(t)$ is a closed loop signal, we cannot assume a priori that it is bounded. The fact that $\Omega^{\star}_{A,\beta,\gamma,n} = \Omega_{A,\beta,\gamma,n}$ shows that for every input signal $x(t)$ (under the only assumption that it is C^1), the output $z(t)$ is always bounded if the set Ω is non-empty, and if $z(0) \in \Omega$.

In parallel work [10], the study of the thermodynamic admissibility of the Bouc-Wen model within the context of the endochronic theory led to the following result: the conditions $A > 0$ and $-\beta \leqslant \gamma \leqslant \beta$ are necessary and sufficient for the thermodynamic admissibility of the Bouc-Wen model. This means that the class I Bouc-Wen model is consistent with the laws of thermodynamics.

8.2.2 The normalized Bouc-Wen model

Consider two Bouc-Wen models (8.1)-(8.2) whose parameters are such that $n_2 = n_1 = n$, $A_2 = A_1$, $\beta_2 = \nu^n \beta_1$, $\gamma_2 = \nu^n \gamma_1$, $D_2 = \nu D_1$, $\alpha_2 = \alpha_1$, $k_2 = k_1$ where ν is a positive constant, and with an initial condition $z_2(0) = z_1(0) = 0$. Then both models belong to the same class, and for any input signal $x(t)$ they deliver exactly the same output $\Phi_{BW}(t)$. This means that the input-output behavior of a Bouc-Wen model is not described by a unique set of parameters $\{\alpha, k, D, A, \beta, \gamma, n\}$ and, for this reason, identification procedures that use input-output data cannot determine the parameters of the Bouc-Wen model. To cope with this problem, users of the Bouc-Wen model often fix some parameters to arbitrary values as in reference [41] where the coefficient $(1-\alpha)Dk$ of $z(t)$ in equation (8.1) has been set to one and the parameter D has also been set to one. Other authors compare the shape of the limit cycle instead of comparing the identified parameters with their true values as in reference [47]. This fact makes it very difficult to compare results of different identification methods by comparing the identified parameters. Thus it is necessary to elaborate some equivalent "normalized" model whose parameters define in a unique way the input-output behavior of the model allowing a parametric-based comparison of identification methods for this hysteretic model. To this end, define $w(t) = \frac{z(t)}{z_0}$ so that the model (8.1)-(8.2) can be written as:

$$\begin{aligned} \Phi_{BW}(x)(t) &= \kappa_x x(t) + \kappa_w w(t), && (8.8) \\ \dot{w}(t) &= \rho \left(\dot{x} - \sigma |\dot{x}(t)| \, |w(t)|^{n-1} w(t) + (\sigma - 1) \dot{x}(t) |w(t)|^n \right) && (8.9) \end{aligned}$$

where

$$\rho = \frac{A}{D z_0} > 0, \;\; \sigma = \frac{\beta}{\beta + \gamma} \geq 0, \;\; \kappa_x = \alpha k > 0, \;\; \kappa_w = (1 - \alpha) D k z_0 > 0. \tag{8.10}$$

We call equations (8.8)-(8.9) the normalized form of the Bouc-Wen model. Note that if the initial condition $w(0)$ is such that $|w(0)| \leq 1$ then, by Theorem 1, $|w(t)| \leq 1$ for all $t \geq 0$. This means that the variable $z(t)$ has been scaled to unity. It can be checked that the normalized form of the Bouc-Wen model defines a bijective relationship between the input-output behavior of the model and its parameters. It also has the advantage of having only five parameters to identify instead of the seven parameters for the standard form. Note that the normalized form of the Bouc-Wen model is exactly equivalent to its standard form. Indeed, for any input $x(t)$, both forms deliver exactly the same output $\Phi_{BW}(t)$ taking into account that we have $w(0) = \frac{z(0)}{z_0}$. The classification of the normalized Bouc-Wen models is given in Table 8.2. It can be seen that a single parameter σ is needed for this classification.

Table 8.2: Classification of the BIBO, passive and thermodynamically stable normalized Bouc-Wen models

CASE	$\Omega_{\sigma,n}$	Upper bound on $\lvert w(t)\rvert$	CLASS
$\sigma \geq \frac{1}{2}$	$\mathbb{R}$	$\max\left(\lvert w(0)\rvert, 1\right)$	I

With these notations we obtain from equation (8.9):

$$\begin{aligned}
\text{For } w(t) \geq 0, \dot{x}(t) \geq 0 \quad \dot{w}(t) &= \rho\left(1 - w(t)^n\right)\dot{x}(t) && (8.11)\\
\text{For } w(t) \leq 0, \dot{x}(t) \geq 0 \quad \dot{w}(t) &= \rho\left(1 + (2\sigma - 1)\left(-w(t)\right)^n\right)\dot{x}(t) && (8.12)\\
\text{For } w(t) \geq 0, \dot{x}(t) \leq 0 \quad \dot{w}(t) &= \rho\left(1 + (2\sigma - 1)w(t)^n\right)\dot{x}(t) && (8.13)\\
\text{For } w(t) \leq 0, \dot{x}(t) \leq 0 \quad \dot{w}(t) &= \rho\left(1 - \left(-w(t)\right)^n\right)\dot{x}(t) && (8.14)
\end{aligned}$$

Chapter 9

Analysis and parameter identification of the Bouc-Wen model

It is known that the presence of non-linearities and the high voltage needed for optimal performance are the main drawbacks of piezoelectric actuators. As it is explained in Section 7.3.1, we focus on the nonlinear behavior of piezoelectric actuators by taking into account the presence of hysteresis.

The normalized version of the model introduced in chapter 8 relates the output restoring force $\Phi_{BW}(x)(t)$ to the input displacement $x(t)$ in the following way:

$$\begin{aligned} \Phi_{BW}(x)(t) &= \kappa_x x(t) + \kappa_w w(t), && (9.1) \\ \dot{w}(t) &= \rho \left(\dot{x}(t) - \sigma |\dot{x}(t)| \, |w(t)|^{n-1} w(t) + \right. \\ & \quad \left. + (\sigma - 1) \dot{x}(t) |w(t)|^n \right) && (9.2) \end{aligned}$$

where $\kappa_x > 0$, $\kappa_w > 0$, $\rho > 0$, $\sigma > \frac{1}{2}$ and $n \geq 1$ are the model parameters that shape the hysteresis loop. The range of the parameter σ corresponds to the Class I Bouc-Wen model which is stable, asymptotically dissipative and thermodynamically consistent [29]. This chapter deals with the problem of identifying the model parameters in the presence of disturbances. The signals that are accessible to measurements are the input $x(t)$ and the output

$\Phi_{BW}(x)(t)$. The state $w(t)$ is not accessible to measurements. As can be seen from equations (9.1)-(9.2), the difficulty of the identification problem lies (1) in the nonlinear form of the model, especially in relation with the estimation of the parameter n which forms part of the "structure" of the model and (2) in the fact that the state $w(t)$ is not accessible to measurements. A survey of the parametric and non parametric methods that have been used in the literature for the identification of the Bouc-Wen model may be found in [38]. The main theoretical deficiency of these methods is that they rely mainly on numerical simulations and do not offer, to a large extent, a rigorous mathematical proof of the convergence of the estimated parameters to their true counterparts.

In this chapter, we propose a new parametric nonlinear identification technique for the Bouc-Wen model based on the analytical description of [29]. This method does not use any information from the behavior of the system in the plastic region which makes it applicable for a wide class of materials including base isolation devices, magnetorheological damper, piezoelectric elements, etc. And, unlike most identification techniques for the Bouc-Wen model, this method provides the exact values of the model parameters in the absence of disturbances, and gives a guaranteed relative error between the estimated parameter and the true ones in the presence of a particular class of perturbations. The main advantages of the proposed identification methodology are (1) the simplicity of the proof that the estimated parameters are within a given tolerance with respect to their true counterparts in the presence of disturbances (2) the fact that limit cycles can be obtained experimentally in a simple way [4] (3) its wider range of applicability than [30]. The identification technique consists in exciting the hysteretic system with two periodic signals that have a specific shape. The parameters of the Bouc-Wen model are then obtained from the two limit cycles using a precise algorithm. This method guarantees that the estimated parameters are within a given tolerance with respect to the true parameters, and it is shown that the identification technique is robust with respect a class of disturbances of practical interest.

9.1 Parameter identification for the Bouc-Wen model

9.1.1 Class of inputs

In this chapter we consider that the input signal $x(t)$ is T-wave periodic [29]. This means that it is continuous on the time interval $[0, +\infty)$ and periodic of period $T > 0$. Furthermore there exists a scalar $0 < T^+ < T$ such that the signal x is C^1 on both intervals $(0, T^+)$ and (T^+, T) with $\dot{x}(\tau) = \dfrac{dx(\tau)}{d\tau} > 0$ for $\tau \in (0, T^+)$ and $\dot{x}(\tau) < 0$ for $\tau \in (T^+, T)$ (see Figure 9.1). We denote $X_{\min} = x(0)$ and $X_{\max} = x(T^+) > X_{\min}$ the minimal and maximal values of the input signal, respectively. We assume that $\max\left(|X_{\max}|, |X_{\min}|\right) \leq \dfrac{\kappa_w}{\kappa_x}$ so that the Bouc-Wen model is consistent with the hysteretic property [30].

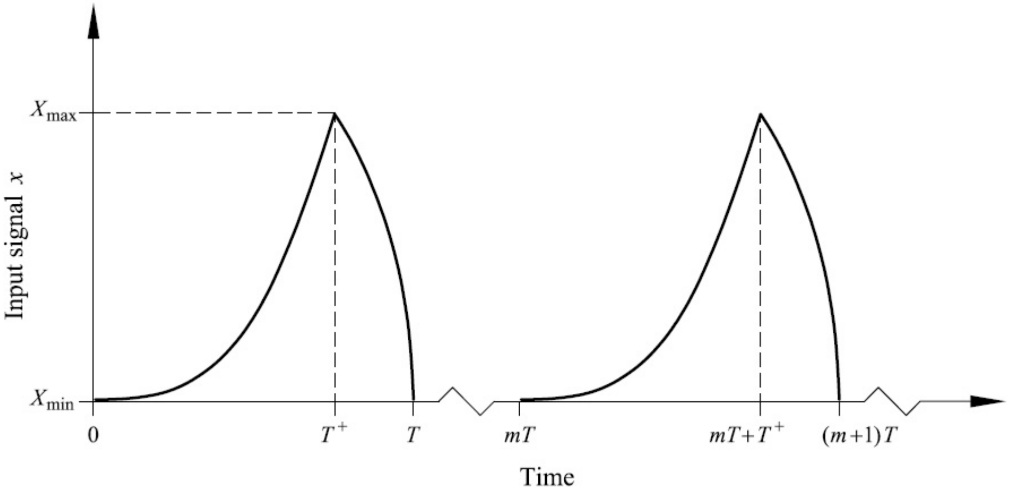

Figure 9.1: Example of a T-wave periodic signal.

9.1.2 Analytic description of the forced limit cycle for the Bouc-Wen model

Define the following functions:

$$\begin{aligned}
\varphi^{-}_{\sigma,n}(w) &= \int_0^w \frac{1}{1+\sigma|u|^{n-1}u+(\sigma-1)|u|^n}du && (9.3)\\
\varphi^{+}_{\sigma,n}(w) &= \int_0^w \frac{1}{1-\sigma|u|^{n-1}u+(\sigma-1)|u|^n}du && (9.4)\\
\varphi_{\sigma,n}(w) &= \varphi^{+}_{\sigma,n}(w)+\varphi^{-}_{\sigma,n}(w) && (9.5)
\end{aligned}$$

for any scalar $w \in (-1,1)$. In this section and in the rest of the chapter we denote $w(t)$ the solution of the differential equation (9.2) while the notation w without an argument is used for a given scalar. It has been shown in [29] that the functions $\varphi^{-}_{\sigma,n}(\cdot)$, $\varphi^{+}_{\sigma,n}(\cdot)$ and $\varphi_{\sigma,n}(\cdot)$ are strictly increasing on the interval $(-1,1)$ so that they are bijective. Their inverses are denoted $\psi^{-}_{\sigma,n}(\cdot)$, $\psi^{+}_{\sigma,n}(\cdot)$ and $\psi_{\sigma,n}(\cdot)$, respectively. These functions have been studied extensively in [29]. Note that for $w \geq 0$ we have

$$\begin{aligned}
\varphi^{-}_{\sigma,n}(w) &= \int_0^w \frac{1}{1+(2\sigma-1)u^n}du && (9.6)\\
\varphi^{+}_{\sigma,n}(w) &= \int_0^w \frac{1}{1-u^n}du && (9.7)
\end{aligned}$$

and for $w \leq 0$ we have

$$\begin{aligned}
\varphi^{-}_{\sigma,n}(w) &= \int_0^w \frac{1}{1-(-u)^n}du && (9.8)\\
\varphi^{+}_{\sigma,n}(w) &= \int_0^w \frac{1}{1+(2\sigma-1)(-u)^n}du && (9.9)
\end{aligned}$$

The limit cycle for the Bouc-Wen model is described by the following [29]:

Theorem 2 *Let $x(t)$ be a T-wave periodic input signal. Define the functions ω_m and ϕ_m for any positive integer m as follows*

$$\begin{aligned}
\omega_m(\tau) &= w(mT+\tau) \quad \textit{for} \quad \tau \in [0,T] && (9.10)\\
\phi_m(\tau) &= \kappa_x x(\tau)+\kappa_w \omega_m(\tau) \quad \textit{for} \quad \tau \in [0,T] && (9.11)
\end{aligned}$$

where $w(\cdot)$ is the solution of equation (9.2) with initial condition $w(0)$. Then the sequence of functions $\{\phi_m\}_{m\geq 1}$ (resp. $\{\omega_m\}_{m\geq 1}$) converges uniformly on the interval $[0,T]$ to a continuous function $\bar{\Phi}_{BW}$ (resp. $\bar{w}$) defined as

$$\begin{aligned}
\bar{\Phi}_{BW}(\tau) &= \kappa_x x(\tau) + \kappa_w \bar{w}(\tau) \quad \textit{for} \quad \tau \in [0,T] && (9.12)\\
\bar{w}(\tau) &= \psi^{+}_{\sigma,n}\left(\varphi^{+}_{\sigma,n}\left[-\psi_{\sigma,n}\left(\rho\left(X_{\max}-X_{\min}\right)\right)\right]+\right.\\
&\quad \left.+\rho\left(x(\tau)-X_{\min}\right)\right) \;\textit{for}\; \tau \in [0,T^{+}]\\
& && (9.13)\\
\bar{w}(\tau) &= -\psi^{+}_{\sigma,n}\left(\varphi^{+}_{\sigma,n}\left[-\psi_{\sigma,n}\left(\rho\left(X_{\max}-X_{\min}\right)\right)\right]\right.\\
&\quad \left.-\rho\left(x(\tau)-X_{\max}\right)\right) \;\textit{for}\; \tau \in [T^{+},T]\\
& && (9.14)
\end{aligned}$$

Furthermore we have for all $\tau \in [0,T]$

$$\begin{aligned}
-1 &< -\psi_{\sigma,n}\left(\rho\left(X_{\max}-X_{\min}\right)\right) \leq \bar{w}(\tau)\\
&\leq \psi_{\sigma,n}\left(\rho\left(X_{\max}-X_{\min}\right)\right) < 1 && (9.15)
\end{aligned}$$

the lower and upper bounds of $\bar{w}(\tau)$ being attained at $\tau = 0$ and $\tau = T^{+}$ respectively.

9.1.3 Identification methodology

In general, the nonlinear state variable w is not accessible to measurement. However, in many cases of practical importance, the hysteretic limit cycle can be obtained experimentally [41]. The hysteretic system under study is assumed to be described by the normalized Bouc-Wen model (9.1)-(9.2), with unknown parameters κ_x, κ_w, ρ, σ and n. The loading part of the limit cycle (that corresponds to an increasing input $x(t)$) can be obtained from Theorem 2 as:

$$\begin{aligned}
\bar{\Phi}_{BW}(x) &= \kappa_x x + \kappa_w \bar{w}(x) && (9.16)\\
\bar{w}(x) &= \psi^{+}_{\sigma,n}\left(\varphi^{+}_{\sigma,n}\left[-\psi_{\sigma,n}\left(\rho\left(X_{\max}-X_{\min}\right)\right)\right]+\right.\\
&\quad \left.+\rho\left(x-X_{\min}\right)\right) && (9.17)
\end{aligned}$$

Note that, by an abuse of notation, we use the same symbol $\bar{w}(\cdot)$ to describe the function $\bar{w}(\tau)$ and $\bar{w}(x)$. This is justified as the function $x(\tau)$ is bijective in the loading part of the limit cycle. The proposed identification method assumes the knowledge of the relation $\bar{\Phi}_{BW}(x)$, that is the knowledge of the limit cycle. In equations (9.16)-(9.17), the parameters κ_x, κ_w, σ, ρ, n are unknown. From equation (9.17) it follows that:

$$\frac{d\bar{w}(x)}{dx} = \rho\left(1-\bar{w}(x)^n\right) \quad \text{for} \quad \bar{w}(x) \geq 0 \tag{9.18}$$

$$\frac{d\bar{w}(x)}{dx} = \rho\left(1+(2\sigma-1)\left(-\bar{w}(x)\right)^n\right) \text{ for } \bar{w}(x) \leq 0 \tag{9.19}$$

Consider two wave T-periodic signals $x(t)$ and $x_1(t)$ such that $x_1(t) = x(t)+q$ for a given constant q. Denoting the corresponding hysteretic outputs $\bar{w}(x)$ and $\bar{w}_1(x_1)$ respectively, we get from equation (9.13) that $\bar{w}_1(x_1) = \bar{w}(x)$ for all $x \in [X_{\min}, X_{\max}]$. It follows from equation (9.12) that $\bar{\Phi}_{BW,1}(x_1) = \bar{\Phi}_{BW}(x) + \kappa_x q$ which gives the value of κ_x as:

$$\kappa_x = \frac{\bar{\Phi}_{BW,1}(x+q) - \bar{\Phi}_{BW}(x)}{q} \tag{9.20}$$

for any value of $x \in [X_{\min}, X_{\max}]$. Since κ_x has been determined, the quantity $\kappa_w \bar{w}(x)$ can be computed from equation (9.12) as

$$\kappa_w \bar{w}(x) = \bar{\Phi}_{BW}(x) - \kappa_x x \triangleq \theta(x). \tag{9.21}$$

Then, equation (9.18) can be written as:

$$\frac{d\theta(x)}{dx} = a - b\,\theta(x)^n \quad \text{for} \quad \theta(x) \geq 0 \tag{9.22}$$

where $a = \rho\kappa_w$ and $b = \rho\kappa_w^{-n+1}$. The coefficient a can be computed from equation (9.22) as:

$$a = \left(\frac{d\theta(x)}{dx}\right)_{x=x_*} \tag{9.23}$$

where x_* is such that $\theta(x_*) = 0$. The existence and uniqueness of this zero follows from Theorem 2. Take two design input values $x_{*2} > x_{*1} > x_*$, then the parameter n and the quantity b can be determined as:

$$\begin{aligned} n &= \frac{\log\left(\dfrac{\left(\frac{d\theta(x)}{dx}\right)_{x=x_{*2}} - a}{\left(\frac{d\theta(x)}{dx}\right)_{x=x_{*1}} - a}\right)}{\log\left(\dfrac{\theta(x_{*2})}{\theta(x_{*1})}\right)} && (9.24) \\ b &= \frac{a - \left(\dfrac{d\theta(x)}{dx}\right)_{x=x_{*2}}}{\theta(x_{*2})^n} && (9.25) \end{aligned}$$

and the parameters κ_w and ρ are computed as follows:

$$\begin{aligned} \kappa_w &= \sqrt[n]{\frac{a}{b}} && (9.26) \\ \rho &= \frac{a}{\kappa_w} && (9.27) \end{aligned}$$

Then, the function $\bar{w}(x)$ can be computed from equation (9.12) as:

$$\bar{w}(x) = \frac{\theta(x)}{\kappa_w} \tag{9.28}$$

The remaining parameter σ is determined as:

$$\sigma = \frac{1}{2}\left(\frac{\dfrac{\left(\dfrac{d\bar{w}(x)}{dx}\right)_{x=x_{*3}}}{\rho} - 1}{\left(-\bar{w}(x_{*3})\right)^n} + 1\right) \tag{9.29}$$

where x_{*3} is a design parameter such that $\bar{w}(x_{*3}) < 0$ or equivalently $x_{*3} < x_*$.

The identification methodology is summarized in the following steps.

- Step 1. Excite the Bouc-Wen model with a wave periodic signal $x(t)$. After a transient, the output $\Phi_{BW}(t)$ will have a steady state $\bar{\Phi}_{BW}(t)$ as proved in Theorem 2. Since both the input and the output are accessible to measurements, the relation $\left(x, \bar{\Phi}_{BW}(x)\right)$ is known.

- Step 2. Choose a nonzero constant q and excite the Bouc-Wen model with the input $x_1(t) = x(t) + q$. After a transient, the output $\Phi_{BW,1}(t)$ will have a steady state $\bar{\Phi}_{BW,1}(t)$ as proved in Theorem 2. Since both the input and the output are accessible to measurements, the relation $\left(x_1, \bar{\Phi}_{BW,1}(x_1)\right)$ is known.
- Step 3. Compute the coefficient κ_x using equation (9.20).
- Step 4. Compute the function $\theta(x)$ using equation (9.21).
- Step 5. Determine the zero of the function $\theta(x)$, that is the quantity x_* such that $\theta(x_*) = 0$.
- Step 6. Compute the parameter a using equation (9.23).
- Step 7. Choose two design constants x_{*1} and x_{*2} such that $x_{*2} > x_{*1} > x_*$. Then, compute the parameters n and b using equations (9.24) and (9.25) respectively.
- Step 8. Compute the parameters κ_w and ρ using equations (9.26) and (9.27) respectively.
- Step 9. Compute the function $\bar{w}(x)$ using equation (9.28).
- Step 10. Choose a design constant x_{*3} such that $x_{*3} < x_*$. Then, compute the parameter σ using equation (9.29).

As can be seen, this identification method provides the exact values of the Bouc-Wen model parameters in the absence of disturbances. The next section analyzes the robustness of the method with respect to a class of disturbances of practical interest.

9.1.4 Robustness of the identification method

In practice, the T-periodic input signal $x(t)$ excites the hysteretic system via a (generally) linear actuator. Assume that the frequency of the input signal lies within the bandwidth of this actuator and that the latter has a unity gain at the zero frequency. Then the output of the actuator can be written in the steady state as $x_d(t) = x(t) + d(t)$ where the term $d(t)$ is due to the fact that the higher harmonics of the signal $x(t)$ are filtered by the actuator. Since the input $x(t)$ is T-periodic, so are the signal $x_d(t)$ and the perturbation $d(t)$.

On the other hand, T-periodic measurement disturbances result from the fact that a sensor has always a limited bandwidth. Thus, the high frequency components of the hysteretic output are filtered so that in the steady state, the measured output and the real output differ by a T-periodic function $v(t)$.

Note that if the input disturbance $d(t)$ is not T-periodic (for example a random noise), then the limit cycle does not occur. Also if the measurement disturbance $v(t)$ is not T-periodic, then even if the input disturbance $d(t)$ is T-periodic, the limit cycle is not observed. However, even though the necessity for the disturbances to be T-periodic constitutes the main theoretical limitation of our identification method, experimental evidence shows that in many cases of practical relevance, limit cycles are indeed observed (see for example [4, Figure 6.12 upper]). This means that for these cases, the most relevant disturbances are indeed T-periodic.

We consider in this section that the input signal is corrupted by an additive disturbance which is constant or periodic with the same period as the input signal. More precisely we consider that an unknown disturbance $d(t)$ is added to the input signal $x(t)$ resulting in a corrupted input signal $x_d(t) = x(t) + d(t)$. If the signal $x_d(t)$ is accessible to measurement, then the analysis of the identification method is much easier as this is equivalent to identifying the Bouc-Wen model parameters with a known input and in the absence of disturbances. This case is included in the more general case of a signal $x(t)$ that is accessible to measurement and a signal $x_d(t)$ that is not accessible to measurement. This corresponds to an unknown signal $d(t)$ which is often the case in practice.

We also consider that the hysteretic output $\bar{\Phi}_{BW}(t)$ is corrupted by an additive measurement disturbance $v(t)$. We choose the signal $x(t)$ so that $0 < X_{\max} = -X_{\min}$, and we make the following assumption on the disturbances $d(t)$ and $v(t)$ that are denoted by the generic notation $\xi(t)$:

Assumption 1 *The unknown disturbance signal* $\xi(t)$ *is constant or periodic of period* T*, is continuous for all* $t \geq 0$ *and* C^1 *on the interval* $(0, T^+) \bigcup (T^+, T)$*. Moreover, there exists a constant* $0 \leq \mu < \frac{1}{2}$ *such that:*

$$
\begin{aligned}
|\xi(\tau)| &\leq \mu X_{\max} \quad \textit{for} \quad \tau \in [0, T] && (9.30)\\
\left|\dot{\xi}(\tau)\right| &\leq \mu \left|\dot{x}(\tau)\right| \quad \textit{for} \quad \tau \in (0, T^+) \bigcup (T^+, T) && (9.31)
\end{aligned}
$$

Clearly the disturbances d and v belong to the class of constant or small slowly time-varying periodic disturbances. These disturbances will be said μ-small. Note that, in practice, the perturbations may have high frequency components that do not verify Assumption 1. In this case, a low pass filter may be designed to eliminate these components so that the resulting perturbations comply with Assumption 1.

Under Assumption 1, the corrupted input signal $x_d(t)$ belongs to the class of inputs of Section 9.1.1 so that limit cycles occur and are described by Theorem 2. Denoting $X_{d,\max}$ and $X_{d,\min}$ the maximal and minimal values of x_d we get $X_{d,\max} = X_{\max} + d(T^+)$ and $X_{d,\min} = -X_{\max} + d(0)$ and the limit cycle is described by the equations

$$
\begin{aligned}
&\bar{\Phi}_{BW}(\tau) = \kappa_x X_{\max} \bar{x}(\tau) + \kappa_x X_{\max} \bar{d}(\tau) + \kappa_w \bar{w}(\tau) + \\
&\qquad\qquad + X_{\max} \bar{v}(\tau) \text{ for } \tau \in [0, T] && (9.32)\\
&\bar{w}(\tau) = \psi^{+}_{\sigma,n}\left(\varphi^{+}_{\sigma,n}\left[-\psi_{\sigma,n}\left(\delta\left(1+\varepsilon_d\right)\right)\right] + \right.\\
&\left. + \frac{\delta}{2}\left[\bar{x}(\tau) + 1 + \bar{d}(\tau) - \bar{d}(0)\right]\right) \text{ for } \tau \in [0, T^+] && (9.33)\\
&\bar{w}(\tau) = -\psi^{+}_{\sigma,n}\left(\varphi^{+}_{\sigma,n}\left[-\psi_{\sigma,n}\left(\delta\left(1+\varepsilon_d\right)\right)\right] \right.\\
&\left. - \frac{\delta}{2}\left[\bar{x}(\tau) - 1 + \bar{d}(\tau) - \bar{d}(T^+)\right]\right) \text{ for } \tau \in [T^+, T] && (9.34)
\end{aligned}
$$

where we take $-1 \leq \bar{x}(\tau) = \dfrac{x(\tau)}{X_{\max}} \leq 1$ as the normalized input function which is accessible to measurement and $\delta = 2\rho X_{\max}$. The quantities $\bar{d}(\tau) = \dfrac{d(\tau)}{X_{\max}}$ and $\bar{v}(\tau) = \dfrac{v(\tau)}{X_{\max}}$ correspond to the (unknown) normalized disturbances and

$\varepsilon_d = \dfrac{\bar{d}(T^+) - \bar{d}(0)}{2}$. For any normalized Bouc-Wen model parameter p we denote p° the identified one. Let $0 < \epsilon < \frac{1}{2}$ be the maximal tolerance allowed for the identified parameters. This means that for each parameter p of the Bouc-Wen model and its corresponding identified value p°, we should have $\left|\dfrac{p - p^\circ}{p}\right| \leq \epsilon$.

In this section, we consider only the loading part of the hysteretic limit cycle, that is we consider that in equations (9.32)-(9.34) we have $\tau \in [0, T^+]$. Since the input signal $\bar{x}(\tau)$ is, by assumption, such that $\dot{\bar{x}}(\tau) > 0$ for all $\tau \in (0, T^+)$, the function $\bar{x}(\tau)$ is a bijection from the time interval $[0, T^+]$ to $[-1, 1]$. Thus it is possible to define its inverse function from the interval $[-1, 1]$ to the time interval $[0, T^+]$. By an abuse of notation, we denote this inverse function τ.

With these notations, we rewrite equations (9.32)-(9.33) as:

$$\begin{aligned}
\bar{\Phi}_{BW}(\bar{x}) &= \kappa_x X_{\max}\bar{x} + \kappa_x X_{\max}\bar{d}\left(\tau(\bar{x})\right) + \kappa_w \bar{w}(\bar{x}) + \\
&\quad + X_{\max}\bar{v}\left(\tau(\bar{x})\right) && (9.35) \\
\bar{w}(\bar{x}) &= \psi^+_{\sigma,n}\left(\varphi^+_{\sigma,n}\left[-\psi_{\sigma,n}\left(\delta\left(1 + \varepsilon_d\right)\right)\right] + \right. \\
&\quad \left. + \frac{\delta}{2}\left[\bar{x} + 1 + \bar{d}\left(\tau(\bar{x})\right) - \bar{d}(0)\right]\right) && (9.36)
\end{aligned}$$

where we did not use the letter l for loading to simplify the notations. We also use the notations $\bar{q} = \dfrac{q}{X_{\max}}$ and $\bar{x}_{*i} = \dfrac{x_{*i}}{X_{\max}}$, $i = 1, 2, 3$. We now state the main result of this section.

Theorem 3 *Let $\bar{x}_{*1}$, $\bar{x}_{*2}$ and $\bar{x}_{*3}$ be design parameters and let $\epsilon > 0$ be the desired precision on the estimated parameters. There exists a real number $\mu^*\left(\kappa_x, \kappa_w, \rho, n, \sigma, \bar{q}, \bar{x}_{*1}, \bar{x}_{*2}, \bar{x}_{*3}, \epsilon\right) > 0$ called robustness margin such that: for any μ-small disturbances d and v verifying $0 \leq \mu \leq \mu^*$, and for any parameter $p \in \{\kappa_x, \kappa_w, \rho, n, \sigma\}$, the corresponding identified parameter p° using the methodology of Section 9.1.3 is such that $\left|\dfrac{p - p^\circ}{p}\right| \leq \epsilon$.*

The proof of Theorem 3 is given in the appendix A.

Robustness is a central issue in identification methods. It is not enough that the method gives the correct parameters in the absence of perturbations, it is also desirable that a “small size” of disturbances leads to a “small discrepancy” between the identified parameters and the true one. Theorem 3 says that, given an $\epsilon > 0$, for all μ-small disturbances such that $0 \leq \mu \leq \mu^*$, the relative error between the identified parameters p° and the true parameters p does not exceed ϵ. If the quantity μ^* were zero, this would have implied that, even for arbitrarily small disturbances, the identification method may lead to a large discrepancy between the identified parameters and the true ones. Theorem 3 guarantees that the robustness margin $\mu^* > 0$ so that all μ-small disturbances with $\mu \in [0, \mu^*]$ lead to a relative error in the parameters no more than ϵ.

9.2 Numerical simulation example

In this section we consider the Bouc-Wen model given by the unknown parameters $\kappa_x = 2$, $\kappa_w = 2$, $\rho = 1$, $\sigma = 3$, $n = 1.5$. The objective is to use the technique presented in the previous sections to identify its parameters. As seen in Section 9.1.3, the identification technique has 10 steps.

Step 1. The first step of the identification procedure is the choice of the T-periodic input signals. Due to Assumption 1 we have $\left|\dot{\xi}(\tau)\right| \leq \mu \left|\dot{x}(\tau)\right|$. This implies that derivative $\dot{\xi}(\tau)$ of the disturbance $\xi(\tau)$ needs to be zero whenever the derivative of the input signal $x(\tau)$ is zero. Thus, a sine wave input signal candidate would impose that $\dot{\xi}(\tau)$ should be very small around the time instants $0 + mT$ and $\frac{T}{2} + mT$ (m is any positive integer) which is unlikely to happen in practice. For this reason, a good choice of an input signal is a triangular one so that the derivative $\dot{\xi}(\tau)$ needs only to be small with respect to the slope of the input signal which is constant (in absolute value). The next design parameter to be chosen is the frequency of the input signal. Since the Bouc-Wen model is rate independent, its input-output behavior is independent of the frequency of the input signal. We thus take $T = 1$ and $T^+ = \frac{T}{2}$. We also choose $X_{\max} = -X_{\min} = 0.2$.

Step 2. In this step, one has to choose a value $q \neq 0$ to obtain a second input signal $x_1(t) = x(t) + q$. The signals $x(t)$ and $x_1(t)$ are given in Figure

9.2 with $q = 0.1$.

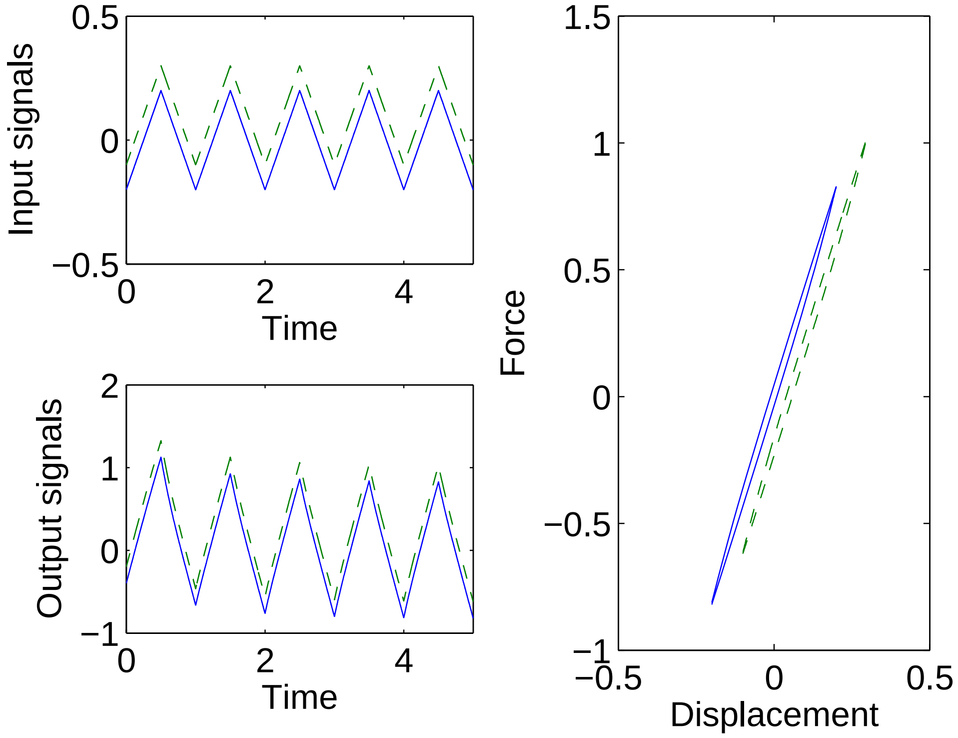

Figure 9.2: Upper left. Solid: input signal $x(t)$, dashed: input signal $x_1(t)$. Lower left. Solid: output $\Phi_{BW}(x)(t)$, dashed: output $\Phi_{BW,1}(x)(t)$. Right. Limit cycles $(x, \bar{\Phi}_{BW})$ (solid) and $(x_1, \bar{\Phi}_{BW,1})$ (dashed) that have been obtained for the time interval $[4T, 5T]$

In practice, the input and output data are in the form of a finite number of samples $x(kh)$, $\bar{\Phi}(kh)$ where h is the sampling period, $k = 0, 1, \cdots, m$ and m the number of samples. These samples have to be taken once the output of the system is in steady-state. Note that, since the identification technique uses only the loading part of the limit cycle, we can choose the time instant $kh = 0$ such that $x(k = 0)$ corresponds to the lowest value of x and the time instant mh so that $x(k = m)$ corresponds to the largest value of x. This implies that the samples that are used for identification purpose verify

$x(i) < x(i+1)$ for all $0 \leq i < m$ as we are considering the loading part of the limit cycle.

Step 3. The estimate κ_x° of the coefficient κ_w is computed from equation (9.20) as:

$$\kappa_x^\circ = \frac{\bar{\Phi}_{BW,1}\left(x(0)+q\right) - \bar{\Phi}_{BW}\left(x(0)\right)}{q} \tag{9.37}$$

where $x(0)$ is the value of x at the time instant $k = 0$.

Step 4. An estimate $\theta^\circ(x)$ of the function $\theta(x)$ is computed from equation (9.21) as

$$\theta^\circ\left(x(i)\right) = \bar{\Phi}_{BW}\left(x(i)\right) - \kappa_x^\circ x(i) \text{ for } i = 0, \cdots, m \tag{9.38}$$

Step 5. It has been shown in the previous section that the estimate $\theta^\circ(x)$ is strictly increasing and has a unique zero, that is there exists a unique point x_* such that $\theta^\circ(x_*) = 0$. Since all the samples $x(i)$ are such that $x(i) < x(i+1)$, we have $\theta^\circ\left(x(i)\right) < \theta^\circ\left(x(i+1)\right)$. The existence and unicity of the zero of the function θ° shows that there exists a unique integer r such that $\theta^\circ\left(x(r)\right) \leq 0 < \theta^\circ\left(x(r+1)\right)$. This implies that $x(r) \leq x_* < x(r+1)$, and a linear interpolation gives an estimate x_*° of the zero x_*. A simple computer program can be done to determine the integer r.

Step 6. An estimate of the parameter a is computed from equation (9.23) as:

$$a^\circ = \frac{\theta^\circ\left(x(r+1)\right) - \theta^\circ\left(x(r)\right)}{x(r+1) - x(r)} \tag{9.39}$$

Step 7 Choosing the design parameters $x_{*2} = x(l_2) > x_{*1} = x(l_1) > x_*^\circ$, the estimates n° and b° are computed from equations (9.24) and (9.25) as follows:

$$n^\circ = \frac{\log\left(\frac{\frac{\theta^\circ(x(l_2+1)) - \theta^\circ(x(l_2))}{x(l_2+1)-x(l_2)} - a^\circ}{\frac{\theta^\circ(x(l_1+1)) - \theta^\circ(x(l_1))}{x(l_1+1)-x(l_1)} - a^\circ}\right)}{\log\left(\frac{\theta^\circ(x_{*2})}{\theta^\circ(x_{*1})}\right)} \tag{9.40}$$

$$b^\circ = \frac{a^\circ - \frac{\theta^\circ(x(l_2+1)) - \theta^\circ(x(l_2))}{x(l_2+1)-x(l_2)}}{\theta^\circ(x_{*2})^{n^\circ}} \tag{9.41}$$

Step 8 Estimates of the parameters κ_w and ρ are computed from equations

(9.26) and (9.27) as follows:

$$\kappa_w^\circ = \sqrt[n^\circ]{\frac{a^\circ}{b^\circ}} \tag{9.42}$$

$$\rho^\circ = \frac{a^\circ}{\kappa_w^\circ} \tag{9.43}$$

Step 9 An estimate of the function $\bar{w}(x)$ is computed from equation (9.28) as follows:

$$\bar{w}^\circ\left(x(i)\right) = \frac{\theta^\circ\left(x(i)\right)}{\kappa_w^\circ} \text{ for } i = 0, \cdots, m \tag{9.44}$$

Step 10 Choose a design parameter $x_{*3} = x(l_3) < x_*^\circ$. Then an estimate of the parameter σ is computed from equation (9.29) as:

$$\sigma^\circ = \frac{1}{2}\left(\frac{\frac{\frac{\bar{w}^\circ\left(x(l_3+1)\right) - \bar{w}^\circ\left(x(l_3)\right)}{x(l_3+1) - x(l_3)}}{\rho^\circ} - 1}{\left(-\bar{w}^\circ(x_{*3})\right)^{n^\circ}} + 1\right) \tag{9.45}$$

The numerical simulation gives $\kappa_x^\circ = 2.0000$, $\kappa_w^\circ = 2.0059$, $\rho^\circ = 0.9971$, $n^\circ = 1.4954$, $\sigma^\circ = 2.9728$.

9.3 Conclusion

This chapter has presented a new identification method for the Bouc-Wen model. The method consist in exciting the hysteretic systems with two input signals that differ by a constant, and use the obtained limit cycles to derive the parameters of the Bouc-Wen model. This technique provides the exact values of the parameters in the absence of disturbances, and proves to be robust with respect to a class of perturbations of practical relevance.

Chapter 10

Adaptation of the Bouc-Wen model for the modeling and validation of a piezoelectric actuator

In this chapter, we propose a modification of the Bouc-Wen model to describe the experimentally observed behavior of a piezoelectric actuator. To identify this modified model, we have developed a new identification technique based on the results obtained in [26], where the problem of identifying the Bouc-Wen model parameters is addressed. The modified Bouc-Wen model is validated by means of experiments, and is compared to the behavior of the non-modified Bouc-Wen model.

The chapter is structured as follows. Section 10.1 shows that the model presented in the last chapter does not describe with precision the experimental behavior of the piezoelectric actuator. In Section 10.2 the modified Bouc-Wen model is introduced, along with the corresponding parameter identification methodology. Section 10.3 applies the identification technique of Section 10.2 and validates the obtained model using experiments. It also presents a comparison between the modified and non-modified Bouc-Wen models. The conclusions are summarized in section 10.4.

10.1 Experimental observations

The system under study is the patch of Figure 10.1 which is a piezoelectric actuator that contains the foil PIC-255 (Physik Instrumente). The actuator is seen as a SISO system whose input is the voltage v applied to the 3 axis and the output is the displacement y along the 1 axis. The model of the piezoelectric actuator is given by:

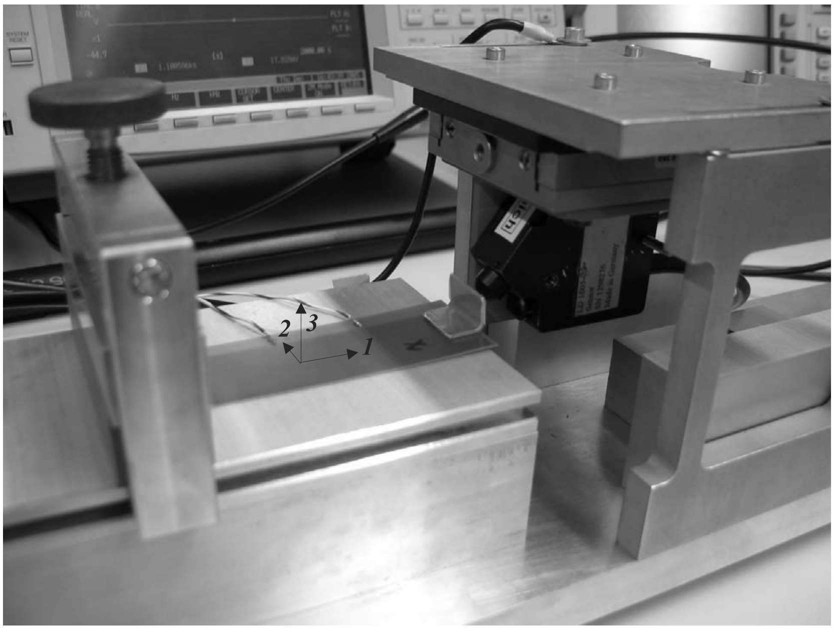

Figure 10.1: Piezoelectric patch employed for the experiments.

$$m\ddot{y}(t) + c\dot{y}(t) + k_1\left(y(t) - y_0\right) + k_2 w(t) = k_3 v(t) \tag{10.1}$$

where m is the equivalent mass of the free edge point of piezoelectric actuator, $y(t)$ its relative position with respect to the sensor, y_0 is a constant that depends on the choice of the origin, v the input voltage, and k_i, $i = 1, 2, 3$ are constant gains. The nonlinear term $w(t)$ takes into account the effect of hysteresis. We use in this section periodic input voltage functions that have a low frequency. In this case, the terms $m\ddot{y}(t)$ and $c\dot{y}(t)$ may be neglected so that the model of the piezoelectric actuator can be written as:

$$y(t) = k_v v(t) + k_w w(t) + y_0 \tag{10.2}$$

where k_v and k_w are constant gains. In the rest of the section, we approximate the nonlinear term $w(t)$ with a Bouc-Wen model and we use the identification method of Section 9.1.3 to determine its parameters. Note that the input variable is the voltage v (which plays the role of x in equations (9.1)-(9.2)), and the output variable is y (which plays the role of $\Phi(x)$ in equations (9.1)-(9.2)).

According to this methodology, two wave T-periodic voltages of low frequency $f = 0.1\ Hz$, and that differ by a constant offset of $q = 100\ V$ are applied to the actuator. Figure 10.2 upper gives the two limit cycles obtained asymptotically as a response of the actuator to the two input voltages. If the actuator were described precisely by the Bouc-Wen model, we would have from equation (9.20):

$$\bar{\Phi}_1(v+q) - \bar{\Phi}(v) = \kappa_v q \tag{10.3}$$

for any value of $v \in [V_{\min}, V_{\max}]$. Hence, such a difference would be constant so that a drag-and-drop of the two voltage-displacement curves of Figure 10.2 upper would lead to a perfect matching. However, we observe in Figure 10.2 lower that this is not the case. This means that the model composed of equations (9.1)-(9.2), (10.2) does not describe satisfactorily the experimental behavior of the piezoelectric actuator. The next section is dedicated to modifying this model so that it matches with experimental observations.

10.2 The modified model and the corresponding identification methodology

In the previous section, it has been observed that the Bouc-Wen model does not represent precisely the experimental behavior of the piezoelectric actuator. For this reason, we propose a modification of the model which consists in

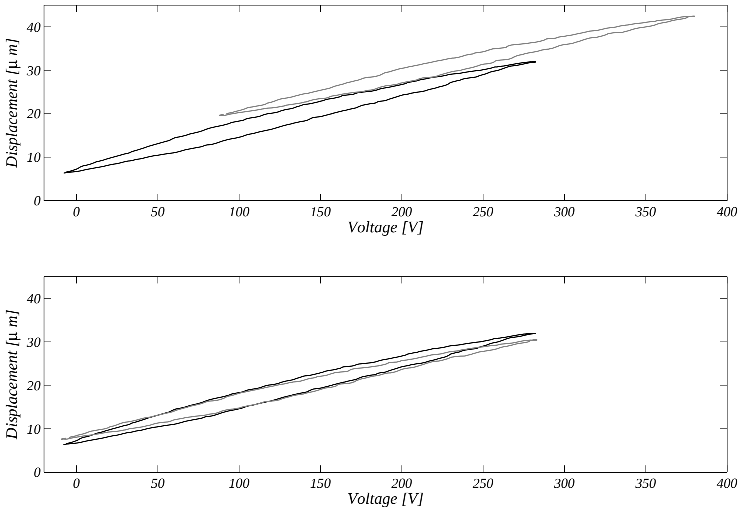

Figure 10.2: Drag and drop of the voltage-displacement curve of $100-400\ V$ input signal over the $0-300\ V$ input signal. It can be seen that the curves do not match.

introducing a higher degree polynomial in the input variable instead of a linear term. We also propose a modification of the identification methodology of Section 9.1.3.

10.2.1 Modified model

The term $\kappa_x x(t)$ of (9.1) is substituted by a polynomial function as:

$$\Phi(x)(t) = \sum_{i=1}^{N} \kappa_i x^i(t) + \kappa_w w(t) \tag{10.4}$$

where κ_i are constants to be determined. No modification is introduced in equation (9.2).

10.2.2 Non-hysteretic term parameter identification

The modification of the model implies a modification of the identification methodology. Similar to Section 9.1.3, two inputs $x(t)$ and $x(t)+q$ that differ by a constant q are applied to the piezoelectric actuator. Then, the obtained asymptotic outputs $\bar{\Phi}_1(\tau)$ and $\bar{\Phi}_2(\tau)$ can be written:

$$\bar{\Phi}_1(\tau) = \sum_{i=1}^{N} \kappa_i x^i(\tau) + \kappa_w \bar{w}_1(\tau) \tag{10.5}$$

$$\bar{\Phi}_2(\tau) = \sum_{i=1}^{N} \kappa_i \left(x(\tau) + q\right)^i + \kappa_w \bar{w}_2(\tau) \tag{10.6}$$

where $\tau \in [0, T]$. Note that we have $\bar{w}_1(\tau) = \bar{w}_2(\tau) \triangleq \bar{w}(\tau)$ from Theorem 2. Subtracting (10.6) from (10.5) it follows:

$$\bar{\Phi}_2(\tau) - \bar{\Phi}_1(\tau) = \sum_{i=1}^{N} \kappa_i \left[\left(x(\tau) + q\right)^i - x^i(\tau) \right] \triangleq \sum_{j=0}^{N-1} g_j x^i(\tau), \forall \tau \in [0, T] \tag{10.7}$$

where g_j are constant coefficients. Expanding the terms of equation (10.7) and rearranging we get:

$$\begin{pmatrix} g_0 \\ g_1 \\ g_2 \\ g_3 \\ \vdots \\ g_{N-1} \end{pmatrix} = \begin{pmatrix} q & q^2 & q^3 & q^4 & \dots & q^N \\ 0 & 2q & 3q^2 & 4q^3 & \dots & \binom{N}{N-1} q^{N-1} \\ 0 & 0 & 3q & 6q^2 & \dots & \binom{N}{N-2} q^{N-2} \\ 0 & 0 & 0 & 4q & \dots & \binom{N}{N-3} q^{N-3} \\ \vdots & \vdots & \vdots & \vdots & \ddots & \vdots \\ 0 & 0 & 0 & 0 & \dots & \binom{N}{N-k} q^{N-k} \\ \vdots & \vdots & \vdots & \vdots & \ddots & \vdots \\ 0 & 0 & 0 & 0 & \dots & \binom{N}{1} q \end{pmatrix} \times \begin{pmatrix} \kappa_1 \\ \kappa_2 \\ \kappa_3 \\ \kappa_4 \\ \vdots \\ \kappa_N \end{pmatrix} \tag{10.8}$$

which is equivalent to:

$$g_j = \sum_{k=j+1}^{N} \left(\begin{array}{c} k \\ k-j \end{array} \right) q^{k-j} \kappa_k \quad , j = 0, 1, ..., N-1 \tag{10.9}$$

Note that equation (10.9) is of the form

$$\mathbf{G} = \mathbf{Q} \times \mathbf{K} \tag{10.10}$$

On the other hand, in equation (10.7), the quantities $\bar{\Phi}_2(\tau)$, $\bar{\Phi}_1(\tau)$ and $x(\tau)$ are experimental data, the integer N is chosen, and the constants g_0, $\cdots$, g_{N-1} are unknowns to be determined using regression techniques. Hence, the matrix **K** of equation (10.10) can be determined as:

$$\mathbf{K} = \mathbf{Q}^{-1} \times \mathbf{G} \tag{10.11}$$

where **Q** is invertible since $q \neq 0$. The simplest case is when $N = 1$, and corresponds to the model (9.1)-(9.2).

If we take $N = 2$, then we get:

$$\mathbf{Q} = \left(\begin{array}{cc} q & q^2 \\ 0 & 2q \end{array} \right) \tag{10.12}$$

so that:

$$\mathbf{K} = \mathbf{Q}^{-1}\mathbf{G} \rightarrow \left(\begin{array}{c} \kappa_1 \\ \kappa_2 \end{array} \right) = \left(\begin{array}{cc} \frac{1}{q} & -\frac{1}{2} \\ 0 & \frac{1}{2q} \end{array} \right) \left(\begin{array}{c} g_0 \\ g_1 \end{array} \right) = \left(\begin{array}{c} \frac{g_0}{q} - \frac{g_1}{2} \\ \frac{g_1}{2q} \end{array} \right) \tag{10.13}$$

10.2.3 Hysteretic term parameter identification

The hysteretic part of the model is obtained from equation (10.4) as:

$$\kappa_w \bar{w}(\tau) = \bar{\Phi}(\tau) - \sum_{i=1}^{N} \kappa_i x^i(\tau), \forall \tau \in [0, T] \tag{10.14}$$

The identification method of the parameters characterizing the hysteretic term has been described in section 9.1.3. To determine the intermediate parameters a and b, and the relevant parameters n, ρ, κ_w, σ, the design parameters x_*, x_{*1}, x_{*2}, x_{*3} have to be chosen as in Table 10.1.

Table 10.1: Design parameters.

	Input	Condition	Curve region	Comments
1	x_*	$\theta(x_*) = 0$	$\bar{w}(x) = 0$	
2	x_{*1}	$x_{*1} > x_*$	$\bar{w}(x) > 0$	in the linear region
3	x_{*2}	$x_{*2} > x_{*1} > x_*$	$\bar{w}(x) > 0$	close to the largest voltage value
4	x_{*3}	$x_{*3} < x_*$	$\bar{w}(x) < 0$	close to the smallest voltage value

The unknown parameters are calculated according to Table 10.2.

Table 10.2: Parameter expressions

Parameter	Expression	Parameter	Expression
a	$\left(\frac{d\theta(x)}{dx}\right)_{x=x_*}$	n	$\frac{\log\left(\frac{\left(\frac{d\theta(x)}{dx}\right)_{x=x_{*2}}{}^{-a}}{\left(\frac{d\theta(x)}{dx}\right)_{x=x_{*1}}{}^{-a}}\right)}{\log\left(\frac{\theta(x_{*2})}{\theta(x_{*1})}\right)}$
b	$\frac{a-\left(\frac{d\theta(x)}{dx}\right)_{x=x_{*2}}}{\theta(x_{*2})^n}$	κ_w	$\sqrt[n]{\frac{a}{b}}$
ρ	$\frac{a}{\kappa_w}$	σ	$\frac{1}{2}\left(\frac{\frac{\left(\frac{d\bar{w}(x)}{dx}\right)_{x=x_{*3}}}{\rho}-1}{(-\bar{w}(x_{*3}))^n}+1\right)$

10.3 Piezoelectric actuator modeling

10.3.1 Experimental setup

The system under study is sketched in Figure 10.3. The actuator is driven by means of a power amplifier whose working voltage is set by a function generator where the reference waves are introduced.

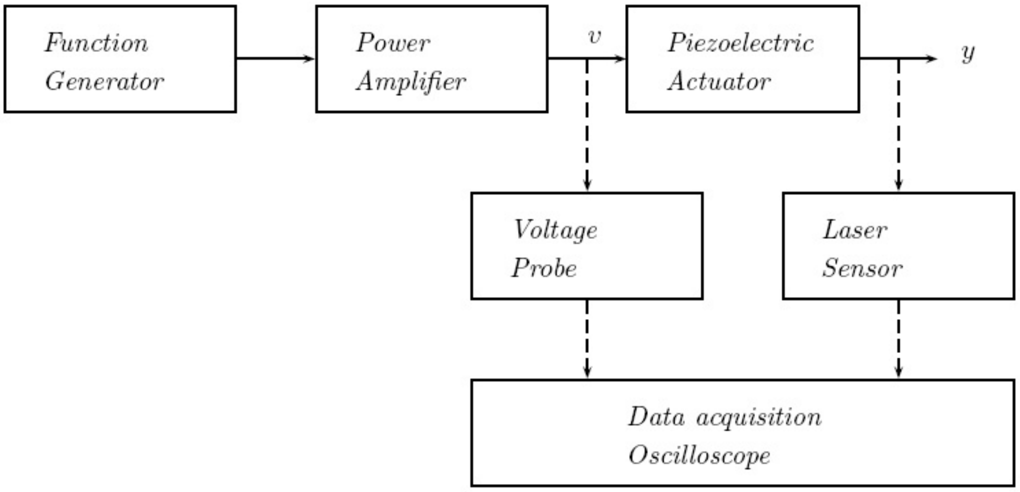

Figure 10.3: Block diagram of the experiment.

The actuator employed (Fig. 10.1) is a patch where the voltage v is applied in the 3 axis and the main displacement y is performed in the 1 axis. Such an actuator can be used in a number of applications ranging from active control of structures to micro-positioning and optics applications. For the sake of completeness, we give the physical characteristics of the patch. The piezoelectric ceramic used is a PI (Physik Instrumente) PIC-255. The material shows a d_{31} piezoelectric coefficient of $-180 \cdot 10^{-12}$ m/V, dielectric permittivity $\varepsilon_{33}^{T}/\varepsilon_0$ of 1800, elastic constant s_{11}^{E} of $16.1 \cdot 10^{-12}$ m^2/N, density of 7.80 gr/cm^3 and Curie temperature of 350 ^oC. The piezoelectric foil shows a mass of 2.34 g. and dimensions of 50 $mm \times 30$ $mm \times 0.2$ mm and the entire patch a mass of 3.405 g. and dimensions of 60 mm × 35 mm × 0.5 mm.

The piezoelectric actuator lays in a low friction surface where it is clamped in one extreme and left free in the other in order to allow its free movement. The piezoelectric actuator has been previously polarized with a constant voltage of 450 V during 5 min in order to ensure its optimal performance.

An *Ono-Sokki Multi-Purpose FFT Analyser CF-5220* has been used as a function generator to generate triangular, sinusoidal and random functions. The amplifier employed is a *PI (Physik Instruments)* with the modules E-

107 and E-111. The voltage v is measured with a probe *Tes(A)tec TT-SI-9002*. The displacement of the free edge of the piezoelectric actuator is measured by means of a laser triangulator *Micro-Epsilon optoNCDT 1607* with range 500 μm - ± 10 V, bandwith of 10 kHz and resolution of 0.1 μm. The data has been acquired with a four channel *Tektronix TDS 3014* (bandwidth 100 MHz). All the quantities have been sampled depending on the function under study so that 10000 samples for each plot (including two or three full periods) are provided.

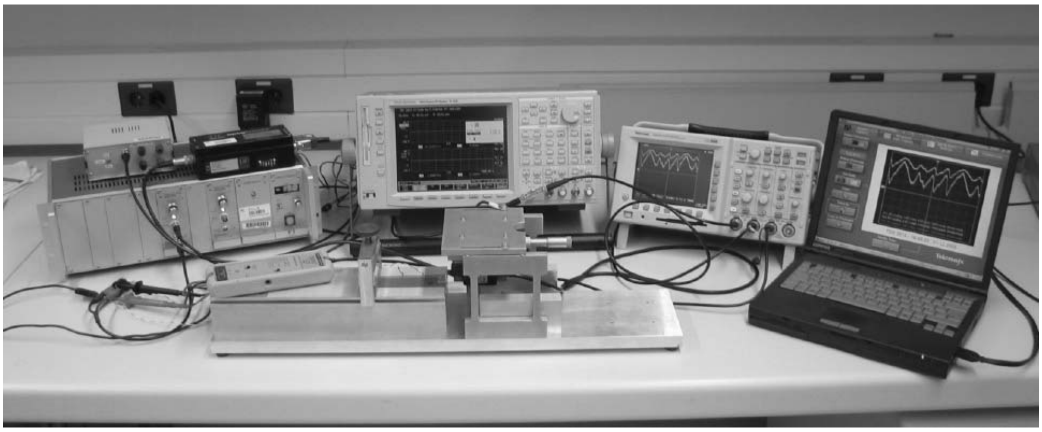

Figure 10.4: Experimental layout.

10.3.2 Identification procedure

The actuator under study has been identified using the methodology described in section 10.2.2. Similar to Section 10.1, it follows from equations (10.1) and (10.4) that:

$$y(t) = \sum_{i=1}^{N} \kappa_i v^i(t) + \kappa_w w(t) + y_0 \tag{10.15}$$

As it can be seen in Fig. 10.5, the input and output signals are corrupted by noise. Since the identification method uses the values of the derivatives at some points of the limit cycle, it is necessary to filter the data before applying the identification algorithm. To this end, a second order filter of the form $\frac{\omega_n^2}{s^2 + 2\zeta\omega_n s + \omega_n^2}$ is used, with $\zeta = 0.7$ and $\omega_n = 50 \times \omega_s$ where $\omega_s = 0.1 \times 2\pi \ rad/s$ is the frequency of the voltage input signal. The fact that the bandwidth of the filter is much larger than the frequency of the voltage input and displacement output signals, implies that the filtering process eliminates only the high frequency disturbances while introducing very little deformation on the relevant data.

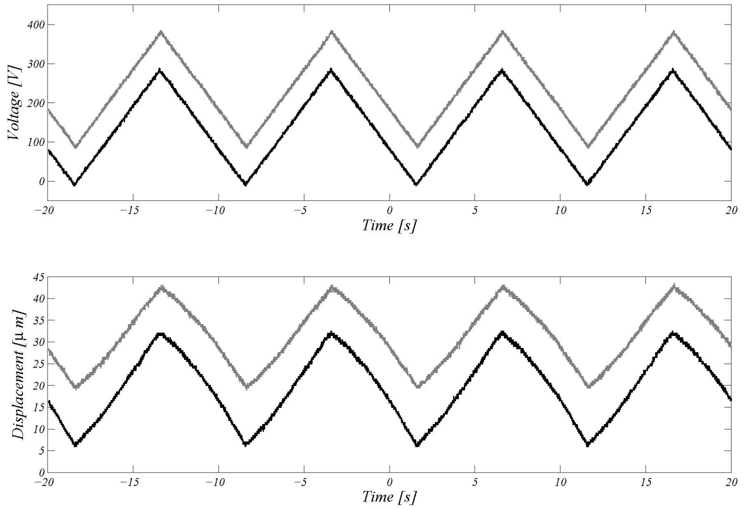

Figure 10.5: Input and output signals.

The input and output signals are plotted in Fig. 10.5. As the identification methodology of Sections 10.2.2 and 10.2.3 uses the asymptotic values of the output signal $y(t)$, the model (10.15) is rewritten as:

$$\bar{y}(\tau) = \sum_{i=1}^{N} \kappa_i v^i(\tau) + \kappa_w \bar{w}(\tau) + y_0, \forall \tau \in [0, T] \tag{10.16}$$

where the quantities $\bar{y}$ and $\bar{w}$ set for the limit functions of y and w as described in Theorem 2. As explained in section 10.2.2 the coefficients g_j are determined by means of regression analysis. The results are given in Table 10.3.

Table 10.3: The g_i coefficients

N	g_1	g_2	g_3	g_4
1	1.1736e-005	-	-	-
2	1.3091e-005	-9.8691e-009	-	-
3	1.3116e-005	-1.0447e-008	2.1060e-012	-
4	1.3151e-005	-1.2285e-008	1.9438e-011	-4.2099e-014

For each value of N, we get a set $\{g_0, g_1, ...g_{N-1}\}$. This set of values determines the parameters $\{\kappa_1, \kappa_2, ...\kappa_N\}$ using equation (10.11).

To compute the parameter y_0, we integrate equation (10.16) over the period $[0, T]$, taking into account the fact that, due to Theorem 2, we have $\int_0^T \bar{w}(\tau)d\tau = 0$:

$$y_0 = \frac{1}{T}\int_0^T \left(\bar{y}(\tau) - \sum_{i=1}^{N} \kappa_i v^i(\tau)\right) d\tau \tag{10.17}$$

The obtained coefficients are given in Table 10.4. At this point, the hysteretic term can be obtained from equation (10.14). Then, we use the methodology described in sections 9.1.3 and 10.2.3 to determine the parameters n, ρ, κ_w and σ. The obtained parameters are given in table 10.5. Note that the input variable is $-v$ instead of v so that the loading and unloading lead to a clockwise limit cycle as expected for the Bouc-Wen model.

Table 10.4: Coefficients κ_i

N	y_0	κ_1	κ_2	κ_3	κ_4
1	3.0587e-006	1.2117e-007	-	-	-
2	1.7858e-006	1.401e-007	-5.0949e-011	-	-
3	1.7715e-006	1.4068e-007	-5.4986e-011	7.2482e-015	-
4	1.7463e-006	1.4223e-007	-7.4161e-011	8.7947e-014	-1.0867e-016

10.3.3 Model validation

The results have been validated with a periodic sinusoidal function between 0 and 400 V and non-periodic random function. The initial condition of the

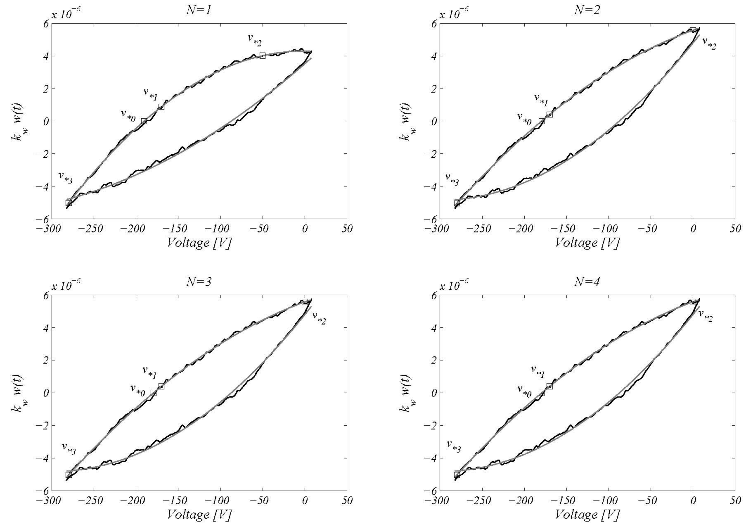

Figure 10.6: Points used to determine the Bouc-Wen model parameters κ_w, n, ρ and σ. In bold filtered experimental data. In grey fitted data for the computation of the derivatives.

Table 10.5: Bouc-Wen model parameters

N	n	ρ	κ_w	σ
1	1.27	0.00893	5.08e-006	0.74
2	1.12	0.0047	9.22e-006	0.812
3	1.12	0.00463	9.35e-006	0.815
4	1.12	0.00461	9.37e-006	0.815

model can be obtained from equation (10.15) as

$$w(0) = \frac{y(0) - \sum_{i=1}^{N} \kappa_i v^i(0) - y_0}{\kappa_w} \tag{10.18}$$

where $y(0)$, κ_i, $v(0)$, y_0 and κ_w are available.

Figures 10.7(a) and 10.10(a) give the output of the model (10.15) for $N = 1$ and $N = 2$, along with the experimental output of the actuator. It can be observed that the model matches better the experimental data for $N = 2$. This conclusion can also be drawn from Figures 10.7(b) and 10.10(b), where the difference between the model and the experimental output is plotted for $N = 1$ and $N = 2$. It can be observed that after a transient phase, the error is smaller for $N = 2$. The same conclusions can be drawn from the displacement-voltage plot of Figure 10.9. Other experiments for $N \geq 3$ show that the behavior of the model for such values of N is not significantly different from that of $N = 2$.

10.4 Conclusion

The chapter has focused on the modeling of a piezoelectric actuator using a modified version of the hysteresis Bouc-Wen model. The modification consists in representing the non-hysteretic part of the model as a degree N polynomial instead of a linear relationship. The results for different values of N have been computed and compared with the real displacements of the actuator. The modified model has proven to match better the experimental data for $N > 1$.

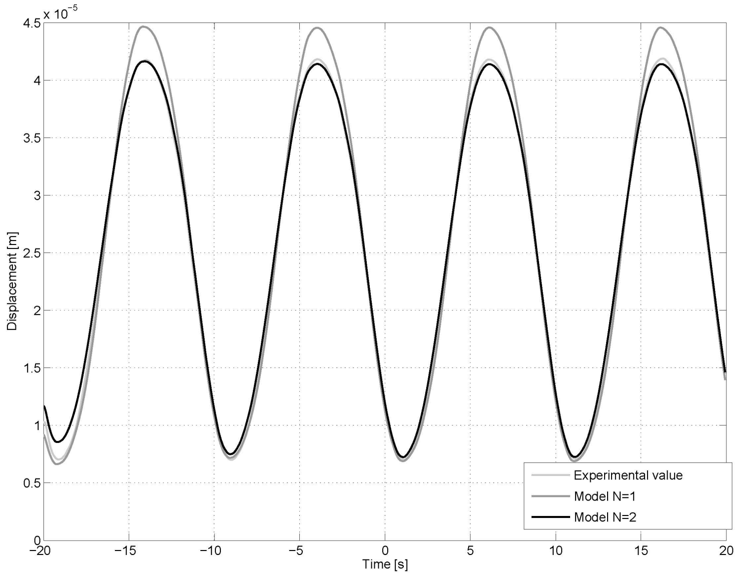

(a) Experimental output and model output for $N = 1$ and $N = 2$.

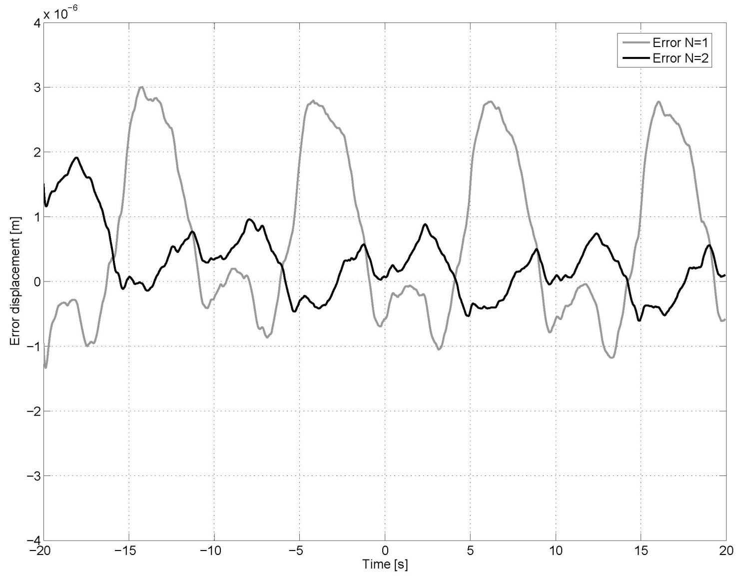

(b) Model error for $N = 1$ and $N = 2$.

Figure 10.7: Model response to a sinusoidal input.

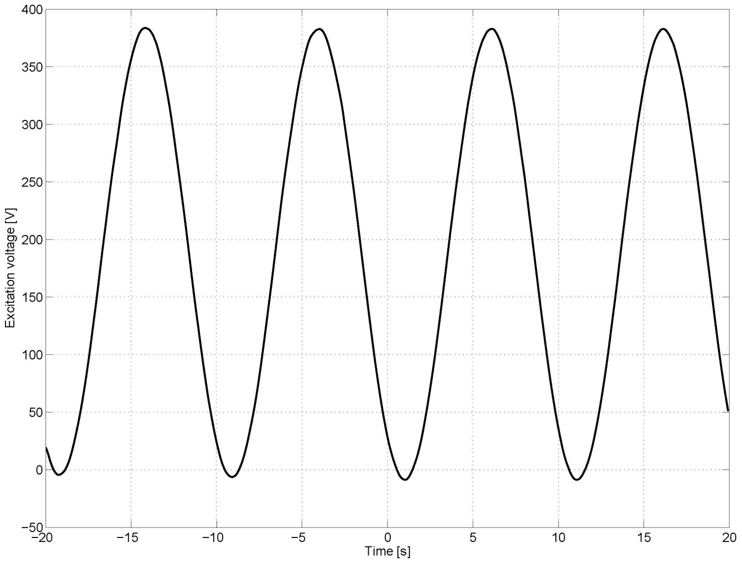

Figure 10.8: Excitation voltage

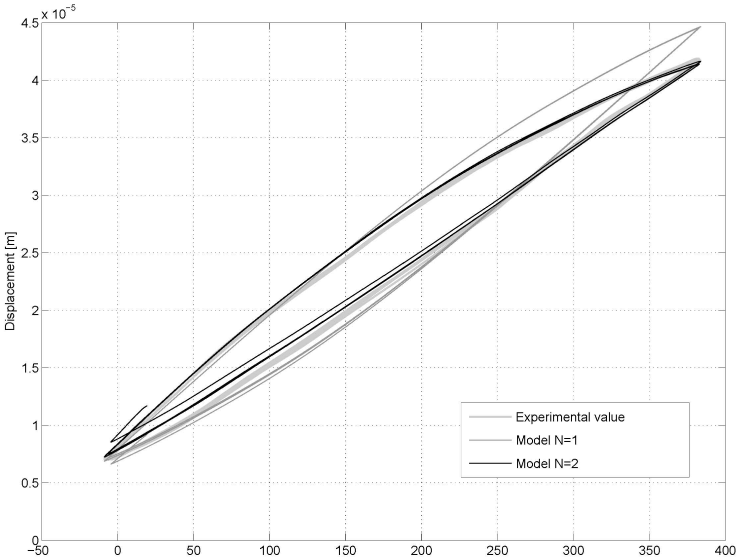

Figure 10.9: Displacement - Voltage plot of the response to a sinusoidal input

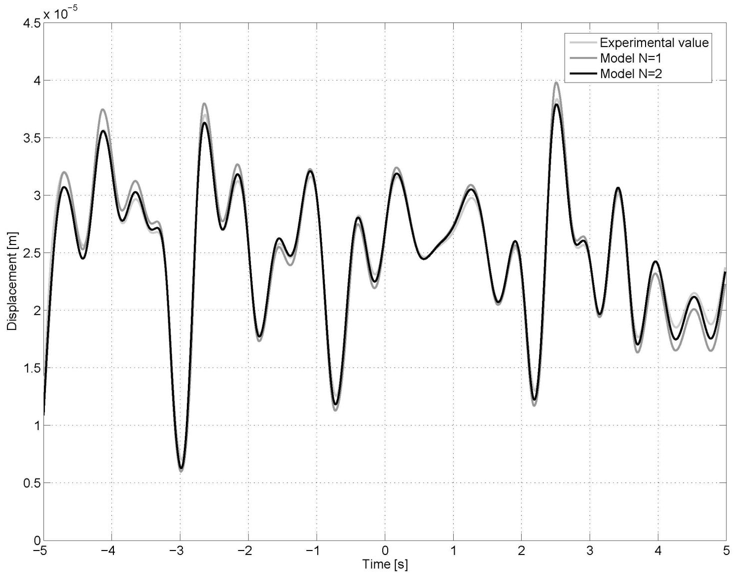

(a) Experimental output and model output for $N = 1$ and $N = 2$.

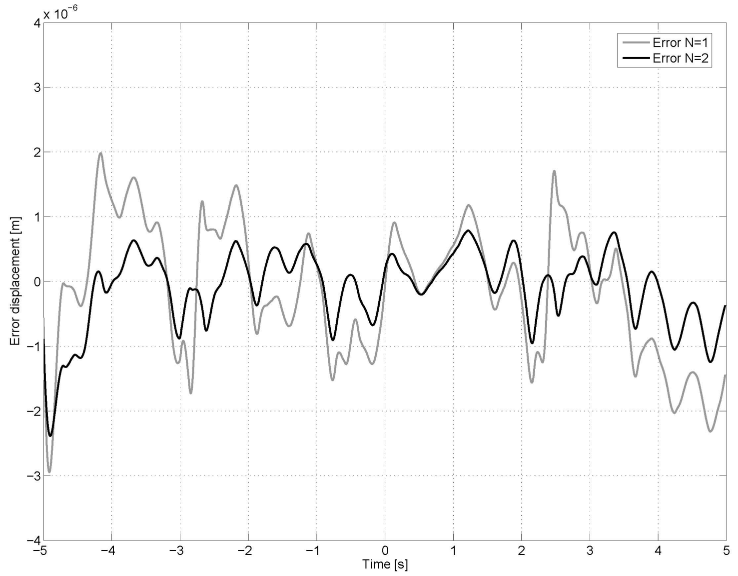

(b) Model error for $N = 1$ and $N = 2$.

Figure 10.10: Model response to a random input.

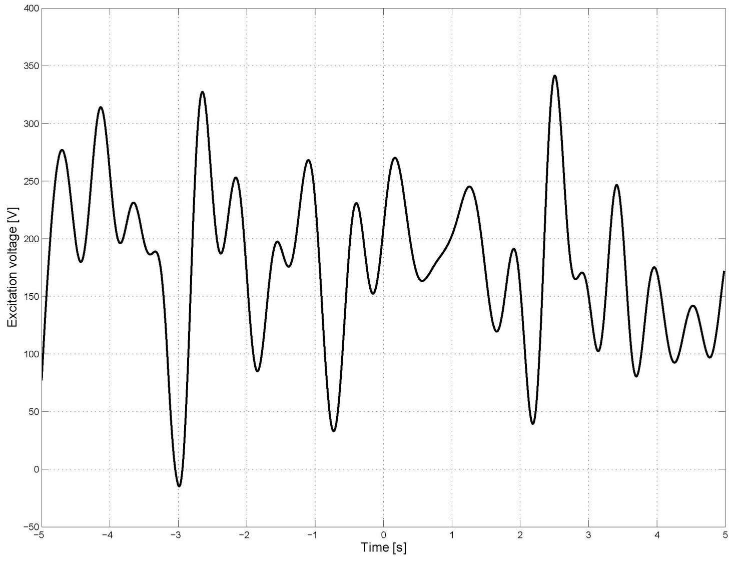

Figure 10.11: Excitation voltage

Chapter 11

Control of a piezoelectric actuator considering the hysteresis

This chapter deals with the modeling and control of a piezoelectric actuator. The main challenge for the control design is the presence of hysteresis. This nonlinearity is represented in this chapter using the Bouc-Wen model and a time-varying PID controller is designed for micropositionning purpose. The performance of the controller is tested using numerical simulations and experimentally.

We consider the problem of micropositionning using a piezoelectric actuator. This problem has spurred much interest in the current literature. A robust controller is employed in [6] to control a piezoelectric bimorph actuator using the Bouc-Wen model. In [24] a piezoelectric actuator is modeled with neural networks and controlled with a variable structure control system. In [59], the controller uses information of the charge instead of the voltage for the control of position. This technique takes advantage of the reduced hysteresis between the displacement and the electrical charge, but presents some difficulty for the measurement of the charge. Since the piezoelectric device is represented in this work using the Bouc-Wen model, the results of [31] are used and improved for the control of the piezoelectric element. In

[31], a second-order mechanical system that includes a Bouc-Wen hysteresis is considered for control purposes. The control objective is to guarantee the global boundedness of all the closed loop signals, and the regulation of both the displacement and the velocity of the device to zero. This objective is achieved using a simple PID controller. However, the main drawback of this controller is that the equilibrium point of the closed loop system is not robust vis-à-vis perturbations which is undesirable in practice. The main contributions of this chapter are the following:

- We present a new control law which is a time-varying PID that guarantees that the equilibrium point of the closed loop is robust to perturbations.
- This control law is tested in numerical simulations and experimentally using a piezoelectric actuator.

The main advantage of the proposed control law over other existing control schemes, is that it is simple to implement in an industrial context.

11.1 Background results. PID control of a Bouc-Wen hysteresis

We consider the second order mechanical system described by:

$$m\ddot{x} + c\dot{x} + \Phi(x)(t) = u(t), \tag{11.1}$$

with initial conditions $x(0)$, $\dot{x}(0)$ and excited by a control input force $u(t)$. The output restoring force Φ is assumed to be described by the normalized Bouc-Wen model [29]:

$$\begin{aligned} \Phi(x)(t) &= \kappa_x x(t) + \kappa_w w(t), & (11.2)\\ \dot{w}(t) &= \rho\left(\dot{x}(t) - \sigma|\dot{x}(t)|\,|w(t)|^{n-1}w(t) + (\sigma-1)\dot{x}(t)|w(t)|^{n}\right) & (11.3) \end{aligned}$$

with an initial condition $w(0)$. The parameters $n \geq 1$, $\rho > 0$, $\sigma \geq \frac{1}{2}$, $\kappa_x > 0$, $\kappa_w > 0$, $m > 0$ and $c \geq 0$ are unknown. The range of the parameters corresponds to the Class I Bouc-Wen model which is stable, asymptotically dissipative and thermodynamically consistent [29]. The displacement $x(t)$ and velocity $\dot{x}(t)$ are available through measurements, but the signal $w(t)$ is not. Let $y_r(t)$ be a (known) smooth and bounded reference signal whose (known) smooth and bounded derivatives are such that $\lim_{t\to\infty} y_r(t) = \lim_{t\to\infty} \dot{y}_r(t) = \lim_{t\to\infty} \ddot{y}_r(t) = \lim_{t\to\infty} y_r^{(3)}(t) = 0$ exponentially. This means that there exist some constants $a > 0$ and $b > 0$ such that $\left|y_r^{(i)}(t)\right| \leq ae^{-bt}$ for $t \geq 0$ and $i = 0, 1, 2, 3$.

The control objective is to globally asymptotically regulate the displacement $x(t)$ and velocity $\dot{x}(t)$ to the reference signals $y_r(t)$ and $\dot{y}_r(t)$ preserving the global boundedness of all the closed loop signals; that is $x(t)$, $\dot{x}(t)$, $w(t)$ and $u(t)$.

We assume the following:

Assumption 2 *The unknown parameters lie in known intervals. That is we have* $m \in [m_{\min}, m_{\max}]$ *with* $m_{\min} > 0$, $c \in [0, c_{\max}]$, $\kappa_x \in (0, \kappa_{x_{\max}}]$, $\kappa_w \in (0, \kappa_{w_{\max}}]$, $\sigma \in \left[\frac{1}{2}, \sigma_{\max}\right]$, $\rho \in (0, \rho_{\max}]$.

Note that the unknown structure parameter $n \geq 1$ is not required to lie in a known interval.

The problem of controlling the system (11.1)-(11.3) has been treated in [31], where it is demonstrated that a PID control insures that the displacement and velocity errors tend to zero. Introduce the variables:

$$x_1(t) = x(t) - y_r(t), \;\; x_2(t) = \dot{x}(t) - \dot{y}_r(t), \;\; x_0(t) = \int_0^t x_1(\tau)d\tau \tag{11.4}$$

and choose as a control law the PID controller:

$$u(t) = -k_0 x_0(t) - k_1 x_1(t) - k_2 x_2(t) \tag{11.5}$$

where the k_i's are design parameters. Then we have [31]:

Theorem 4 *Consider the closed loop formed by the system (11.1)-(11.3) and the control law (11.5). Define the following constants:*

$$\begin{aligned} k_{2_{\min}} &= \sqrt{2m_{\max}\left(\sigma_{\max}\rho_{\max}\kappa_{w_{\max}} + \kappa_{x_{\max}} + k_1\right)} && (11.6)\\ e_1 &= \frac{\left(c_{\max}+k_2\right)^3}{m_{\min}^2} \\ e_2 &= \frac{k_1^2}{m_{\max}^2}\left(k_2^2 - k_{2_{\min}}^2\right) \\ k_{0_{\max}} &= \min\left(\frac{k_1k_2}{m_{\max}}, -e_1 + \sqrt{e_1^2+e_2}\right) && (11.7) \end{aligned}$$

and choose the design gains k_0, k_1 and k_2 in the following way: take any positive value for k_1; then choose k_2 such that $k_2 > k_{2_{\min}}$; finally take $0 < k_0 < k_{0_{\max}}$. In this case we have the following:

1. *All the closed loop signals x_0, x_1, x_2, w and the control u are globally bounded.*
2. $\lim_{t\to\infty} x(t) = 0$ *and* $\lim_{t\to\infty} \dot{x}(t) = 0$.

11.2 Experimental Platform

11.2.1 Experimental Layout

The system under study is the patch of Figure 11.1 which is a piezoelectric actuator that contains the foil PIC-255 (Physik Instrumente). The actuator is seen as a SISO system whose input is the voltage u applied to the 3 axis and the output is the displacement y along the 1 axis.

The actuator can be used in a number of applications ranging from active control of structures to micro-positioning and optics applications. For the sake of completeness, we give the physical characteristics of the patch. The piezoelectric ceramic used is a PI (Physik Instrumente) PIC-255. The material shows a d_{31} piezoelectric coefficient of -180×10^{-12} m/V, dielectric permittivity $\varepsilon_{33}^T/\varepsilon_0$ of 1800, elastic constant s_{11}^E of 16.1×10^{-12} m^2/N, density of 7.80 gr/cm^3 and Curie temperature of 350 ^{o}C. The piezoelectric foil

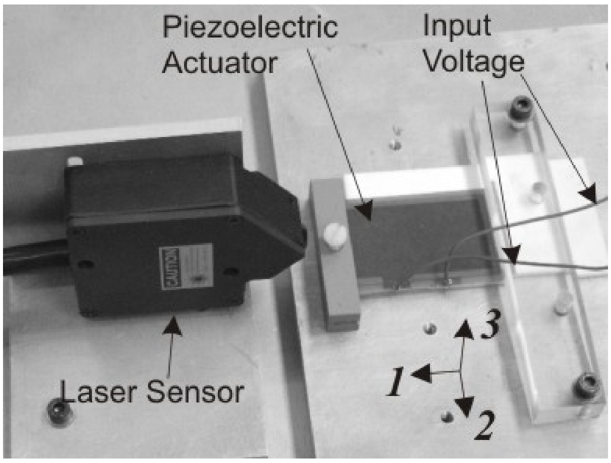

Figure 11.1: Controlled piezoelectric actuator.

shows a weight of 2.34 gr. and dimensions of 50 mm ×30 mm ×0.2 mm and the entire patch a weight of 3.405 gr. and dimensions of 60 mm ×35 mm ×0.5 mm. The piezoelectric actuator lays in a low friction surface where it is clamped in one extreme and left free in the other in order to allow its free movement. It has been previously polarized with a constant voltage of 450 V during 5 min in order to ensure its optimal performance.

The experiments have been undertaken with the platform sketched in Figure 11.2. The control is performed by a *DSP*[1] Controller. The actuator is driven by means of a power amplifier whose working voltage is set by the *DSP* controller. The amplifier can work with voltages between −450 V and 450 V with a maximum current of 100 mA.

The displacement of the free edge of the piezoelectric actuator is measured using a laser triangulator *Micro-Epsilon optoNCDT 1607* with range 500 μm, bandwidth 10 kHz and resolution 0.1 μm. The data has been acquired with a four channel *Yokogawa DL9000* (bandwidth 500 MHz). All the quantities have been sampled so that at least 25000 samples are provided for each plot.

---

[1] DSP stands for digital signal processor

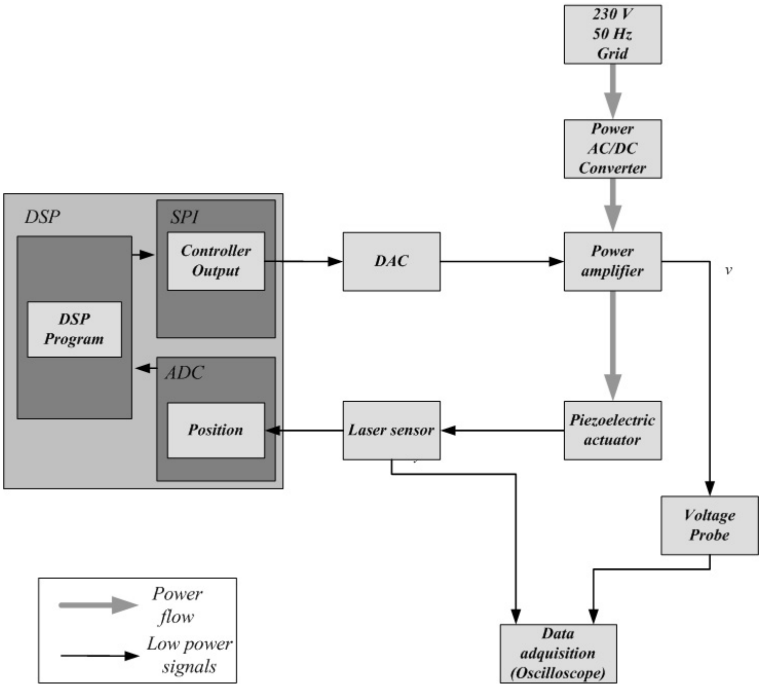

Figure 11.2: Block diagram of the platform.

11.2.2 System modeling

The system model is given by [6]:

$$m'\ddot{x}(t) + c'\dot{x}(t) + \kappa_a x(t) = \kappa_b \Phi(u)(t) \tag{11.8}$$

where κ_a and κ_b are elastic constants, m' and c' are the equivalent mass and damping coefficient of the piezoelectric actuator, $x(t)$ its relative position with respect to the sensor, and $k_b\Phi(u)(t)$ is the force produced by the actuator. The term $\Phi(u)(t)$ is assumed to follow a Bouc-Wen equation so that the actuator may be represented by:

$$m'\ddot{y}(t) + c'\dot{y}(t) + \kappa_a\left(y(t) - y_0\right) = \kappa_b\kappa'_x u(t) + \kappa_b\kappa'_w w(t), \tag{11.9}$$

$$\dot{w}(t) = \rho\left(\dot{y}(t) - \sigma|\dot{y}(t)|\,|w(t)|^{n-1}w(t) + (\sigma-1)\dot{y}(t)|w(t)|^{n}\right) \tag{11.10}$$

where κ'_w and κ'_x are constant gains. The nonlinear term $w(t)$ takes into account the effect of hysteresis.

Defining:

$$m = \frac{m'}{\kappa_a\kappa'_x}\ ,\ c = \frac{c'}{\kappa_a\kappa'_x}\ ,\ \kappa_x = \frac{\kappa_a}{\kappa_b k'_x}\ ,\ \kappa_w = -\frac{\kappa'_w}{\kappa'_x} \tag{11.11}$$

it can be seen that the actuator follows equations (11.1)-(11.3). This model is valid only for low frequencies (well below the resonance of the actuator), as an important mismatch has been observed experimentally for high frequencies.

11.2.3 Control objective

The control objective is to insure the boundedness of all the closed loop signals, along with the regulation of the displacement and velocity of the piezoelectric actuator to zero. Furthermore, in steady-state, the control output has to have a unique value so that the closed loop system has a unique equilibrium point.

11.3 Parameter identification

The system under consideration is described by equations (11.1)-(11.3) in which the system parameters m, c along with the Bouc-Wen model parameters κ_x, κ_w, ρ, σ, n are unknown. The objective of this section is to determine these parameters using the measurements of the relative displacement $x(t)$ and the voltage input $u(t)$. Since we are dealing with a model valid only for low frequencies, the terms $m\ddot{x}$ and $c\dot{x}$ can be neglected in equation (11.1) so that the actuator model can be approximated by equations (11.2)-(11.3).

The problem of identifying the parameters of the Bouc-Wen model (11.2)-(11.3) has been treated in references [26; 30]. The technique presented in those references consists in choosing for $u(t)$ a periodic signal with a loading-unloading shape (that is a wave periodic signal [29]). This implies that $x(t)$ is also wave periodic so that a limit cycle (x, u) is obtained asymptotically. The experimentally obtained limit cycle is then used to determine the unknown Bouc-Wen model parameters.

The identified parameters are given in Figure 11.3. It can be seen that these parameters are almost constant in the fequency range $[0, 100 \text{ Hz}]$. The parameters values are shown in Table 11.1.

Table 11.1: Identified parameters.

Parameter	Smallest Value	Largest Value	Mean Value	Unit
n	1.16	1.192	1.176	-
σ	0.9094	0.9212	0.9153	-
ρ	7.632×10^4	9.5×10^4	8.566×10^4	m^{-1}
k_w	39.97	48.74	43.57	V
k_x	9.83×10^6	10.8×10^6	10.35×10^6	$\mathrm{V\ m}^{-1}$

For higher values of the frequency, the Bouc-Wen model parameters are highly frequency dependent.

The model (11.2)-(11.3) is tuned with the parameters obtained in Table 11.1 (column 4), and the initial condition is calculated from equation (11.2)

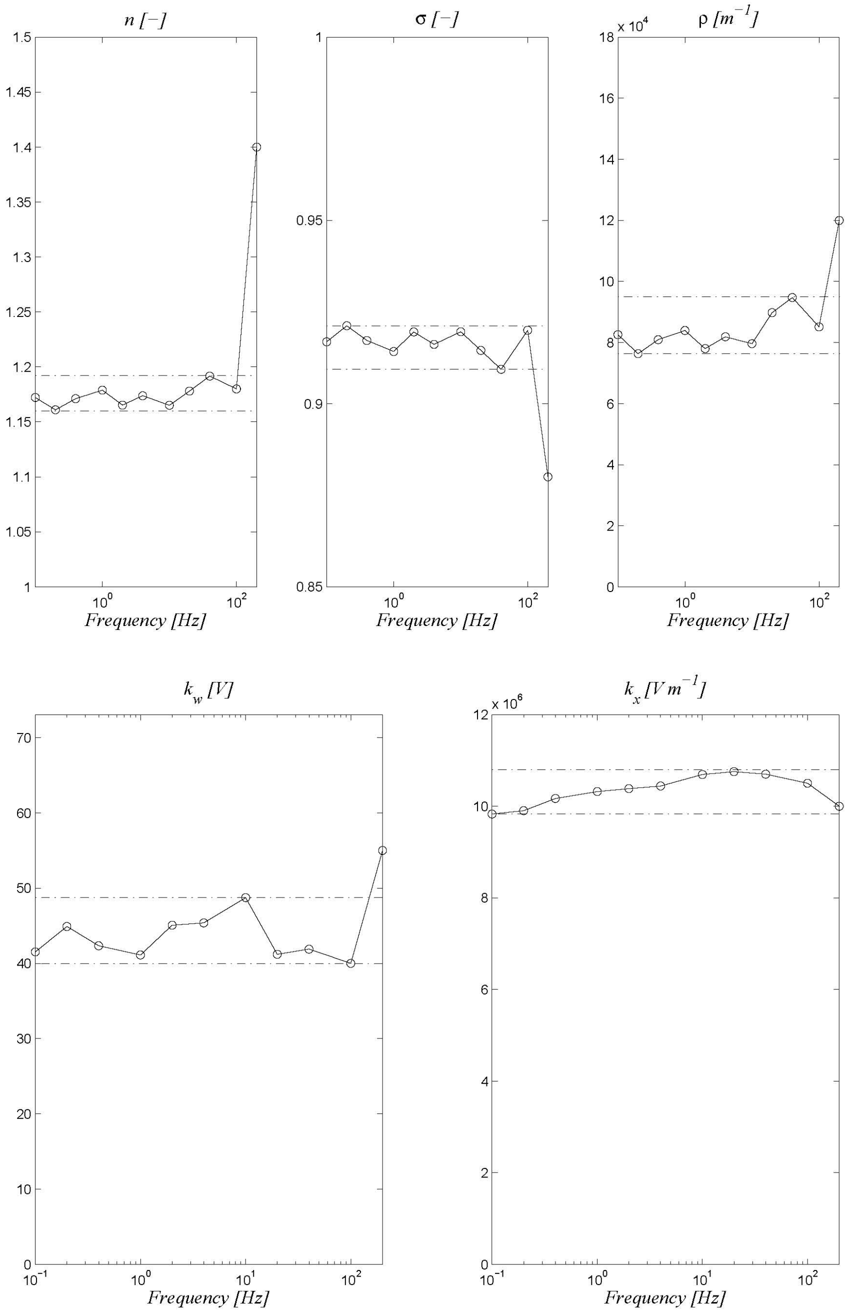

Figure 11.3: Identified parameters for different input frequencies.

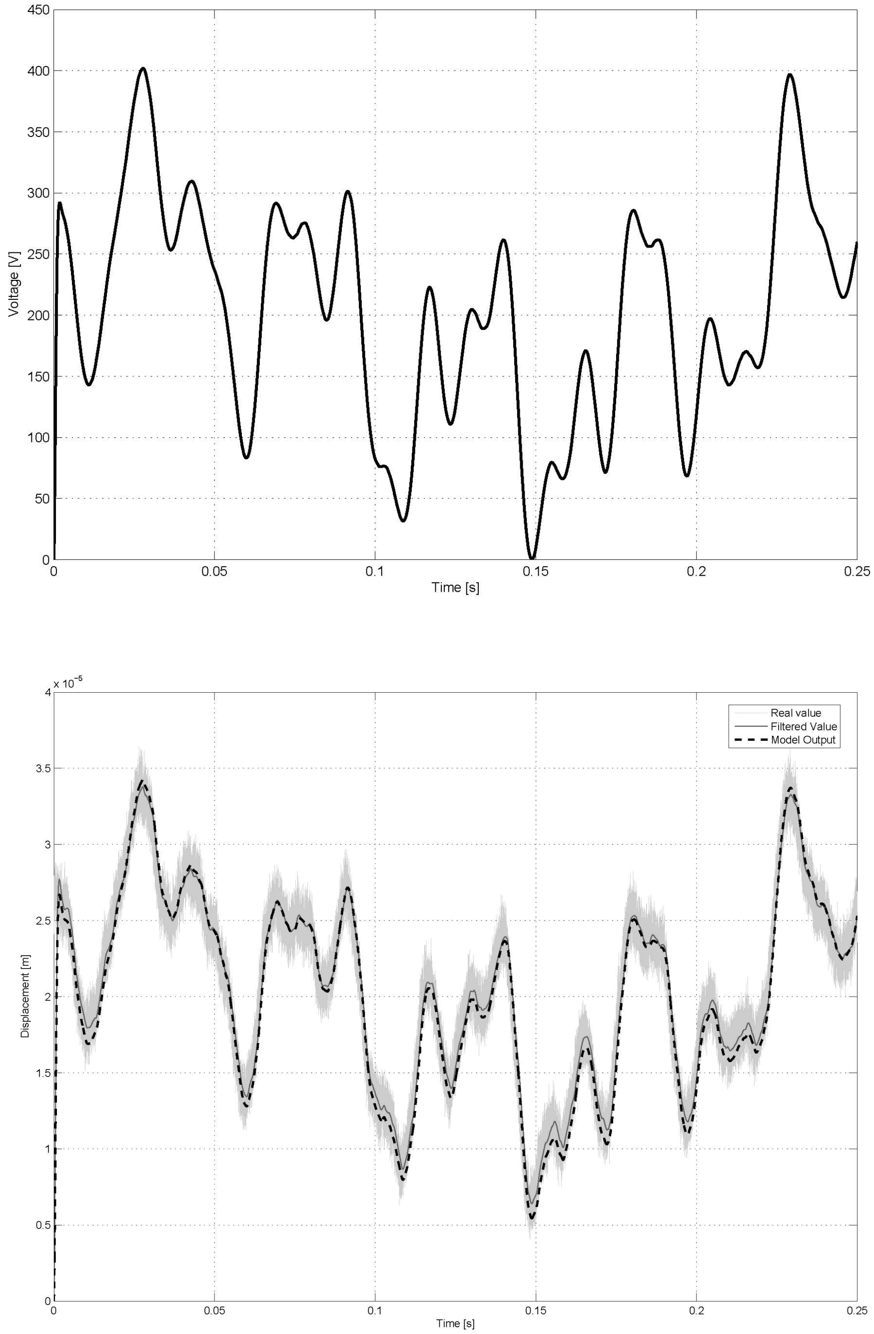

Figure 11.4: Model response to a random input function.

as

$$w(0) = \frac{u(0) - k_x x(0)}{k_w} \tag{11.12}$$

To check the validity of this model, it is excited with a random signal whose frequency content lies in the interval $[0, 100\ \mathrm{Hz}]$. Figure 11.4 gives the responses of both the model and the actuator. A reasonable match is observed.

11.4 Control laws

This section introduces three control laws for the piezoelectric device, which are based on the linear controller of Section 11.1. These controllers are tested by means of numerical simulations.

11.4.1 PID Control

In this section we consider the closed loop formed by the system (11.1)-(11.3) along with the control law (11.5). The closed loop is then described by the equations:

$$\begin{aligned}
\dot{x}_0 &= x_1, && (11.13)\\
\dot{x}_1 &= x_2, && (11.14)\\
\dot{x}_2 &= m^{-1}\left(-\left(c+k_2\right)x_2 - \left(\kappa_x + k_1\right)x_1 - k_0 x_0 - \kappa_w w\right.\\
&\quad \left.-m\ddot{y}_r - c\dot{y}_r - \kappa_x y_r\right), && (11.15)\\
\dot{w} &= \rho\left(x_2 + \dot{y}_r - \sigma|x_2 + \dot{y}_r|\,|w|^{n-1}w + (\sigma - 1)\left(x_2 + \dot{y}_r\right)|w|^n\right) && (11.16)
\end{aligned}$$

In order to determine the PID constants k_0, k_1 and k_2, we need to have known bounds on the unknown parameters (Assumption 2). The identification process of Section 11.3 gives these bounds for the Bouc-Wen model parameters κ_x, κ_w, ρ, σ, n. Section 11.2.1 gives information on the rest of the system parameters. We use the following bounds:

- $m_{\min} = 3.98 \times 10^{-3}\ \mathrm{V\ s^2\ m^{-1}}$

- $m_{\max} = 6.63 \times 10^{-3}$ V s^2 m^{-1}
- $c_{\max} = 13.43$ V s m^{-1}
- $k_{x\max} = 10.8 \times 10^6$ V m^{-1}
- $\sigma_{\max} = 0.9212$
- $\rho_{\max} = 9.510 \times 10^4$ m^{-1}
- $k_{w\max} = 48.74$ V

The PID controller parameters are determined using Theorem 4. The first design parameter to be chosen is $k_1 = 5 \times 10^6$ so that we get $k_{2min} = 567.6$. We choose $k_2 = 580$ so that we obtain $k_{0max} = 1.16 \times 10^9$. Finally we take $k_0 = 1 \times 10^9$.

Figure 11.5 gives the behavior of the closed loop signals with $m = 5.3\times10^{-3}$ V s^{2}m^{-1} and $c = 13$ Vsm^{-1}. The initial conditions are $x_0(0) = 0$ m·s, $x_1(0) = 20 \times 10^{-6}$ m, $x_2(0) = 0.2$ m/s and $w(0) = 0$. For the reference signal, we choose y_r as the output of the second order linear system $\frac{\omega_0^2}{s^2 + 2\xi\omega_0 s + \omega_0^2}$ with $\xi = 0.7$, $\omega_0 = 2\pi \times 500$ rad/s and zero input; that is, the linear system is driven only by the non-zero initial conditions $y_r(0) = x(0)$ and $\dot{y}_r(0) = \dot{x}(0)$. It can be seen that the outputs x_1 and x_2 are regulated to zero. Note that, although the control signal u is zero for negative times, its asymptotic value is different from zero. This fact can be explained as follows. Taking $y_r = 0$ in equations (11.15)-(11.16), it can be seen that the four states system (11.13)-(11.16) has an infinite number of equilibrium points. These equilibria are defined by $\{x_1 = 0, x_2 = 0, k_0 x_0(\infty) = \kappa_w w(\infty) = u(\infty)\}$. It is not necessary that $x_0(\infty) = 0$ so that the control value may be nonzero asymptotically (see Figure 11.5). In practice, this behavior is undesirable as it implies that the actuator applies a control action at equilibrium, which means an unnecessary loss of energy. Another inconvenient of this behavior is the modification of the equilibrium point of the system.

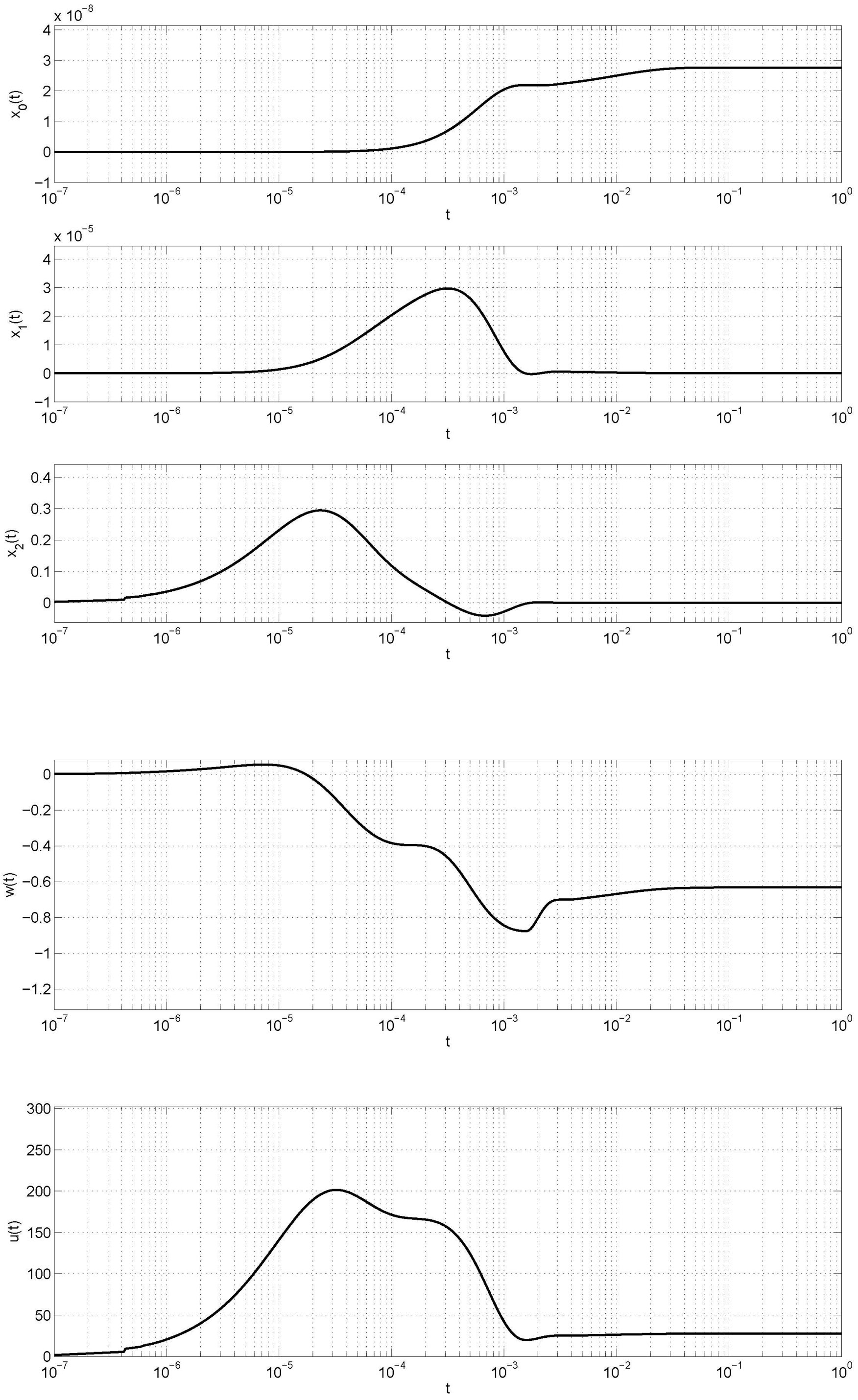

Figure 11.5: Closed loop signals relative to the control law of Section 11.4.1.

11.4.2 PID plus a sinusoidal component

The previous section has pointed out to the possible modification of the equilibrium point of the system under the action of a PID controller. Since this behavior is not acceptable in practice, a modification of the controller is proposed in this section to reduce this effect. The reason for having a control which is not zero asymptotically is that $u(\infty) = \kappa_w w(\infty)$ where $w(\infty)$ is not necessarily zero. To solve this problem, the idea would be to force the hysteretic term to go to zero asymptotically, inducing the control to go to zero. Consider that the system (11.1)-(11.3) is in open loop and choose for $u(t)$ a wave periodic input signal (see Section 9.1.1). Numerical simulations show that the obtained displacement signal $x(t)$ is also wave periodic. On the other hand, we know from Theorem 2 that, if the signal $x(t)$ is wave periodic, then the hysteretic output $w(\cdot)$ is also wave periodic and that it belongs asymptotically to the interval $[-\psi_{\sigma,n}(\rho(X_{\max} - X_{\min})), \psi_{\sigma,n}(\rho(X_{\max} - X_{\min}))]$. On the other hand, it can be shown that, for fixed values of the parameters σ and n, the function $\psi_{\sigma,n}(\mu)$ is increasing with its argument μ. This implies that the interval $[-\psi_{\sigma,n}(\rho(X_{\max} - X_{\min})), \psi_{\sigma,n}(\rho(X_{\max} - X_{\min}))]$ can be made as small as desired if the quantity $X_{\max} - X_{\min}$ can be reduced arbitrarily. Numerical simulations suggest that if the amplitude of the wave periodic voltage input $u(t)$ is decreased, then the amplitude of the corresponding displacement signal is also decreased.

These remarks suggest the following control law for the system (11.1)-(11.3)

$$u(t) = -k_0 x_0(t) - k_1 x_1(t) - k_2 x_2(t) - A\sin(2\pi f t) \tag{11.17}$$

where A and f are positive design constants, and k_0, k_1, k_2 are computed using Theorem 4. The closed loop behavior is given in Figures 11.6 and 11.7 with the values of k_0, k_1, k_2 that have been determined in the previous section, and for different values of the parameters A and f. The initial states are $x_0(0) = 0$ m·s, $x_1(0) = 20 \cdot 10^{-6}$ m, $x_2(0) = 0.2$ m/s and $w(0) = 0$. The reference signal is chosen as in Section 11.4.1.

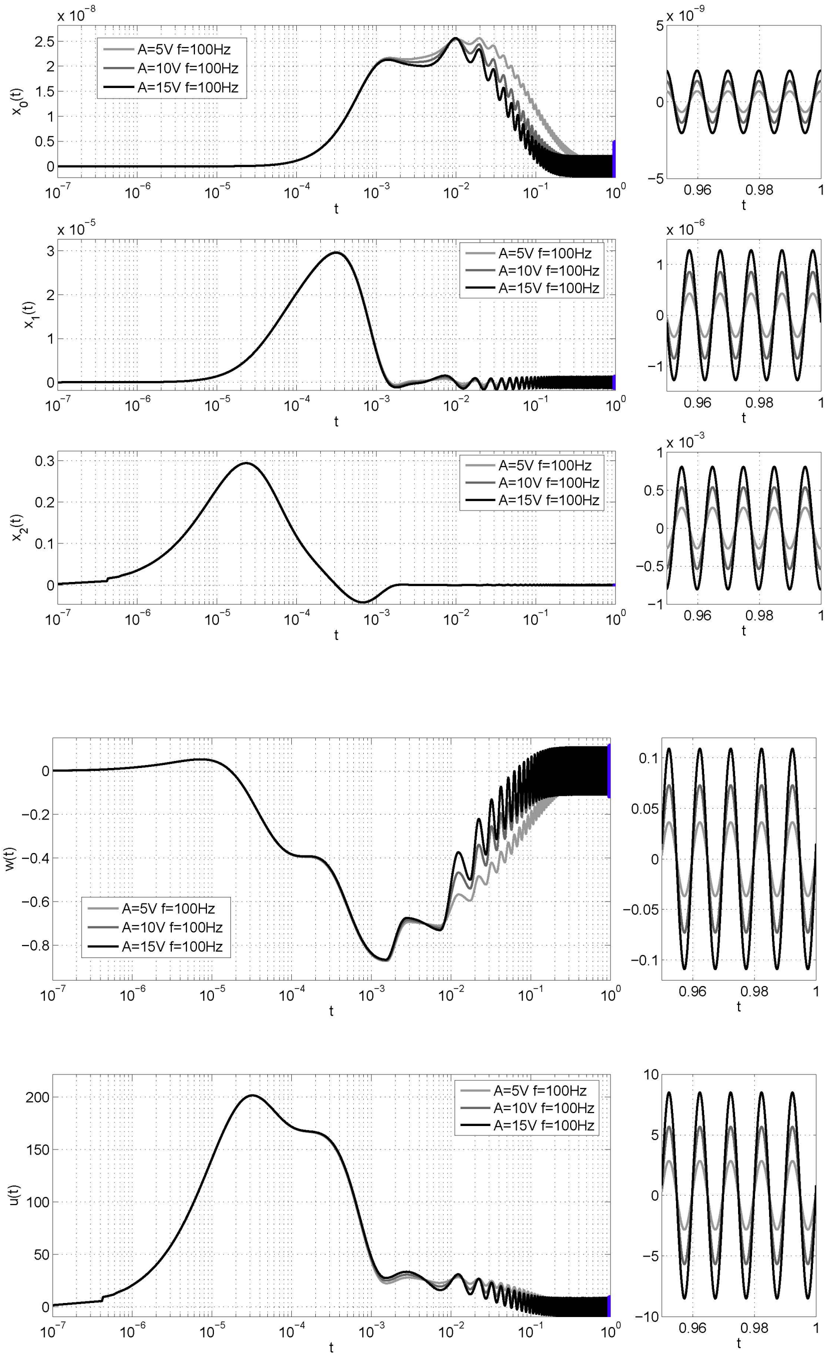

Figure 11.6: Closed loop signals relative the control law of Section 11.4.2. The figures in the right are a zoom in the indicated region of the figures in the left.

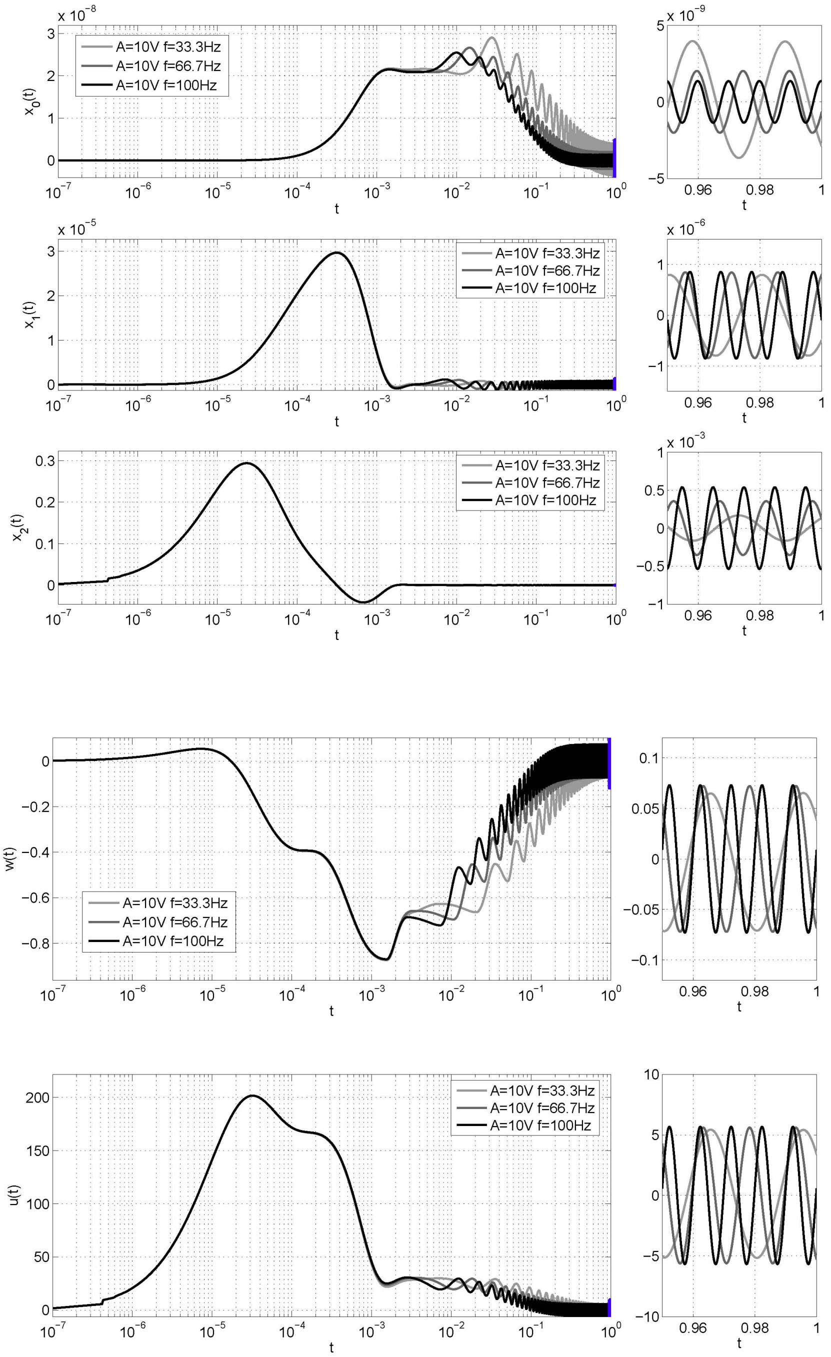

Figure 11.7: Closed loop signals relative the control law of Section 11.4.2. The figures in the right are a zoom in the indicated region of the figures in the left.

As noticed before, the steady-state response of the closed loop is periodic, and it can be seen that the amplitude of the closed loop signals $x(t)$, $\dot{x}(t)$ and $u(t)$ decreases as A decreases. The amplitude of the steady-state closed loop signals is independent of the frequency f. This frequency influences the settling time: the transient response of the system has a shorter duration for higher frequencies f.

As a conclusion, adding a term $A\sin(2\pi ft)$ to the PID controller makes the closed loop set point oscillating around zero. The amplitude of the oscillations can be made as small as desired by reducing the design parameter A.

11.4.3 PID plus a sinusoidal component with a time varying amplitude

The previous section has studied the behavior of a PID plus a sinusoidal component in the control law. It has been noticed that the set point of the closed loop steady-state systems oscillates around zero. As oscillations are also undesirable in practice, the control law has to be modified in order to eliminate them. Notice that the amplitude of the oscillations decreases with the amplitude of the sinusoidal component of the control law. This fact suggests to use for this component a time-varying amplitude that tends to decrease as the control law goes to zero. Since $u(\infty) = k_0 x_0(\infty)$ for the PID case, we choose as control law the expression:

$$u(t) = -k_0 x_0(t) - k_1 x_1(t) - k_2 x_2(t) - k_A x_0(t)\sin(2\pi ft) \qquad (11.18)$$

where k_A is a constant gain.

This control law has been tested using numerical simulations. The initial conditions are $x_0(0) = 0$ m·s, $x_1(0) = 20 \times 10^{-6}$ m, $x_2(0) = 0.2$ m/s and $w(0) = 0$. The reference signal is chosen as in Section 11.4.1.

The frequency f is taken to be 100 Hz as this value makes the settling time shorter without harming the overall response (see the previous section).

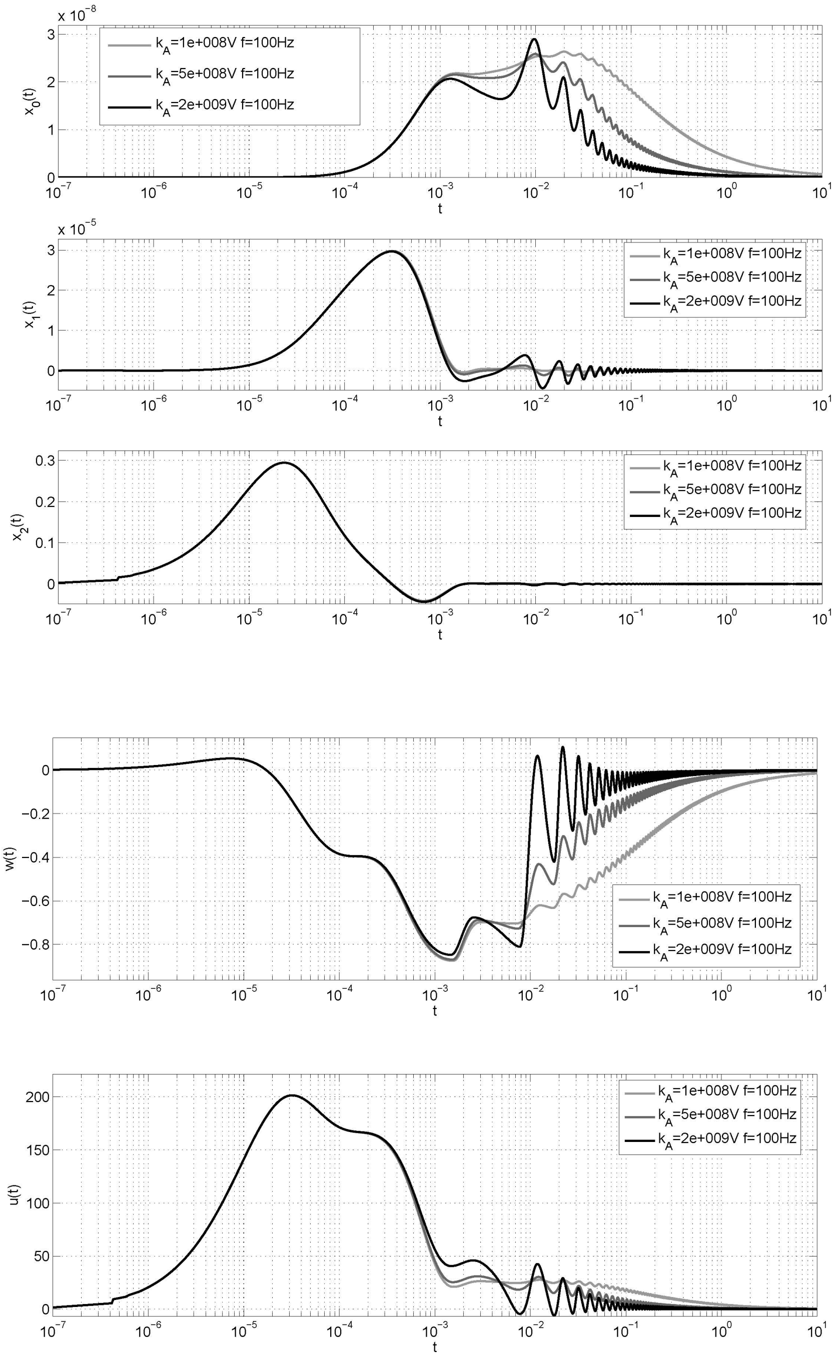

Figure 11.8: Closed loop signals applying the contol law introduced in Section 11.4.3 with $f = 100$ Hz and different k_A values.

Three values of k_A are chosen to study the effect of this parameter. The results of the closed loop simulations are given in Figure 11.8. It can be seen that the closed loop signals x_1 and x_2 converge to zero and that larger values of k_A lead to a shorter settling time. Furthermore, the control value is the same before and after the perturbation so that the equilibrium point of the closed loop remains unchanged.

11.5 Experimental Results

In this section, we apply the control laws of Sections 11.4.1, 11.4.2 and 11.4.3 to the piezoelectric element of Section 11.2.1. The numerical simulations conducted in the previous sections consisted in starting the system with nonzero initial conditions and seeing how the closed loop behaves. In our experimental platform, we first close the loop (that is we apply the control law) with a set point for the control around 200 Volts. Then we open the loop during 10 milliseconds in which the control is forced to have a constant value of 72 Volts. Then we closed the loop again. This time instant in which the loop is closed again corresponds to $t = 0$ in the previous numerical simulations. In this section, we take $y_r = 0$. The position of the piezoelectric element is measured directly so that the state x_1 is equal to the measured position. The state x_0 is obtained by approximating the exact integral by a sum of rectangles. The state x_2 is obtained using an Euler approximation.

11.5.1 PID Control

The controller of Section 11.4.1 is applied to the piezoelectric element. The PID constants are the same as in Section 11.4.1. The closed loop signals are given in Fig. 11.9. As observed in the numerical simulations, the position error and the velocity go asymptotically to zero, but the final value of controller output differs from its initial value. This means that the equilibrium point of the closed loop system is not robust to perturbations.

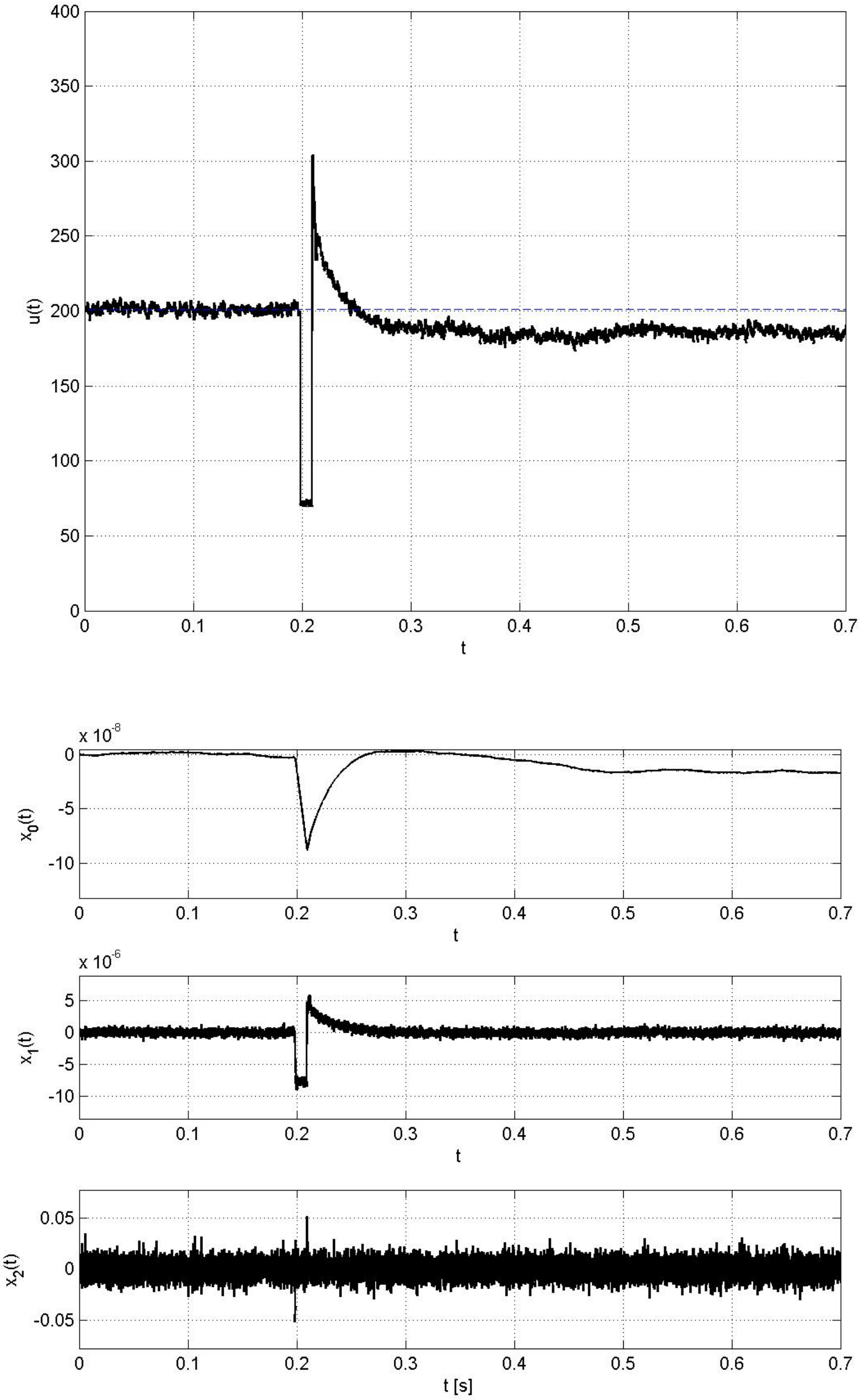

Figure 11.9: Closed loop signal with the controller of Section 11.4.1.

11.5.2 PID plus a sinusoidal component

The controller of Section 11.4.2 is applied to the piezoelectric element. We choose $A = 15$ V and $f = 10$ Hz. The constants k_0, k_1 and k_2 are the same as before. The closed loop signals are given in Fig. 11.10. Similar to what happens in numerical simulations, the closed loop system oscillates around zero.

11.5.3 PID plus a sinusoidal component with a time varying amplitude

The controller of Section 11.4.3 is applied to the piezoelectric element. We choose $k_A = 1.5 \times 10^9$ and $f = 100$ Hz. The constants k_0, k_1 and k_2 are the same as before. The closed loop signals are given in Fig. 11.11. It can be seen that the equilibrium point of the closed loop system is the same before and after the perturbation.

11.6 Conclusion

This chapter has presented a new control law for a piezoelectric actuator. The main challenge for the control design is the presence of hysteresis. The actuator has been represented using the Bouc-Wen model for hysteresis, and the model parameters have been identified. A nice agreement has been observed between the behavior of the piezoelectric actuator and the obtained model. Then, three control laws have been tested both numerically and experimentally for the position regulation of the piezoelectric device. It has been observed that a PID with a time-varying component insures that the displacement and velocity of the actuator go to zero asymptotically, while maintaining the same equilibrium point for the closed loop system. The tracking problem for the micropositionning of the device, and the developing of a model of the piezoelectric actuator for high frequencies, are under investigation.

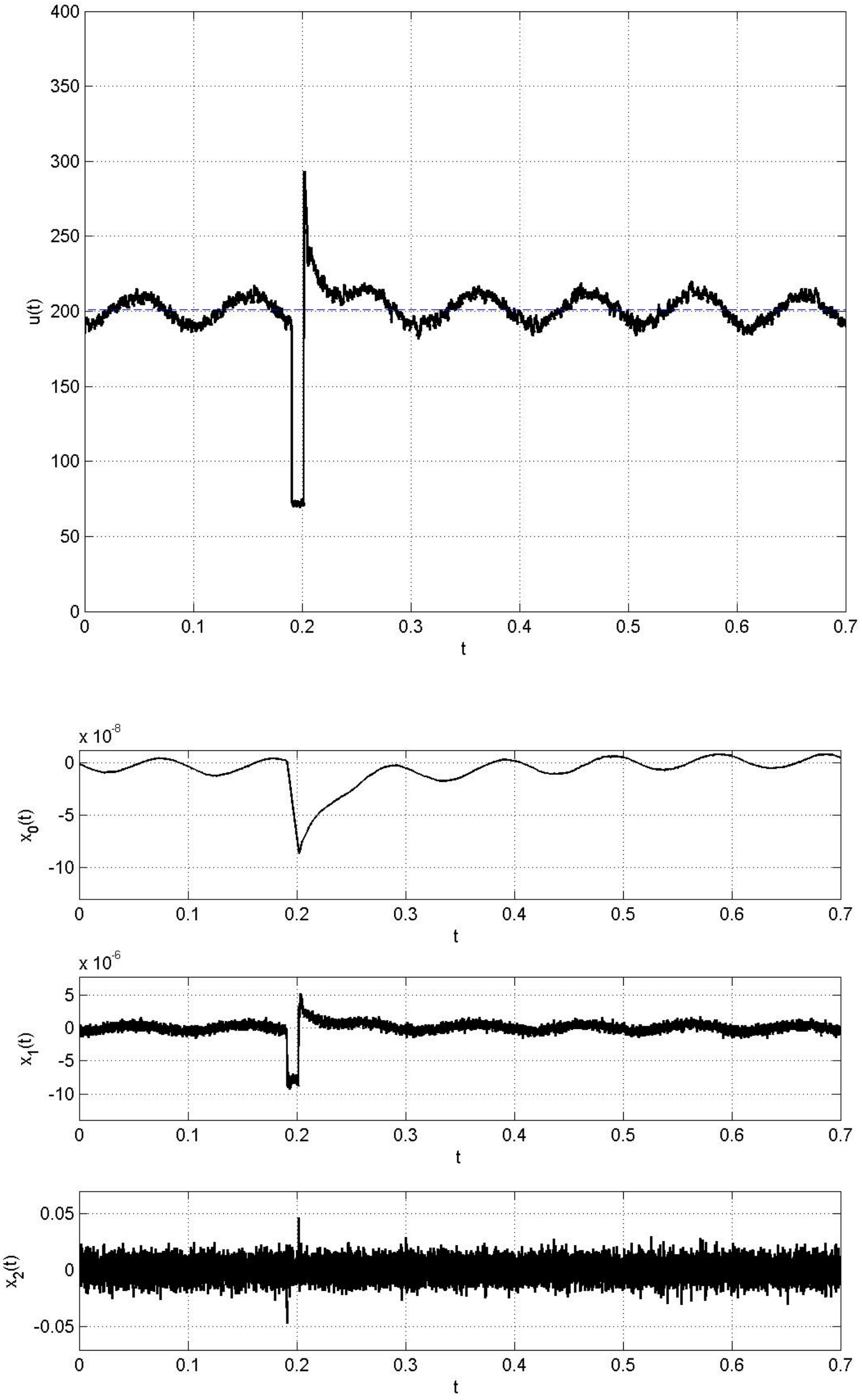

Figure 11.10: Closed loop signal with the controller of Section 11.4.2.

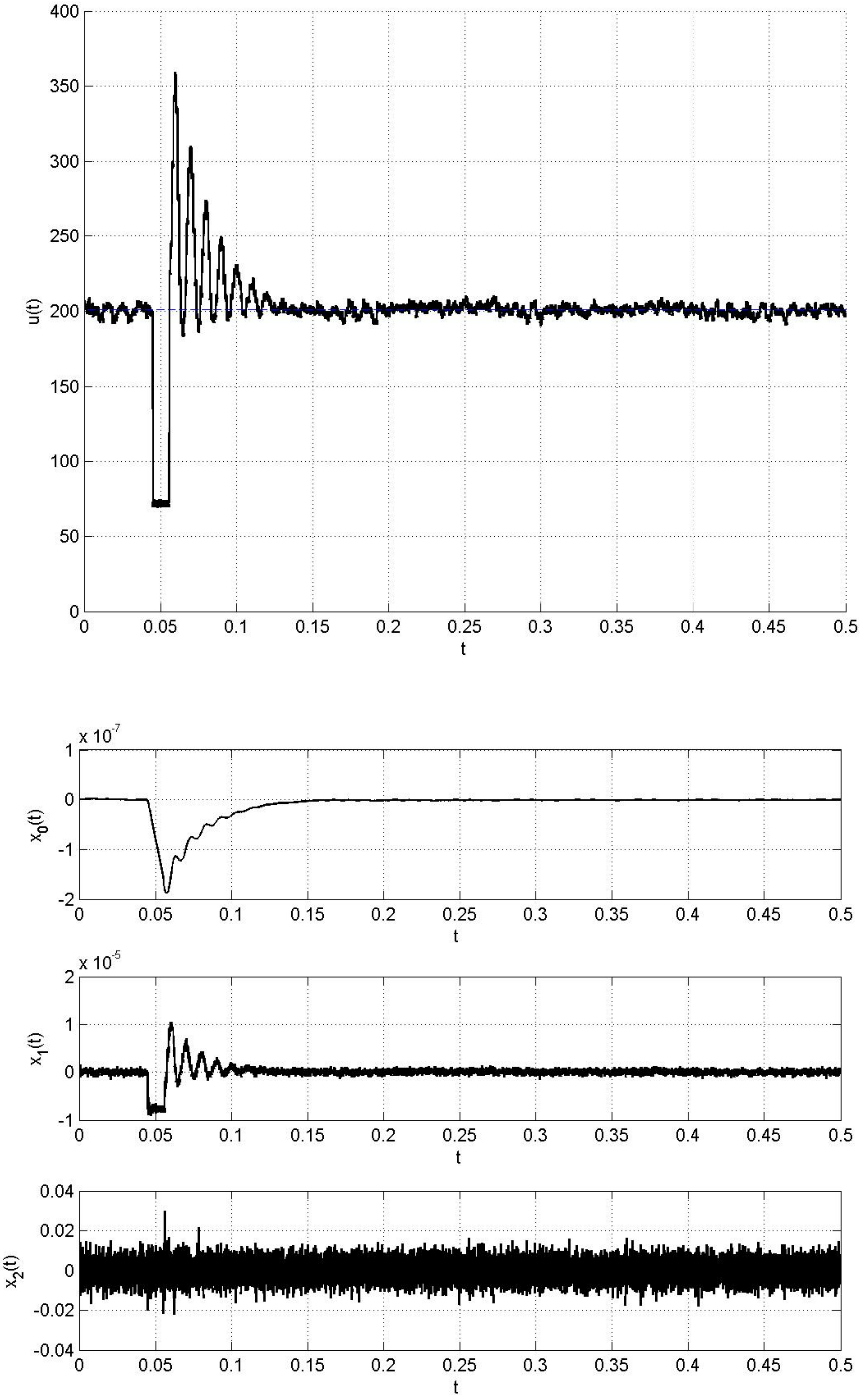

Figure 11.11: Closed loop signal with the controller of Section 11.4.3.

Chapter 12

Conclusions

12.1 Contributions

The present thesis part has investigated models to represent the hysteretic behavior of piezoelectric actuators in order to apply them to the conception of controllers for such hysteretic systems. The Bouc-Wen hysteresis model has been introduced, along with an identification technique to determine the parameters. Its robustness against different classes of perturbations has been discussed. The original model has been modified in order to characterize better the behavior of piezoelectric actuators. The model has been validated with a real actuator and the advantages over the original have been shown.

Furthermore, a new control law for a piezoelectric actuator has been introduced, taking into account the presence of hysteresis. Three control laws have been tested both numerically and experimentally for the position regulation of the piezoelectric device. It has been observed that a PID with a time-varying component insures that the displacement and velocity of the actuator go to zero asymptotically, while maintaining the same equilibrium point for the closed loop system.

The contributions of this thesis part can be summarized:

- Improvement of the existing Bouc-Wen model by considering a polynomial relationship in the non-hysteretic term, along with the modification of the identification technique and the experimental validation of the results. These contributions are collected in [16; 17; 26; 27]

- The design of a linear time-varying controller for the obtained model of a piezoelectric actuator. This design improves the previous results of the literature in the sense that the closed loop is asymptotically stable. These results are summarized in [18]

12.2 Future work

There are a number of possible interesting and challenging fields to investigate. It may become specially interesting to delve into:

- Modeling of piezoelectric for **high frequencies**. It is known that many applications of piezoelectric actuators take advantage of the high frequency capability of such a class of actuators. In this frame, the modeling of the actuators at high frequencies is an important challenge.

- **Tracking**. The micro-positioning regulation problem has been discussed; however, many applications require tracking control approaches which can possibly be addressed using similar techniques to those described in this thesis.

- Employment of **non-linear controllers**. Although linear controllers have the important advantage of easy implementation, non-linear controllers may provide some improvements in the response of the actuator. To these end, the introduction of such strategies is encouraged.

Bibliography

[1] M.F. Ashby and D. Cebon. Material selection in mechanical design. In *Troisieme Conference Europeenne sur les Materiaux et les Procedes Avances, Euromat '93*, Paris, June 8-10 1993. 4, 6

[2] D.M. Auslander. What is mechatronics? *IEEE/ASME Transactions on Mechatronics*, 1(1):5–9, Mar 1996. vii, xi

[3] Ll. Bonals and R. Ruiz. *Transmissió de calor*. Edicions UPC, Barcelona, 1994. 13, 17, 18

[4] V. Brailovsk, S. Prokoshkin, P. Terriault, and F. Trochu. *Shape Memory Alloys: Fundamentals, Modeling and Applications.* Université du Québec, École de Technologie Supérieure, 2003. 59, 88, 95

[5] E. Buckingham. On physically similar systems: Illustrations of the use of dimensional equations. *Phys. Rev.*, 4:345–376, 1914. 24, 31, 48

[6] B. M. Chen, T. H. Lee, C. C. Hang, Y. Guo, and S. Weerasooriya. An H_∞ almost disturbance decoupling robust controller design for a piezoelectric bimorph actuator with hysteresis. *IEEE Transactions on Control Systems Technology*, 7(2):160–174, 1999. 60, 75, 82, 121, 127

[7] S. B. Choi, S. K. Lee, and Y. P. Park. A hysteresis model for the field-dependent damping force of a magnetorheological damper. *Journal of Sound and Vibration*, 245(2):375–383, 2001. 75, 82

[8] J. Curie and P. Curie. Développement par compression de l'électricité polaire dans les cristaux hémièdres à faces inclinées. *Bulletin de la Société Minéralogique de France*, 3:90–93, 1880. 57, 63, 66

[9] P. Duhem. Die dauernden aenderungen und die thermodynamik. *Zeitschrift für Physikalische Chemie*, 22:543–589, 1897. 58, 74

[10] S. Erlicher and N. Point. Thermodynamic admissibility of bouc-wen type hysteresis models. *C. R. Mecanique*, 332:51–57, 2004. 84

[11] G.C Foliente. Hysteresis modeling of wood joints and structural systems. *ASCE Journal of Structural Engineering*, 121(6):1013–1022, 1995. 58, 74, 75, 82

[12] V. Giurgiutiu and C. A. Rogers. Energy based comparision of solid state induced strain actuators. *Journal of intelligent material systems and structures*, 7, January 1996. 4, 6

[13] O. Gomis-Bellmunt, S. Galceran-Arellano, A. Sudrià-Andreu, D. Montesinos-Miracle, and F. Campanile. Nuevo motor piezoeléctrico basado en módulos piezoeléctricos flexibles. In *XV Reunión de grupos de inverstigación de Ingeniería Eléctrica*, Zaragoza, Spain, Mar 2005. 162

[14] O. Gomis-Bellmunt, S. Galceran-Arellano, A. Sudrià-Andreu, D. Montesinos-Miracle, and L. F. Campanile. Linear electromagnetic actuator modeling for optimization of mechatronic and adaptronic systems. *Mechatronics*, 2006. 48, 50, 54, 57, 77, 161

[15] O. Gomis-Bellmunt, S. Galceran-Arellano, A. Sudrià-Andreu, D. Montesinos-Miracle, and J. Rull-Duran. Hydraulic actuator modeling for optimization of mechatronic and adaptronic systems. *Submitted to Mechatronics*, 2006. 54, 161

[16] O. Gomis-Bellmunt, F. Ikhouane, P. Castell-Vilanova, and J. Bergas-Jané. Modeling and validation of a piezoelectric actuator. *Accepted for publication in Electrical Engineering - Archiv für Elektrotechnik*, 2006. 146, 161

[17] O. Gomis-Bellmunt, F. Ikhouane, P. Castell-Vilanova, and D. Montesinos-Miracle. Modeling a hysteretic piezoelectric actuator employing a modified bouc-wen model. In *ECC2007 European Control Conference 2007*, Kos, Greece, July 2007. 146, 162

[18] O. Gomis-Bellmunt, F. Ikhouane, and D. Montesinos-Miracle. Control of a piezoelectric actuator considering hysteresis. *Submitted to Precision Engineering*, 2006. 146, 162

[19] G.H. Haertling. Ferroelectric ceramics: History and technology. *Journal of the American Ceramic Society*, 82(4):797–818, 1999. 66

[20] L. Holloway. Materials selection for optimal environmental impact in mechanical design. *Materials and Design*, 19:133–143, 1998. 4

[21] D. Howe. Magnetic actuators. *Sensors and Actuators*, 81:268–274, 2000. 6

[22] T.R. Hsu. Mechatronics. An overview. *IEEE Transactions on Components, Packaging, and Manufacturing Technology, Part C*, 20(1):4–7, Jan 1997. vii, xi

[23] J. E. Huber, N. A. Fleck, and M. F. Ashby. The selection of mechanical actuators based on performance indices. *Proc. R. Soc. Lond. A*, 453:2185–2205, 1997. 4, 6, 7

[24] C.L. Hwang, C.J., and Y.H. Chen. Piezomechanics using intelligent variable-structure control. *IEEE Transactions on Industrial Electronics*, 48(1):47–59, Feb 2001. 60, 121

[25] Ferroelectrics IEEE Ultrasonics and Frequency Control Society. *IEEE Standards on Piezoelectricity*. IEEE, 1987. 63, 64, 65

[26] F. Ikhouane, O. Gomis-Bellmunt, and P. Castell-Vilanova. A limit cycle approach for the parametric identification of hysteretic systems. *Submitted to IEEE Transactions on Control Systems Technology*, 2006. 58, 59, 103, 128, 146, 162

[27] F. Ikhouane, O. Gomis-Bellmunt, and P. Castell-Vilanova. A new identification method for hysteretic systems: Theory and experiments. In *ECC2007 European Control Conference 2007*, Kos, Greece, July 2007. 146, 162

[28] F. Ikhouane, V. Mañosa, and J. Rodellar. Adaptive control of a hysteretic structural system. *Automatica*, 41(2):225–231, 2005. 75, 82

[29] F. Ikhouane and J. Rodellar. On the hysteretic Bouc-Wen model. part I: Forced limit cycle characterization. *Nonlinear Dynamics*, 42(1):63–78, 2005. 58, 83, 87, 88, 89, 90, 122, 123, 128

[30] F. Ikhouane and J. Rodellar. On the hysteretic Bouc-Wen model. part II: Robust parametric identification. *Nonlinear Dynamics*, 42(1):79–95, 2005. 59, 88, 89, 128

[31] F. Ikhouane and J. Rodellar. A linear controller for hysteretic systems. *IEEE Transactions on Automatic Control*, 51(2):340–344, 2006. 60, 75, 82, 121, 122, 123

[32] F. Ikhouane and J. Rodellar. *Systems with hysteresis: Analysis, identification and control using the Bouc-Wen model.* John Wiley & Sons, to appear in 2007. 82

[33] F.P. Incropera and D.P. DeWitt. *Introduction to heat transfer.* Wiley, New York, 1990. 18, 32

[34] H. Janocha. *Adaptronics and Smart Structures.* Springer Verlag, 2000. 76

[35] S. Katzir. The discovery of the piezoelectric effect. *Arch. Hist. Exact Sci.*, 57:61–91, 2003. 66

[36] M.A. Krasnosel'skii and A.M. Pokrvskii. *Systems with Hysteresis.* Nauka, Moscow, 1983. 58, 74

[37] K. Kuribayashi. Criteria for the evaluation of new actuators as energy converters. *Advanced robotics*, 7(4):289–307, 1993. 4, 6

[38] A. Kyprianou, K. Worden, and M. Panet. Identification of hysteretic systems using the differential evolution algorithm. *Journal of Sound and Vibration*, 248(2):289–314, 2001. 88

[39] T. S. Low and W. Guo. Modeling of a three-layer piezoelectric bimorph beam with hysteresis. *Journal of Microelectromechanical Systems*, 4(4):230–237, Dec 1995. 58, 74, 75, 82

[40] J.W. Macki, P. Nistri, and P. Zecca. Mathematical models for hysteresis. *SIAM Review*, 35(1):94–123, 1993. 58, 74

[41] Y. Q. Ni, J. M. Ko, and C. W. Wong. Identification of non-linear hysteretic isolators from periodic vibration tests. *Journal of Sound and Vibration*, 217(4):737–756, 1998. 84, 91

[42] Physik Instrumente PI. *The world of Micro- and Nanopositioning*, 2005-2006. 76

[43] F. Preisach. Über die magnetische nachwirkung. *Zeitschrift für Physik*, 94:277–300, Feb 1935. 58, 74

[44] C. Ru and L. Sun. Hysteresis and creep compensation for piezoelectric actuator in open-loop operation. *Sensors and Actuators A: Physical*, 122(1):124–130, July 2005. 58, 74

[45] R.C. Smith. *Smart Material Systems: Model Development*. SIAM, Philadelphia, 2005. 58, 74

[46] A. W. Smyth, S. F. Masri, E. B. Kosmatopoulos, A. G. Chassiakos, and T. K. Caughey. Development of adaptive modeling techniques for non-linear hysteretic systems. *International Journal of Non-Linear Mechanics*, 37:1435–1451, 2002. 74, 82

[47] B. F. Spencer, S. J. Dyke, M. K. Sain, and J. D. Carlson. Phenomenological model for magnetorheological dampers. *Journal of Engineering Mechanics ASCE*, 123:230–238, 1997. 75, 82, 84

[48] A. Sudrià, O. Gomis, and D. Montesinos. La mecatrónica es algo realmente distinto. *Automática e Instrumentación*, 362:48–57, May 2005. vii, xi, 161

[49] S. Timoshenko and D. H. Young. *Elements of Strength of Materials.* Princeton, NJ, 4th edition, 1962. 40, 41

[50] M. Triantafyllou, K.T. Neumann, H. Reichl, F. Ansorge, V. Grosser, K.F. Becker, E. Schmidt, and R. Maier. Mechatronics for automotive and industrial applications. *IEEE Transactions on Advanced Packaging*, 22(3):433–441, Aug 1999. vii, xi

[51] S. A. Turik, L. A. Reznitchenko, A. N. Rybjanets, S. I. Dudkina, A. V. Turik, and A. A. Yesis. Preisach model and simulation of the converse piezoelectric coefficient in ferroelectric ceramics. *Journal Of Applied Physics*, 97(64102):1–4, 2005. 58, 74

[52] K. Uchino. *Piezoelectric Actuators and Ultrasonic Motors.* Kluwer Academic Publishers, 1997. xxiii, 63, 66, 76, 77

[53] K. Uchino. *Ferroelectric Devices.* Marcel Dekker Inc., 2000. 63

[54] A. Visintin. *Differential Models of Hysteresis.* Springer-Verlag, 1994. 58, 74

[55] W. Voigt. *Lehrbuch der Kristallphysik.* B. G. Teubner, Leipzig, 1910. 67

[56] J.W. Waanders. *Piezoelectric Ceramics. Properties and Applications.* Philips Components, Eindhoven, 1st edition, April 1991. 70

[57] Y. K. Wen. Method of random vibration of hysteretic systems. *Journal of Engineering Mechanics Division, ASCE*, 102(2):249–263, 1976. 74, 81

[58] Wikipedia. Piezoelectricity. In *Wikipedia.* 2006. 66

[59] K.A. Yi and R.J. Veillette. A charge controller for linear operation of a piezoelectric stack actuator. *IEEE Transactions on Control Systems Technology*, 13(4):517–526, Jul 2005. 60, 121

[60] M. Zupan, M. F. Ashby, and N. A. Fleck. Actuator classification and selection - the development of a database. *Advanced engineering materials*, 4(12):933–940, 2002. 4, 6

Appendix A

Outline of the proof of Theorem 3

The proof is done in several steps.

A.1 Determination of the parameter κ_x

As seen in chapter 9, the determination of the parameter κ_x involves two experiments: the first one consists in obtaining the limit cycle with the input x and the second one consists in obtaining the limit cycle with the input $x_1 = x + q$. Both experiments are subject to input disturbances d and d_1 as well as to measurement disturbances v and v_1. All of these perturbations are supposed to verify Assumption 1. The equation of the limit cycle obtained with the input x_1 comes from Theorem 2 as:

$$\begin{aligned}
\bar{\Phi}_{BW,1}(x_1) &= \kappa_x X_{\max}\bar{x} + \kappa_x X_{\max}\bar{d}_1\left(\tau(\bar{x})\right) + \kappa_w \bar{w}_1(x_1) + \\
&\quad + X_{\max}\bar{v}_1\left(\tau(\bar{x})\right) + \kappa_x X_{\max}\bar{q} \qquad \text{(A.1)}\\
\bar{w}_1(x_1) &= \psi^+_{\sigma,n}\Big(\varphi^+_{\sigma,n}\left[-\psi_{\sigma,n}\left(\delta\left(1+\varepsilon_{1d}\right)\right)\right] + \\
&\quad + \frac{\delta}{2}\left[\bar{x} + 1 + \bar{d}_1\left(\tau(\bar{x})\right) - \bar{d}_1(0)\right]\Big) \qquad \text{(A.2)}
\end{aligned}$$

where $\varepsilon_{1d} = \dfrac{\bar{d}_1(T^+) - \bar{d}_1(0)}{2}$, $\bar{d}_1(\tau) = \dfrac{d_1(\tau)}{X_{\max}}$ and $\bar{v}_1(\tau) = \dfrac{v_1(\tau)}{X_{\max}}$.

The estimated parameter κ_x° is computed from equation (9.20) as:

$$\kappa_x^\circ = \frac{\bar{\Phi}_{BW,1}(x_1) - \bar{\Phi}_{BW}(\bar{x})}{q} \tag{A.3}$$

Using standard analysis tools, it follows that the relative error on the parameter κ_x is given by:

$$\begin{aligned} \left|\frac{\kappa_x^\circ - \kappa_x}{\kappa_x}\right| \quad \leq \quad & \frac{\left|\bar{d}_1 - \bar{d}\right|}{\bar{q}} + \frac{\kappa_w}{X_{\max}\kappa_x\bar{q}} \left|\bar{w}_1(x_1) - \bar{w}(\bar{x})\right| + \\ & + \frac{\left|\bar{v}_1 - \bar{v}\right|}{\kappa_x\bar{q}} \end{aligned} \tag{A.4}$$

which leads to:

$$\left|\frac{\kappa_x^\circ - \kappa_x}{\kappa_x}\right| \leq \frac{c_1\mu}{\bar{q}} \tag{A.5}$$

for some constant c_1. From inequality (A.5) it is clear that to get $\left|\frac{\kappa_x^\circ - \kappa_x}{\kappa_x}\right| \leq \epsilon$ it is enough to have $\mu \leq \frac{\epsilon\bar{q}}{c_1}$. The next step is to compute the function θ defined by equation (9.21). However, the true value of the parameter κ_x is not known, and we know instead its estimate κ_x°. Thus, all we can compute is the estimate:

$$\theta^\circ(\bar{x}) = \bar{\Phi}_{BW}(\bar{x}) - \kappa_x^\circ X_{\max}\bar{x} \tag{A.6}$$

A.2 Existence and unicity of the zero of the function $\theta^\circ(\bar{x})$

As seen in chapter 9, the determination of the rest of the parameters uses the zero of the function θ°. The existence of this zero will be insured if we can show that $\theta^\circ(1) > 0$ and $\theta^\circ(-1) < 0$ due to the continuity of the function $\theta^\circ(\bar{x})$. From equations (A.6), (9.35), and (9.34) we get:

$$\begin{aligned} \theta^\circ(1) \quad = \quad & \left(\kappa_x - \kappa_x^\circ\right) X_{\max} + \kappa_x X_{\max}\bar{d}(T^+) + \\ & + X_{\max}\bar{v}(T^+) + \kappa_w\psi_{\sigma,n}\left(\delta\left(1 + \varepsilon_d\right)\right) \end{aligned} \tag{A.7}$$

Using Assumption 1 along with equations (A.7) and (A.5) it follows that:

$$\theta^{\circ}(1) \geq -\mu X_{\max} c_2 + \kappa_w \psi_{\sigma,n}\left(\rho X_{\max}\right) \tag{A.8}$$

for some constant c_2. The term $\psi_{\sigma,n}\left(\rho X_{\max}\right)$ can be developed in Taylor series as $\psi_{\sigma,n}\left(\rho X_{\max}\right) = \frac{1}{2}\rho X_{\max} + o\left(X_{\max}\right)$. Thus, if we have $\mu < \dfrac{\rho \kappa_w}{2c_2} = c_3$ then, by equation (A.8), we have $\theta^{\circ}(1) > 0$ for all $X_{\max} \in (0, A]$ for some constant A. To have $\theta^{\circ}(1) > 0$ for all $X_{\max} \in \left(0, \dfrac{\kappa_w}{\kappa_x}\right]$ it is enough to have $\mu < \dfrac{\kappa_w \psi_{\sigma,n}\left(\rho A\right)}{c_2 \frac{\kappa_w}{\kappa_x}} = c_4$. Similarly, it can be shown that we have $\theta^{\circ}(-1) < 0$ for all $X_{\max} \in \left(0, \dfrac{\kappa_w}{\kappa_x}\right]$ for $\mu < c_5$ for some constant c_5. Thus we have proved that for μ sufficiently small, the function $\theta^{\circ}(\bar{x})$ has at least one zero. Using standard analysis arguments, it can be shown that:

$$\frac{\partial \theta^{\circ}(\bar{x})}{\partial \bar{x}} \geq X_{\max}\left(-\mu c_2 + c_6\right) \tag{A.9}$$

for some constant c_6. Taking $\mu \leq \dfrac{c_6}{2c_2}$ we get from equation (A.9):

$$\frac{\partial \theta^{\circ}(\bar{x})}{\partial \bar{x}} \geq \frac{c_6}{2} = c_7 > 0 \tag{A.10}$$

From equation (A.10) it comes that the function $\theta^{\circ}(\bar{x})$ is strictly increasing which proves the unicity of its zero that we denote $\bar{x}_*^{\circ}$.

A.3 Determination of the parameter n

It is to be noted that, by combining equations (A.6), (A.5) and the fact that $\theta^{\circ}\left(\bar{x}_*^{\circ}\right) = 0$, we have:

$$\left|\bar{w}\left(\bar{x}_*^{\circ}\right)\right| \leq \frac{c_2}{\kappa_x}\mu = c_8 \mu \tag{A.11}$$

Now, let $\bar{x}_{*1} = \bar{x}_*^{\circ} + r_1\left(1 - \bar{x}_*^{\circ}\right)$ where $0 < r_1 < 1$ is a design parameter. Then we have from equation (A.10) that

$$\theta^{\circ}\left(\bar{x}_{*1}\right) \geq c_7\left(\bar{x}_{*1} - \bar{x}_*^{\circ}\right) = c_7 r_1\left(1 - \bar{x}_*^{\circ}\right) = c_9 \tag{A.12}$$

Due to the fact that the function θ° is increasing, for all $\bar{x} \geq \bar{x}_{*1}$ we have $\theta^\circ(\bar{x}) \geq c_9$. This fact along with equations (A.6), (A.5) and Assumption 1 gives $\bar{w}(\bar{x}) > 0$ for all $\bar{x} \geq \bar{x}_{*1}$ for all $\mu \leq \frac{\kappa_x c_9}{2\kappa_w c_2}$. Let $\bar{x}_{*2} = \bar{x}_*^\circ + r_2 \left(1 - \bar{x}_*^\circ\right)$ where $0 < r_1 < r_2 < 1$ is a design parameter. An estimate of the parameter n comes from equation (9.24) as:

$$n^\circ = \frac{\log\left(\dfrac{\left(\frac{d\theta^\circ(\bar{x})}{d\bar{x}}\right)_{\bar{x}=\bar{x}_{*2}} - \left(\frac{d\theta^\circ(\bar{x})}{d\bar{x}}\right)_{\bar{x}=\bar{x}_*^\circ}}{\left(\frac{d\theta^\circ(\bar{x})}{d\bar{x}}\right)_{\bar{x}=\bar{x}_{*1}} - \left(\frac{d\theta^\circ(\bar{x})}{d\bar{x}}\right)_{\bar{x}=\bar{x}_*^\circ}}\right)}{\log\left(\dfrac{\theta^\circ(\bar{x}_{*2})}{\theta^\circ(\bar{x}_{*1})}\right)} \tag{A.13}$$

Standard mathematical arguments lead to:

$$\left|\frac{n^\circ - n}{n}\right| \quad \leq \quad c_{15}\mu \tag{A.14}$$

for some constant c_{15}. Thus, to get $\left|\frac{n^\circ - n}{n}\right| \leq \epsilon$ it is enough to have $\mu \leq \frac{\epsilon}{c_{15}}$.

A.4 Determination of the parameter κ_w

The next parameter to identify is κ_w using equation (9.26). An estimate of this parameter can be computed from equation (9.26) using the formula:

$$\kappa_w^\circ = \theta^\circ(\bar{x}_{*2}) \times \sqrt[n^\circ]{\frac{\left(\frac{d\theta^\circ(\bar{x})}{d\bar{x}}\right)_{\bar{x}=\bar{x}_*^\circ}}{\left(\frac{d\theta^\circ(\bar{x})}{d\bar{x}}\right)_{\bar{x}=\bar{x}_*^\circ} - \left(\frac{d\theta^\circ(\bar{x})}{d\bar{x}}\right)_{\bar{x}=\bar{x}_{*2}}}} \tag{A.15}$$

A simple mathematical analysis gives:

$$\left|\frac{\kappa_w^\circ - \kappa_w}{\kappa_w}\right| \quad \leq \quad c_{20}\mu \tag{A.16}$$

for some constant c_{20}. Thus, to obtain $\left|\frac{\kappa_w^\circ - \kappa_w}{\kappa_w}\right| \leq \epsilon$ it is enough to have $\mu \leq \frac{\epsilon}{c_{20}}$.

A.5 Determination of the parameter ρ

The identification of the parameter ρ is done using equation (9.27):

$$\rho^\circ = \frac{\left(\frac{d\theta^\circ(\bar{x})}{d\bar{x}}\right)_{\bar{x}=\bar{x}_*^\circ}}{X_{\max}\kappa_w^\circ} \tag{A.17}$$

Using standard mathematical arguments, it follows that:

$$\left|\frac{\rho^\circ - \rho}{\rho}\right| \quad \leq \quad c_{22}\mu \tag{A.18}$$

for some constant c_{22}. Thus, to get $\left|\frac{\rho^\circ - \rho}{\rho}\right| \leq \epsilon$ it is enough to have $\mu \leq \frac{\epsilon}{c_{22}}$.

A.6 Determination of the parameter σ

To determine the parameter σ we have to compute the function $\bar{w}(\bar{x})$ using equation (9.28). However, in this equation the parameter κ_w and the function θ are unknown. Thus we define the computable function:

$$\bar{w}^\circ(\bar{x}) = \frac{\theta^\circ(\bar{x})}{\kappa_w^\circ} \tag{A.19}$$

An estimate of the parameter σ can be computed from equation (9.29) as:

$$\sigma^\circ = \frac{1}{2}\left(\frac{\frac{\left(\frac{d\bar{w}^\circ(\bar{x})}{d\bar{x}}\right)_{\bar{x}=\bar{x}_{*3}}}{X_{\max}\rho^\circ} - 1}{\left(-\bar{w}^\circ(\bar{x}_{*3})\right)^{n^\circ}} + 1\right) \tag{A.20}$$

where $\bar{x}_{*3}$ and is a design parameter such that $\bar{w}^\circ(\bar{x}_{*3}) < \frac{\theta^\circ(-1)}{2\kappa_w^\circ} = r_3 < 0$. Standard arguments show that:

$$\left|\frac{\sigma^\circ - \sigma}{\sigma}\right| \quad \leq \quad c_{27}\mu \tag{A.21}$$

for some constant c_{27}. Thus, to get $\left|\frac{\sigma^\circ - \sigma}{\sigma}\right| \leq \epsilon$ it is enough to have $\mu \leq \frac{\epsilon}{c_{27}}$ which ends the proof of Theorem 3.

Appendix B

Publications

B.1 Journal papers

B.1.1 Published

[14] O. Gomis-Bellmunt, S. Galceran-Arellano, A. Sudrià-Andreu, D. Montesinos-Miracle, and L. F. Campanile. Linear electromagnetic actuator modeling for optimization of mechatronic and adaptronic systems. *Mechatronics*, 2006.
`http://dx.doi.org/10.1016/j.mechatronics.2006.07.002`

[16] O. Gomis-Bellmunt, F. Ikhouane, P. Castell-Vilanova, and J. Bergas-Jané. Modeling and validation of a piezoelectric actuator. *Electrical Engineering - Archiv für Elektrotechnik*, 2006.
`http://dx.doi.org/10.1007/s00202-006-0049-8`

[48] A. Sudrià, O. Gomis, and D. Montesinos. La mecatrónica es algo realmente distinto. *Automática e Instrumentación*, 362:48–57, May 2005.

B.1.2 Submitted

[15] O. Gomis-Bellmunt, S. Galceran-Arellano, A. Sudrià-Andreu, D. Montesinos-Miracle, and J. Rull-Duran. Hydraulic actuator modeling for optimization

of mechatronic and adaptronic systems. *Submitted to Mechatronics*, 2006.

[18] O. Gomis-Bellmunt, F. Ikhouane, and D. Montesinos-Miracle. Control of a piezoelectric actuator considering hysteresis. *Submitted to Precision Engineering*, 2006.

[26] F. Ikhouane, O. Gomis-Bellmunt, and P. Castell-Vilanova. A limit cycle approach for the parametric identification of hysteretic systems. *Submitted to IEEE Transactions on Control Systems Technology*, 2006.

B.2 Conference papers

B.2.1 Published

[13] O. Gomis-Bellmunt, S. Galceran-Arellano, A. Sudrià-Andreu, D. Montesinos-Miracle, and F. Campanile. Nuevo motor piezoeléctrico basado en módulos piezoeléctricos flexibles. In *XV Reunión de grupos de inverstigación de Ingeniería Eléctrica*, Zaragoza, Spain, Mar 2005.

B.2.2 Accepted

[17] O. Gomis-Bellmunt, F. Ikhouane, P. Castell-Vilanova, and D. Montesinos-Miracle. Modeling a hysteretic piezoelectric actuator employing a modified bouc-wen model. *ECC2007 European Control Conference 2007*, Kos, Greece, July 2007.

[27] F. Ikhouane, O. Gomis-Bellmunt, and P. Castell-Vilanova. A new identification method for hysteretic systems: Theory and experiments. *ECC2007 European Control Conference 2007*, Kos, Greece, July 2007.